FINAL REPORT

Catalytic and Transport Behaviors of Model and Porous and Composite Nanostructures

Grant Number: DE-FG02-02-ER15368

Period of Performance: September 15, 2002 to November 14, 2016

Institution: the University of New Mexico, 1 University of New Mexico MSC01 1120, Albuquerque, NM 87131

Principle Investigator: C. Jeffrey Brinker, Ph.D, Distinguished and Regent's Professor, Department of Chemical and Nuclear Engineering, The Department of Chemistry, and The Department of Molecular Genetics and Microbiology, the University of New Mexico, Albuquerque, NM. Fellow, Sandia National Laboratories, Albuquerque, NM.

PI Contact Information:

C. Jeffrey Brinker
Advanced Materials Laboratory
1001 University Blvd SE, Ste. 100
Albuquerque, NM 87106
E-Mail: cjbrink@sandia.gov
Phone: (505) 272-7629c

DOE/Office of Science Program Office: Office of Basic Energy Sciences

DOE/Office of Science Program Manager Contact:
Dr. Raul Miranda
Chemical Sciences, Geosciences, and Biosciences Division
Office of Basic Energy Sciences
SC-22.1/Germantown Building
U.S. Department of Energy
1000 Independence Avenue, SW
Washington, D.C. 20585-1290
E-Mail: Raul.Miranda@science.doe.gov
Phone: (301) 903-8014

Table of Contents

1.0 Introduction

As stressed in the Basic Energy Sciences Advisory Committee (BESAC) Report "New Science for a Secure and Sustainable Energy Future" (December 2008), solving our Nation's energy challenges will entail more than incremental changes in present materials-related technologies; new, advanced routes to nanostructured materials with transformational properties will be required. For example, the special properties of nanoparticle- (NP) based catalysts arising from small size are well known (i.e., high surface area for lowered materials cost, as in Pt fuel cell catalysts[1], or modification of electronic properties, illustrated by the activity of Au NC to low-temperature CO oxidation[2]). In general, however, only the catalytic properties of random dispersions of NPs have been studied; well-defined architectures incorporating NPs (as well as other active materials[3]) are expected to display new, emergent properties based on NP-NP interactions[4] as well as precisely defined catalytic sites between particles of two or more types and the nanoscale combination of multiple catalytic materials, enabling the efficient transformation of matter via multistep processes[5]. Furthermore the incorporation of catalysts within well-defined pores with controlled molecular access and an engineered 3D solvation/reaction environment could lead to new types of membrane reactors that increase selectivity and stability and reduce poisoning.

Separation membranes are another class of materials where dramatically improved properties will be needed to address our Nation's energy problems. Membranes operating in liquid or vapor appear in many current energy-related applications (for example, removing CO_2 from natural gas to prevent corrosion of high-pressure pipelines), as well as future energy technologies (purification of bio- or solar-derived fuels, selective proton transport for fuel cells, and CO removal from H_2 to prevent fuel cell poisoning). Also, CO_2 separation from power plant emissions for geological sequestration could become a significant application of membrane technology. However, current membrane technology does not achieve performance criteria needed in these (and other) critical energy-related applications. In particular, the predominant selectivity mechanism is that of size exclusion or 'molecular sieving', a mode of separation with inherent limitations in the trade-off between selectivity and molecular flux. Future developments in membrane development will require looking toward nature for inspiration, where the subtle interplay of pore size, spatially-defined surface modification, and pore asymmetry underlie the high-flux and nearly perfect ion and molecular selectivity of natural biological channels.

To address the needs of these areas, we our work explored the following integrated nanomaterials systems that coupled transport and catalytic behaviors:

1) The integration of ordered NP/oxide[6] and NP/polymer composite arrays[7] with membranes and/or stabilizing layers made by evaporation-induced self-assembly (EISA) or EISA combined with ALD or MLD. These arrays, as shown in **Figure 1.1 A** and **B** are 10-100 nm in thickness and composed of ordered 2D monolayers or multi-layers of nanoparticles assembled within an oxide (silica, alumina, or titania) or polymer matrix (including those with conducting and semiconducting properties). By virtue of NP proximity and arrangement, they are expected to possess altered and perhaps enhanced catalytic properties compared to random heterogeneous catalysts, and their integration with membranes will allow control of access and define at the membrane/NP interface a confined reaction volume with controlled solvation and steric constraints.

2) Oriented inorganic membrane reactors with transmembrane (along the pore length) control of pore size, surface chemistry, and catalyst location(s) formed by ALD and plasma-directed ALD in combination with evaporation induced self-assembly (**Figure 1.2**). Such asymmetric, graded reactors achieve improved selectivity and flux and avoid poisoning and coke formation compared to
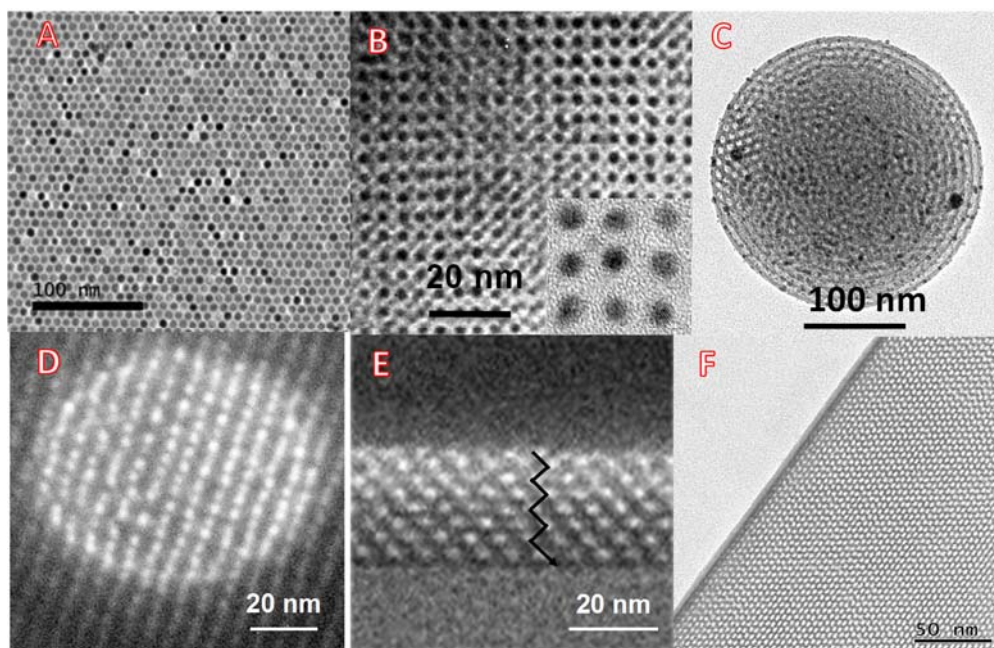
Figure 1.1. A) Large area, free-standing Au/PMMA arrays prepared by interfacial self-assembly and transferred to a holey carbon grid, B) Au NP/silica self-assembled array prepared by EISA, C) Pt-NP decorated mesoporous silica nanoparticle prepared by aerosol-assisted EISA and reduction, D) Free-standing mesoporous silica membrane formed over FIBed nanopore, E, cross-section of membrane in D, F) Ultra-thin polyamide desalination membrane formed by molecular layer deposition (MLD) on large area membrane formed by EISA.

conventional supported catalysts. They could also serve as a 'reaction-coordinate' along which reaction intermediates are stabilized and coupled reactions are enabled due to vectorial transport and local concentration effects. In addition to new membrane reactor structures, ALD processing will allow precise alloying of NP catalysts and layer-by-layer modification of the catalyst support chemistry.

3) 3D analogs of the thin film architectures denoted in (2) prepared by NP self-assembly or aerosol-assisted EISA and ALD (**Figure 1.1C**). Here ALD is used to control the size of the pore entrance and the pore surface/support chemistry; it can also be used to deposit a thin stabilization layer to avoid catalyst coarsening at higher temperatures.
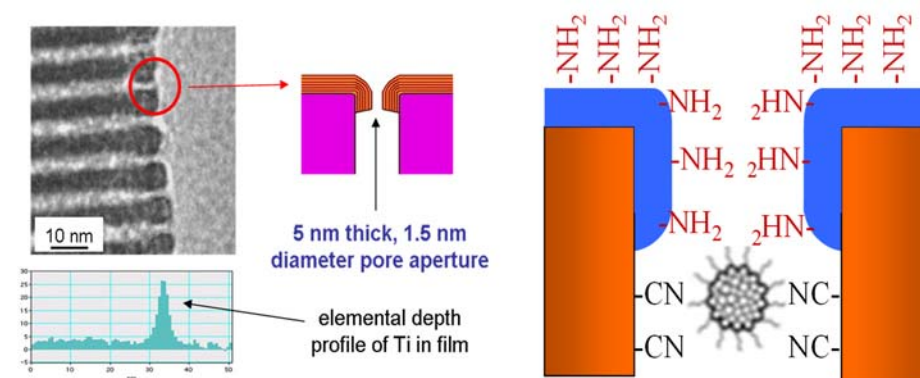
Figure 1.2. Plasma directed TiO_2 ALD on oriented silica nano-channels allows control of pore size and pore surface chemistry (left) and creates controlled access and reaction environment for catalyst nanoparticles (right).

4) Ultra-thin biomimetic polymer or hybrid composite membranes formed by plasma-directed ALD on or within nanoporous membranes formed by EISA (**Figure 1.1F**) and containing either synthetic or natural catalysts, i.e. enzymes. Such nanoporous-supported catalytic membranes are expected to have greater thermal, chemical, and mechanical stability compared to conventional membranes and are dimensionally very thin important for enhancing flux in applications like fuel cell membranes PEMs and CO_2 sequestration.

Catalytic systems have been designed for both liquid and vapor phase chemical transformations, with initial focus on the aerobic oxidation of alcohols in water over Pd/Au NPs[8-11] and the oxidation of CO.[12]

Our research is differentiated from on-going work in supported NP catalysts in several ways. First it exploits our unique ability to create ordered, NP/oxide or NP/polymer arrays transferrable to arbitrary substrates. In contrast to randomly organized or 'small scale' NP assemblies studied elsewhere,[6, 13-17] these large area arrays possess well-defined in-plane array symmetry with long-range order and uniform NP-NP spacings. Second, membrane self-assembly over top of these arrays will isolate NPs or NP dimers or timers in individual nano-reaction channels allowing further NP catalyst processing and atomic-level control of NP support chemistry using ALD and other chemical procedures. (Although it might be anticipated that NP/support interfaces between adjacent NPs might be important in governing catalysis, these interfaces are difficult to synthesis and isolate by other techniques). Third, employing atomic layer deposition and plasma-directed ALD and molecular layer deposition methods developed in our group, we can create stratified asymmetric pore channels with graded, along the channel control of pore size, surface chemistry, and catalyst or enzyme placement. This ability has the potential to create new classes of membranes and membrane reactors rivaling the performance of natural transporters and reaction centers.

Our research goals align with several of the Basic Energy Sciences Grand Challenges laid out in the 2007 BESAC report "Directing Matter and Energy: Five Challenges for Science and the Imagination", including "*How do we design and perfect atom- and energy- efficient synthesis of revolutionary new forms of matter with tailored properties", "How can we master energy and information on the nanoscale to create new technologies with capabilities rivaling those of living things*", and "*How do we characterize and control matter away—especially very far away—from equilibrium?*". Additionally, our research will address many "Basic Energy Needs" in specific areas outlined by BESAC. In "Catalysis for Energy" (2007), we will not only answer the Grand Challenge for the "Design and Controlled Synthesis of Catalytic Structures", creating new nanoarchitectures to increase *selectivity* of chemical processes, our NP arrays (with well-defined catalytic sites) will form model platforms to enable "Characterization of Solid Catalysts with Enhanced Spatial, Temporal, and Energy Resolution". Our NP/polymer arrays are also an ideal architecture to examine "Array Behavior of Nanostructures" identified as a need for "Basic Research Needs for Solid-State Lighting". Finally, our ALD membrane research will address several specific stated goals of "The Sure Energy Future" and "Hydrogen Economy" thrusts: novel membrane assemblies, nanoscale science, and quantitative/predictive modeling. It will also contribute fundamental understanding to science grand challenges: precision design and fabrication of new forms of matter with tailored properties, development of complex emergent behaviors that mimic the characteristics of living systems.

2.0 Background and Prior Accomplishments (DE-FG03-02ER15368)

Our prior BES-NSET-funded research focused on the development of new self-assembly approaches to controllably organize inorganic and inorganic components on the nanometer scale. Our goal was to form porous and composite films and particles exhibiting novel mass, charge and energy transport characteristics through controlled nanostructuring and nano-confinement effects. We developed several new classes of nanocomposite materials: sea-shell-like protective coatings that are of interest as permeation barriers[18], ultra-selective high flux membranes[19], responsive nanocomposites incorporating switchable organic ligands[20-24], molecules, or polymers within rigid inorganic scaffolds to derive synergistic function[25, 26], and 2- and 3-D metallic and semiconductor/nanoparticle arrays incorporated within inorganic or polymeric matrices[6, 7]. We focused on the preparation of these nanocomposites mainly as films (combining 'bottom-up' evaporation-induced self-assembly[27] with 'top-down' printing and lithography and atomic layer deposition) to enable their facile integration into devices and platforms of interest to the U.S. Department of Energy and the BES-funded Center for Integrated Nanotechnologies (CINT) at Sandia and Los Alamos National Laboratories. Our synthetic approach and highlights of accomplishments are summarized below.

2.1 Evaporation-Induced Self-Assembly (EISA)

Over a decade ago Mobil researchers demonstrated that surfactant self-assembly conducted in the presence of hydrophilic silicate precursors resulted in the spontaneous formation of surfactant/silica mesophases that upon heating were converted to so-called mesoporous silicas
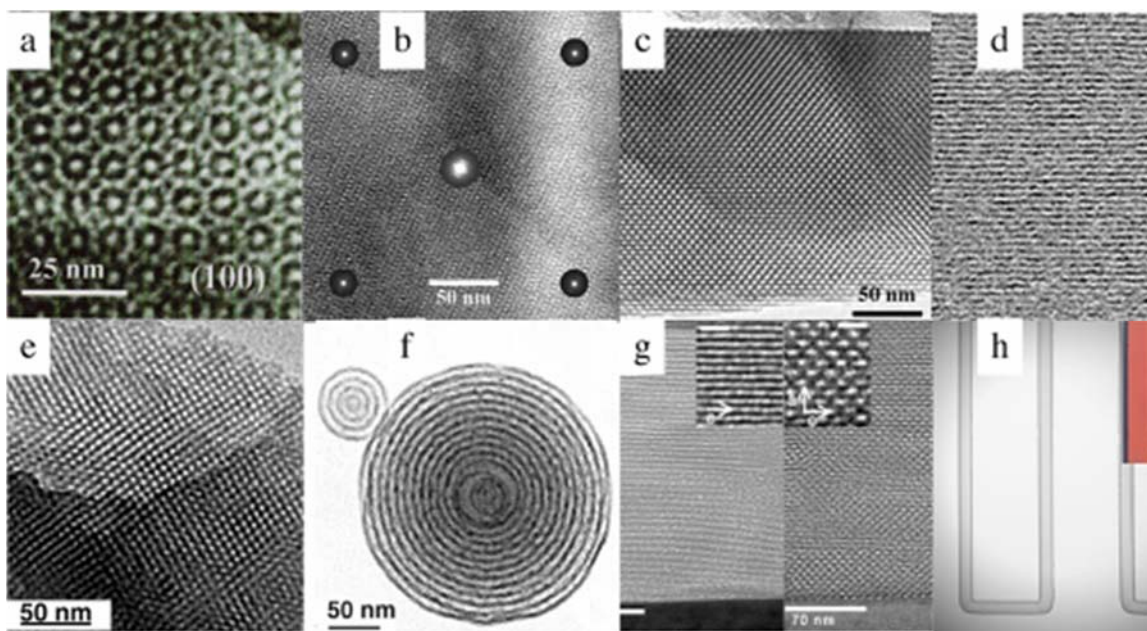
Figure 2.1. TEM micrographs of self-assembled porous and composite nanostructured coatings and particles. **a, b**: Plain-view of cubic thin film mesophases, **c**: cross-sectional TEM of hydrophobic, fluoro-alkylated silica mesophase, **d**: polyalkylmethacrylate/silica nanocomposite, **e**: conjugated polymer/ silica nanocomposite, **f**: nanostructured particles formed by aerosol-assisted self-assembly, **g**: optically induced phase transformation (hexagonal to cubic) developed in photosensitive mesophase **h**: patterned optically-active thin film mesophase written by a Robot-controlled pen.

characterized by a precise periodic arrangement of mono-sized pores. However, these procedures resulted exclusively in the precipitation of ill-defined powders that are difficult to integrate into devices. In order to form efficiently mesoporous silicas as uniform films (or well-defined spherical particles) our team pioneered the development of an evaporation-induced surfactant self-assembly *EISA* procedure[28-30]. Beginning with a homogeneous solution of soluble silica and surfactant prepared in ethanol/water solvent with initial surfactant concentration $c_o \ll cmc$, preferential evaporation of ethanol concentrates the depositing film in water and non-volatile surfactant and silica species. The progressively increasing surfactant concentration drives self-assembly of silica-surfactant micelles and their further organization into lyotropic liquid crystalline mesophases. Surfactant removal by washing or pyrolysis creates supported, highly ordered mesoporous coatings (**Figure 2.1 a-c**) of interest for sensors, membranes, catalyst supports, and low dielectric constant films[31, 32].

Starting with an *aerosol* dispersion of the same precursor solutions used to create mesoporous or nanocomposite films, *EISA* is also a route to ordered porous and composite powders[29]. Solvent evaporation creates a radial gradient of surfactant concentration within each droplet that steepens in time. This surfactant enrichment induces silica-surfactant self-assembly into micelles and further organization into liquid crystalline mesophases. The radial concentration gradient and presence of the liquid- vapor interface (that serves as a nucleating surface) causes ordered silica-surfactant liquid crystal domains to grow radially inward. TEM micrographs of representative porous particles are shown in **Figures 1.1C** and **2.1f**. This class of particles is being used widely as a 3D host for NP catalysts.

2.2 Nanoparticle Self-Assembly

In 2004 we reported in Science the formation of metallic and semiconducting NP micelles (**Figure 2.2**) and their ability to direct the formation of highly ordered NP arrays. This occurs through electrostatic and hydrogen-bonding interactions in a mechanism analogous to that of surfactant-directed self-assembly of silica/surfactant mesophases (used as precursors to so-called mesoporous silicas)[33]. For example, addition of tetraethyl orthosilicate under basic conditions results in the formation of hydrophilic oligosilicic acid species that organize with NC micelles to form a new type of ordered gold NC/silica mesophase. This nanocrystal mesophase has *fcc* symmetry (space group *Fm3m*), as shown in **Figure 2.3**. These images are consistent with an *fcc* unit cell with a unit cell dimension *a* of ~10.2 nm and uniform spacing between NCs of ~6 nm. This was the first example of an ordered *fcc* nanocrystal array formed spontaneously by self-assembly in aqueous media rather than by solvent evaporation[34, 35]. Compared with other ordered NC arrays, the embedding silica matrix provides for greater chemical, mechanical, and thermal robustness. Furthermore, thermodynamically controlled self-assembly provides greater order and control of NC spacing, compared with other connected nanocrystal systems such as those prepared by DNA hybridization[36]. Using acidic conditions designed to minimize the siloxane condensation rate, pathway i-ii-iv in **Figure 2.2** leads to the formation of thin films by means of standard techniques like spin-coating, micromolding, or inkjet printing.

These NP arrays have been the subject of considerable interest, as they serve as model "artificial solids" with tunable electronic, magnetic, and optical properties stemming from single-electron charging and quantum confinement energies of individual NCs mediated by coupling interactions with neighboring NCs. In general, such highly ordered NC arrays should *serve as model ideal systems in which to discover new nanoscale phenomena*, and to develop and test theories of collective optical, electronic, and catalytic behaviors.
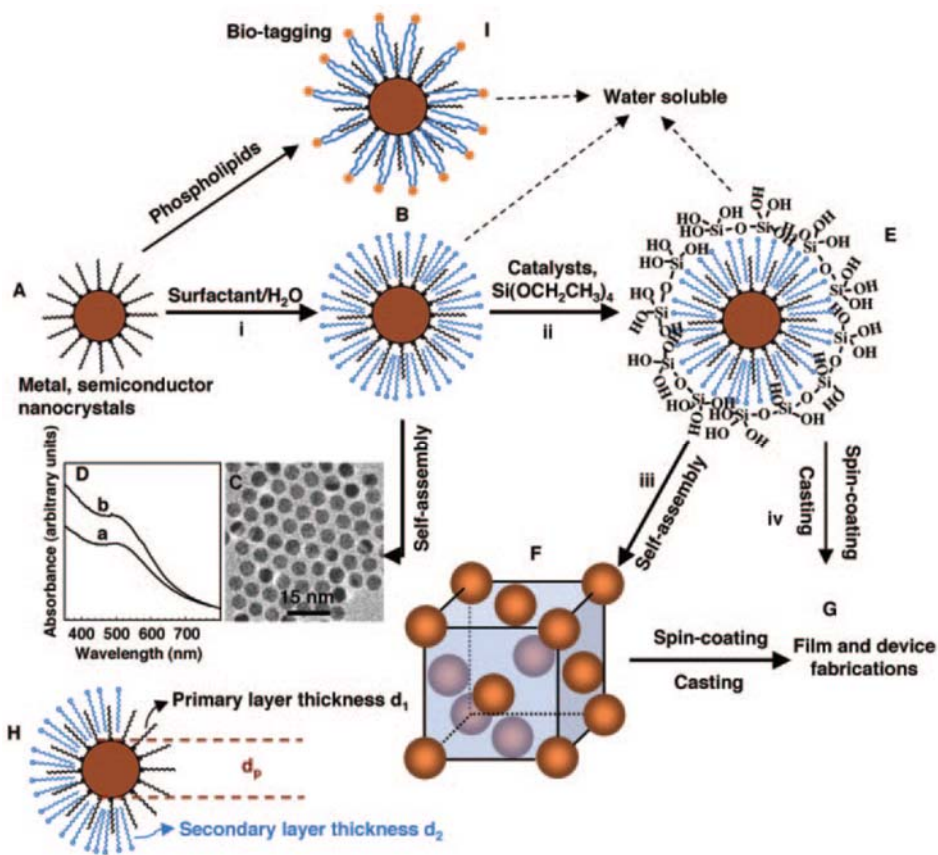
Figure 2.2. Processing diagram for the synthesis of water-soluble gold nanocrystal micelles and periodically ordered gold NC/silica mesophases. (**A**) Gold nanocrystals are prepared with 1-decanethiol as a stabilizing agent, with heat treatments employed to further narrow the particle size distributions. (**B**) The thiol-stabilized nanocrystals are encapsulated in surfactants (using an oil-in-water microemulsion technique) to form water-soluble NC micelles that, upon evaporation, self-assemble to form hexagonally ordered NC arrays as shown in the TEM image (**C**). (**D**) UV-visible spectra of (a) gold nanocrystals in chloroform and (b) gold NC micelles in water; both exhibit plasmon resonance bands at 510 cm^{-1}. (**E**) Silicic acid moieties formed by hydrolysis of TEOS are organized at the hydrophilic surfactant-water interface of NC micelles, leading, under basic conditions, to a gold NC/silica mesophase (**F**) composed of NCs organized in a periodic *fcc* lattice within a dense silica matrix. (**G**) Under acidic conditions that suppress siloxane condensation, spin coating or casting results in ordered thin-film NC/silica mesophases that are readily integrated into devices. (**H**) The lattice constant of the NC/silica mesophase is controlled by the nanocrystal size, d_p, the primary layer thickness of the stabilizing ligand, d_1, and/or the secondary layer thickness of the surfactant, d_2. (**I**) Polyethylene glycol surfactants or lipids can be used to prepare biocompatible water-soluble NC micelles for biolabeling. From Fan *et al*., *Science*, 2004.
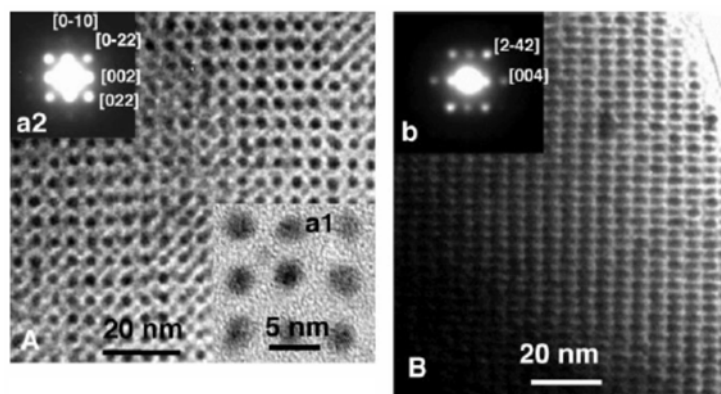
Figure 2.3. TEM images of a nanocrystal mesophases showing two orientations of an *fcc* structure: A) [100], B) [210]. From Fan *et al*.,*Science*, 2004.

2.3 Free-Standing, Patternable Nanoparticle/Polymer Monolayer Arrays

Recently, we have extended our work on NP assembly to 2D NP/polymer arrays fabricated on a water interface from toluene containing poly(methylmethacrylate) (PMMA) or other hydrophobic polymers.[7, 37, 38] This approach represents a new means to attain very highly loaded yet flexible particle/polymer nanocomposites,[39] which have eluded most synthetic efforts to date. In this procedure, a 5-10 µl drop of the toluene solution is deposited onto the water surface; as the drop spreads, solvent evaporation concentrates the thinning film in NPs and polymer, leading to NP self-assembly and solidification into an ordered NP monolayer array/polymer nanocomposite film with polymer thickness down to 10 nm and physical area of up to 100 cm^2 (**Figure 2.4**). The NP/polymer monolayer can be transferred to arbitrary substrates[38] and remains stable as a free-standing membrane suspended over cm-sized holes, even with free edges (**Figure 2.4C**). Additionally, the polymer layer can serve as a photoresist enabling electron beam (e-beam) NP patterning,[7] or as an e-beam deformable layer for coalescence of 2D Au NP lattices into arrays of Au 'wires' with anisotropic electronic transport properties.[37] Preliminary results have demonstrated the potential to extend this interfacial assembly procedure to produce true 2D binary lattices supported on polymer films. Results from *in situ* grazing-incidence small-angle x-ray (GISAXS) studies at the Advanced Photon Source (Argonne National Labs) show that assembly occurs through a lower density intermediate phase that is compressed by radial stresses induced by polymer drying (**Figure 2.4D**).
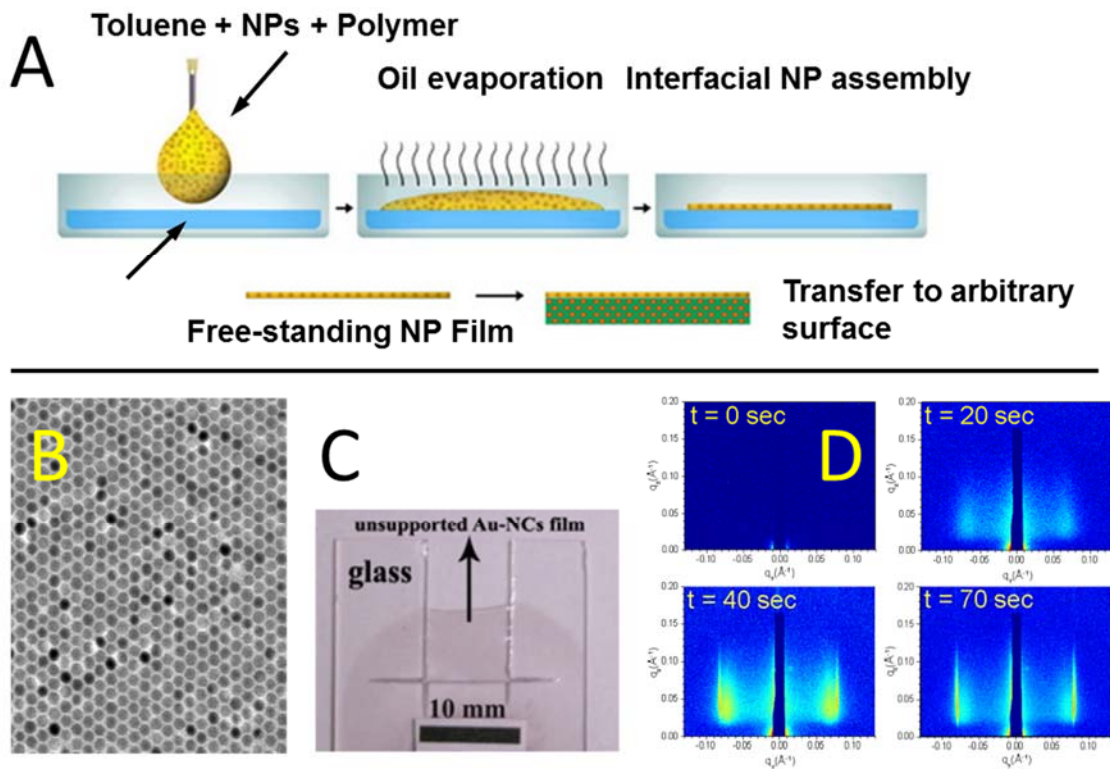
Figure 2.4. A) Interfacial assembly of NP/polymer films through spreading of NP and polymer in toluene across a water surface, B) TEM of the highly ordered NP 2D array formed on top of the ultrathin (10-100 nm) polymer film, C) image showing the mechanical stability of NP/polymer films, D) GISAXS time sequence of NP/polymer assembly at a water surface, showing NP ordering occurring through a less densely packed intermediate phase which is compressed to the final state by polymer drying stresses.

2.4 Atomic Layer Deposition on Porous Self-Assembled Substrates for Controlled Transport

2.4.1 Sub-10nm Thick Membranes Made by Plasma-Defined Atomic Layer Deposition

Surface-limited deposition of ultrathin layers on porous supports is important for the formation of high flux membranes. Here we achieve surface-limited deposition using a new procedure we term plasma-directed atomic layer depostion (PD-ALD). We start with a nanoporous silica film, consisting of an ordered cubic arrangement of monosized pores, formed by evaporation-induced self-assembly. Following calcination and UV/ozone exposure the nanoporous film has fully hydroxylated 3.2-nm pores as measured by a surface acoustic wave based technique.[40] To avoid ALD on any interior porosity, which would detrimentally increase the membrane thickness, we expose this membrane structure to hexamethydisilazane and then to trimethychlorosilane vapor at 180 °C for 5 minutes. This exposure converts the surface and internal hydroxyl groups to trimethylsiloxane groups, which remain inert to hydrolysis reactions and therefore passivate the surface against ALD during subsequent steps. To activate the immediate surface of the nanoporous film to ALD, the sample is exposed to a remote $Ar+O_2$ plasma for 2 seconds. The plasma conditions are designed so that the Debye length (several mm) is much larger than the pore size. In this condition the plasma radicals cannot penetrate the internal porosity, and only trimethylsiloxane groups residing on the immediate surface of the nanoporous film are converted to silanols ($\equiv$Si-OH). These surface silanols are active to halide and alkoxide ALD precursors, $M(X)_n$ and $M(OR)_n$, respectively, undergoing condensation reactions to form $\equiv$Si-O-M$\equiv$ plus HX and HOR byproducts. Therefore, ALD takes place on the surface of the film, while internal, hydrophobic $-Si(CH_3)_3$ groups remain unhydrolyzed and do not undergo condensation reactions with ALD precursors.

Figure 2.5 contrasts PD-ALD with conventional two-stage ALD. In **Figure 2.5 A-C**, titania was uniformly deposited throughout a mesoporous silica film deposited by EISA using two stages of $TiCl_4$ exposure and purging (long/short) followed by two stages of water exposure and purging (long/short). As shown in the schematic we can combine silane coupling chemistry with TiO_2 ALD to arrive at a wide spectrum of chemistries of interest to both transport and catalysis. In contrast to this two-stage thermal ALD process, PD-ALD allows spatially localized ALD deposition with 0.03-nm dimensional control. Depending on the plasma parameters and the pore dimension, the penetration depth can be 4 nm or smaller. This PD-ALD process could localize the formation of a transport limiting aperture at the entrance to a pore (**Figure 2.5 D-F**).

Using PD-ALD, we developed a high flux, high selectivity membrane by an approach combining remote plasma exposure and surface passivation with conventional ALD of an (unconventional) hybrid precursor. In the case of passivated internal porosity, successive steps of adsorption and hydrolysis of $M(X)_n$ and $M(OR)_n$ precursors first reduce the size of surface nanopores and then, when the film thickness exceeds the original pore radius, progressively seal the surface. If molecular-sized pore templates, so-called porogens, could be introduced within a dense, ultrathin sealing layer, their removal would create a corresponding ultrathin microporous membrane with controlled pore size and shape.[41, 42] Introduction of organic templates using organosilanes R_xSiX_{4-x} is rather straightforward and has been demonstrated previously.[42] However, in this case the condensation reactions position the organic ligands R on the external surface, where they passivate it toward further ALD. Additionally, the coverage of R groups must be sufficiently low so as to avoid association of multiple R groups, which when removed, would create larger and more polydisperse pores than individual R groups. To resolve these problems, we used an

organically bridged silsesquioxane (RO)$_3$Si-R'-Si(OR)$_3$ as an ALD precursor. In this case the R' unit, which serves as the pore template, is incorporated uniformly within the developing siloxane framework, avoiding passivation of the surface and reducing template aggregation. Here, we used BTEE (bis(triethoxysilyl)ethane, (C$_2$H$_5$O)$_3$-Si-C$_2$H$_4$-Si-(OC$_2$H$_5$)$_3$) as our bridged ALD precursor. Following remote plasma exposure to activate the nanoporous substrate, ALD was performed in a
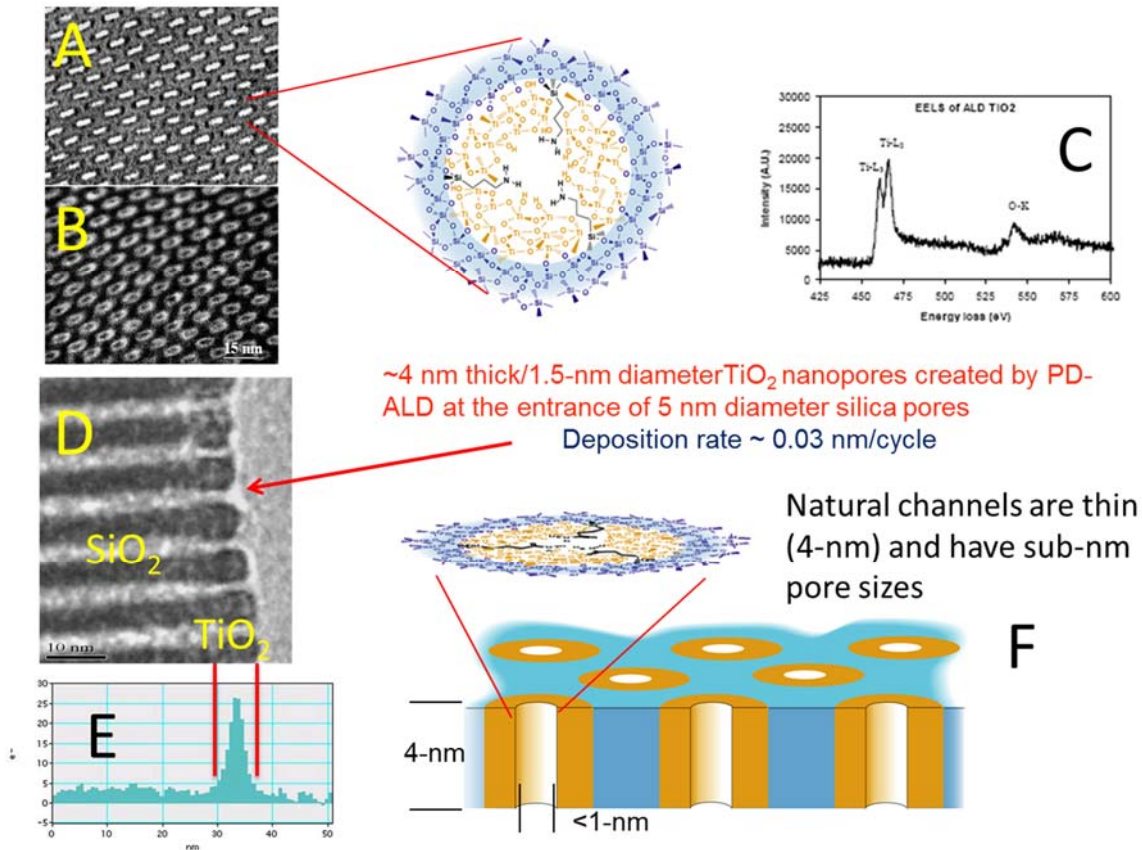
Figure 2.5. Comparison between thermal ALD and PD- ALD. A) TEM image of nanoporous network modified by TiO$_2$ thermal ALD. The dark rims on the pores (white) are TiO$_2$ ALD on pore surfaces; B) EELS mapping of Titanium in the same area, where Ti gives bright contrast. The bright rings in this image show that the dark rims in above image correspond to titania; C) EELS for the same area, confirming the deposition is TiO$_2$. D) TEM image of nanoporous network modified by PD-ALD, showing ALD was localized at the pore entrance vicinity; E) corresponding Ti- EELS profile; F) schematic of a bio-mimetic channel with 4-nm effective membrane thickness and sub-nm pore diameter.

home-built reactor according to the following steps: 1) evacuate ALD chamber to a base vacuum of 10^{-6} Torr; 2) inject BTEE vapor, causing BTEE molecules to condense with surface ≡Si–OH groups; 3) purge chamber with Ar to remove all non-condensed BTEE and condensation by-products; 4) inject water vapor to hydrolyze the ethoxysilane groups of chemisorbed BTEE; 5) purge chamber with Ar to remove residual water vapor and ethanol by-products; 6) repeat steps 2-5 to obtain desired thickness.

Figure 2.6 shows a representative cross-sectional TEM image of the nanoporous supported ALD film prepared by 300 cycles of ALD with BTEE (each cycle comprising steps 2-5 above) followed by UV/ozone exposure to remove the organic C_2 template. The film is ultra-thin (~5-nm thick) and smooth and spans the ~3-nm diameter pores of the underlying support. Comparison of the higher magnification images **Figure 2.6b** (support prior to ALD) and **Figure 2.6c** (support after ALD) shows that the film is confined to the immediate surface of the support with no evidence of penetration into the nanoporous sublayer. **Figure 2.6d** shows the electron energy loss spectrum (EELS) of the as-deposited ALD film. Prior to EELS, the sample was cleaned in a plasma oxidizer to remove any carbon contamination on the sample surface as well as epoxy used for cross-sectional sample preparation. The energy loss edges at 104~160 eV, 286 eV, and 540 eV are attributed to Si, C, and O, repsectively. The absence of a shoulder edge at ~282 eV indicates that the carbon is mainly σ-bonded as expected from the bridging ethylene group in the BTEE precursor.
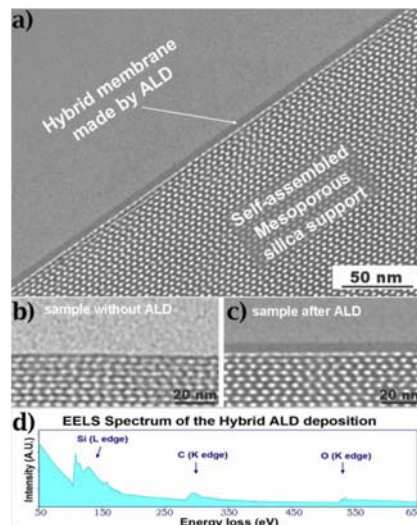
Figure 2.6. a) Cross-sectional TEM image of a hybrid membrane supported on mesoporous silica; b) original mesoporous silica support; c) support coated with ALD membrane; d) EELS spectrum of the membrane.

To demonstrate the efficacy of this approach to form selective membranes, the organic template was removed by 30s of UV/ozone exposure and the permeance of the film to the series of gases He, N_2, and SF_6 was measured at room temperature using standard techniques. **Figure 2.7** shows the gas permeances and selectivities of the samples after differing numbers of ALD cycles. The original porous support had a He permeance of 171cc/bar-cm^2-min and He/N_2 selectivity and He/SF_6 selectivity of 2.08 and 4.28, consistent with Knudsen diffusion. With increasing cycle

Figure 2.7. Gas permeances of ALD membranes to He, N_2 and SF_6 with kinetic diameters of 2.2, 3.6 and 5.5Å, respectively.

numbers the permeance decreased and, after 100 cycles, the selectivity increased logarithmically. These results are consistent with the requirement to form a defect-free, pore-spanning sealing layer of several nanometer thickness prior to template removal. Due to the thinness of the membrane, after 200 ALD cycles, the He permeance was a very remarkable 5.3 cc/bar-cm^2-min, and the He/N_2 and He/SF_6 selectivities exceeded 10^3 and 10^4, respectively.

2.4.2 Achieving precisely tunable nanopores by ALD [Chen Z, et al. DNA translocation through an array of kinked nanopores. Nature Materials 9: 667-75, 2010] Combining EISA and PD-ALD, we demonstrated the formation of 'kinked' silica nanopores and their further tuning and chemical derivatization using atomic-layer deposition (**Figure 2.8**).[43] A thin (25 nm) porous film was coated over a ca. 100 nm hole in a Si_3N_4 membrane formed by fast atom bombardment; GISAXS analysis showed the film to be comprised principally of *bcc* arranged pores, (**Figure 2.8B**) forming a 'kinked' transport pathway through the film through connectivity of the pores (**Figure 2.8C**). DNA translocation through this film was measured using a patch clamp apparatus (**Figure 2.8D**). Compared with 'straight through' proteinaceous nanopores of comparable dimensions, kinked nanopores exhibit up to fivefold reduction in translocation velocity, which has been identified as one of the critical issues in DNA sequencing. Additionally, we demonstrated an efficient two-step ALD modification approach to create a nanopore array exhibiting nearly perfect selectivity for ssDNA over dsDNA. We showed that a coarse-grained drift–diffusion theory with a sawtooth-like potential could reasonably describe the velocity and translocation time of DNA through the pore. By accounting for pore size, length and shape, the model captured the main functional behaviors of protein pores in our solid-state nanopore system.

2.4.3 An Inorganic-Organic Proton Exchange Membrane for Fuel Cells with a Controlled Nanoscale Pore Structure formed by ALD (collaboration with S. Moghaddam and M. Shannon (UIUC), Moghaddam S, et al. An inorganic-organic proton exchange membrane for fuel cells with a controlled nanoscale pore structure. Nature Nanotechnology 5: 230-6, 2010.) Proton exchange membrane (PEM) fuel cells are being extensively studied for applications in energy conversion and storage, but their development has been impeded by problems related to the
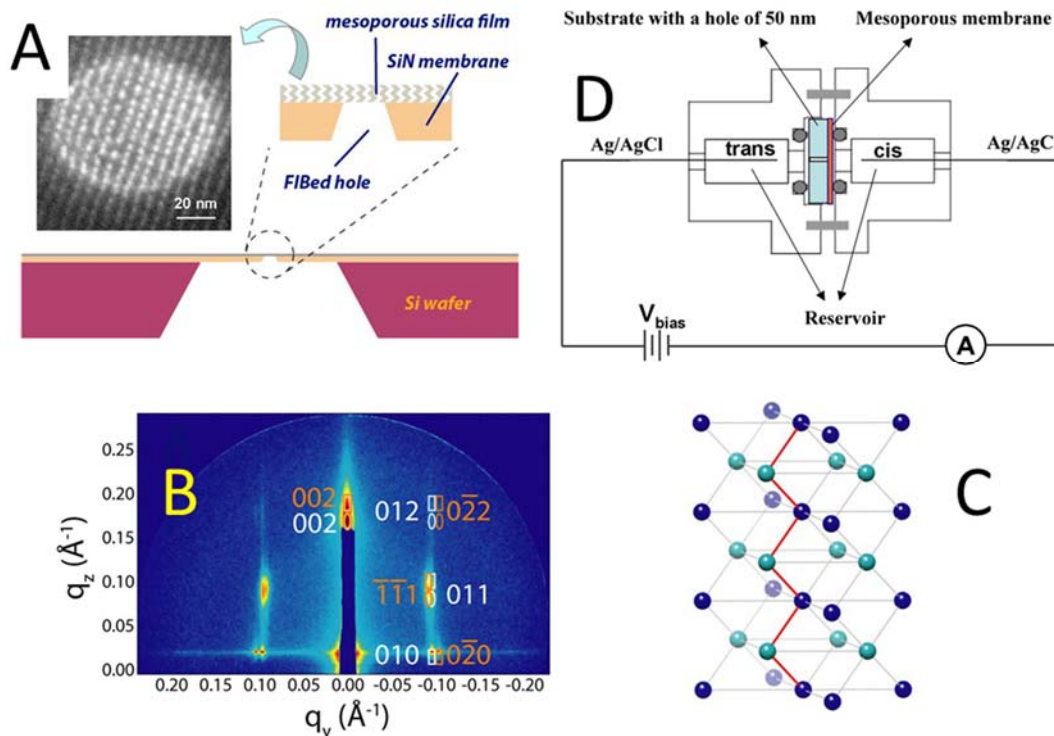
Figure 2.8. A) 25 nm thick nanoporous membrane formed over a FIBed hole in Si_3N_4, B) GISAXS data for a film similar to the one shown in A, indexed to a mixture of bcc and hcp packing of pores, C) Connectivity of pores for bcc packing across a nanoporous membrane, D) Experimental apparatus for measuring DNA translocation across a nanoporous membrane.

membrane electrode assembly (MEA). We recently demonstrated that a silicon-based inorganic-organic membrane offers a number of advantages over Nafion–the most widely used PEM in hydrogen fuel cells - including higher proton conductivity, lack of volumetric size change, and enhanced MEA construction capabilities.[44] The proton conductivity is practically independent of humidity. The inorganic-organic structure is made by fabricating a silicon membrane with ~5-7 nm pores, self-assembly of a molecular monolayer and selective ALD deposition of a hydrophilic aperture at the pore entrances. ALD reduces the diameter of the pores to ~2 nm, ensuring hydration of the pores via capillary condensation and resulting in a proton conductivity 2-3 order of magnitude higher than that of Nafion at low humidity. A MEA constructed with this inorganic-organic proton exchange membrane delivered an order of magnitude higher power density than that achieved previously with a dry hydrogen feed and an air-breathing cathode.

***2.4.4 A Biomimetic Desalination Membrane prepared by combined self-assembly and ALD (2011 R&D100 Award, Biomimetic Membranes for Water Purificat*ion)** We have pursued a new approach to membrane design and development for cheap desalination membranes by approaching the problem at the molecular level of pore design. Our inspiration comes from natural biological channels, which permit faster water transport than current reverse osmosis membranes and selectively pass healthy ions. Combining self-assembly and a new hybrid atomic-layer deposition process we have fabricated membranes exhibiting a 3-fold improvement in water flux over commercial RO membranes that operate at low pressure.

3.0 Research Accomplishments

3.1 Oriented inorganic membrane reactors with transmembrane (along the pore length) control of pore size, surface chemistry, and catalyst location(s) formed by ALD and plasma-assisted and plasma-directed ALD in combination with evaporation induced self-assembly.

We pioneered the formation of a class of ultra-thin flow-through catalytic membrane reactors via ALD deposition within a membrane formed by EISA. Peter Stair, who pioneered this field,[45, 46] refers to this construct as a 'nanolith'. Rather than anodic alumina membranes used by Stair, we have fabricated membranes by EISA that are thinner and have smaller and more controlled pore sizes, which, through definition of silica surfactant space group, have prescribed morphologies other than vertically aligned cylindrical arrays (see 'kinked' pores in **Figure1.1E**). Using different sequences of ALD and plasma-directed ALD (**Figure 3.1**), we have varied the pore size and chemistry of the pore entrance or exit (**Figure 1.2**) along with that of the pore channel and have defined the location of ALD deposition of catalyst NPs or enzymes. The fabrication of such
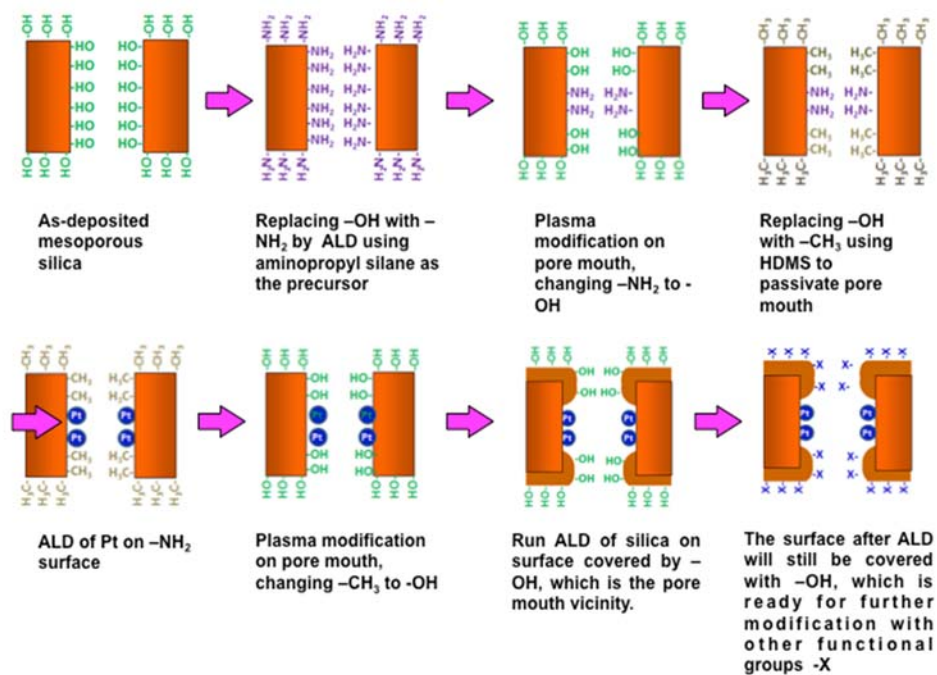
Figure 3.1. Strategies for using different sequences of ALD and plasma-directed ALD to vary pore size and chemistry of the pore entrance or exit of nanoporous membranes along with that of the pore channel, and to define the location of ALD deposition of catalyst NPs or conceivably a spatially defined sequence of NPs.

membrane assemblies is demonstrated in **Figures 1.1D** and **E** and **Figure 1.2** and related references[43] where we show the formation of free-standing membranes and their further modification with ALD to enable nearly perfect voltage-biased translocation of single stranded DNA over double stranded DNA. Similar free-standing membranes have been produced on meso or macroporous substrates such as an anodized aluminum oxide membrane (AAO), or within a lithographically defined channel. As shown in **Figure 3.2A**, performing EISA within AAO results in aligned parallel channels essentially stratifying each AAO pore into many smaller reactors. **Figure 3.2B** shows a reactor design created by EISA within a lithographically designed trench. Both the architectures have been implemented for conducting vapor-phase or liquid phase catalytic reactions. As shown in **Figure 2.5** and described in detail in **Section 2.4.1**, ALD conditions
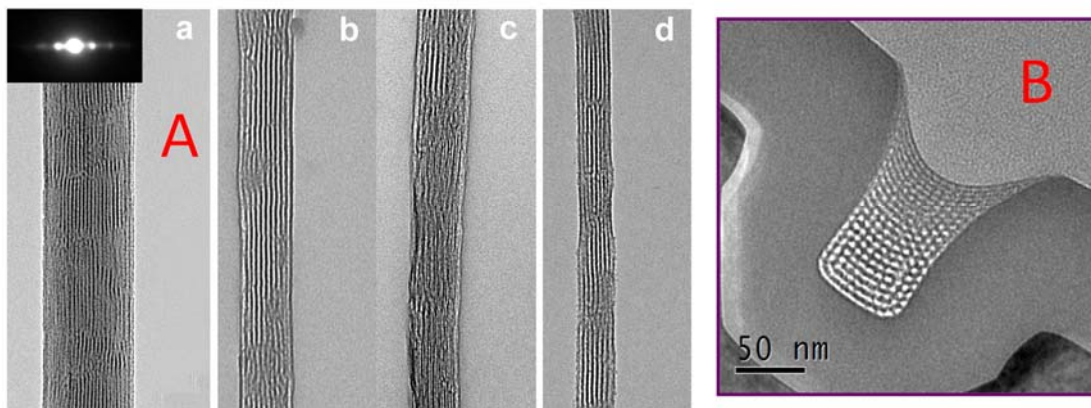
Figure 3.2. A) Aligned nanopore channels deposited within anodized aluminum oxide (AAO) membranes using EISA (a: 200 nm AAO channel, b and c: 120 nm channels, d: 70 nm channel) or B) within a lithographically defined trench.

enabling deposition of uniformly thick, conformal coatings within the nanopore channels is readily achievable. To fabricate asymmetric pore designs, we have developed plasma-directed (PD) ALD, wherein we can selectively modify the pore entrance (see **Figure 2.5A-E**). Importantly for the modification of pore size we have shown that during PD-ALD of silica and titania, deposition rates are ~0.03-nm/cycle compared with about 0.1 nm-cycle for conventional ALD.[19] This allows us to tune the pore opening with a precision not achievable by any other known method. As shown schematically in **Figure 3.1** the strategy for designing the sequence of ALD and plasma-directed ALD steps needed to fabricate the nanochannel reactor geometry involves selective protection and de-protection/activation of deposition sites. Using a remote oxygen plasma where the Debye length (μm) and the molecule mean free path in a typical plasma (μm-mm) greatly exceed the pore

Figure 3.3. Changing ALD processing conditions can alter deposition from conformal amorphous TiO_2 film left to templated single crystal anatase NPs right.

dimension (nm), the plasma cannot penetrate (and ALD cannot occur) within the internal porosity. This allows internal pores to be passivated or functionalized with, e.g., and amine, while the pore entrances are activated by the plasma allowing deposition there. In the schematic the pore is symmetric, but by exposing the cis- and trans- sides of the membrane separately and by using differing oxygen plasma conditions, an unlimited range of asymmetric channel designs is possible. Deposition of catalysts within the channel is possible by ALD. For example, **Figure 3.3** shows 2 nm Pt NPs deposited within oriented silica nanopores and **Figure 3.3** shows that by changing the TiO_2 ALD conditions it is possible to alter the deposition from a conformal film to a single nano-crystal confined within the pore channel.

3.1.1 Ultra-thin enzymatic membrane reactor for CO2 sequestration

Overview - An enzymatically active, ultra-thin, nano-stabilized liquid membrane was developed for CO₂ separation. The separation membrane is an approximately 18-nm thick water layer stabilized by capillary condensation within a hydrophilic mesoporous silica film and embedded with the metalloenzyme carbonic anhydrase, which catalyzes the rapid inter-conversion of $CO_2 + H_2O$ to carbonic acid (HCO_3^-). By minimizing diffusional constraints and stabilizing and concentrating CA within a densely packed array of nanopores, this ultra-thin enzymatic membrane is capable of separating CO₂ at room temperature at a rate of 2600 GPU with CO₂/N₂ and CO₂/H₂ selectivities exceeding 788 and 1500, respectively, the highest combined flux and selectivity yet reported that exceeds for the first time the U.S. Department of Energy standards[1] for CO₂ sequestration technologies.

Carbon dioxide is the most important anthropogenic greenhouse gas in the atmosphere because it accounts for 80% of emissions and, once emitted, can stay in the atmosphere for hundreds of years[47]. 32.2 billion tons of CO_2 were emitted in 2013 due to human activities, and this number is increasing each year[48]. According to the World Meteorological Organization (WMO)'s report in November 2014[49], atmospheric CO_2 reached 142% of the pre-industrial level in 2013, primarily because of emissions from combustion of fossil fuels and the production of cement. With the growing concern about global warming caused by CO_2 emissions, the need for efficient CO_2 separation and capture is imperative. Many countries including the US signed the "Kyoto Protocol" that sets binding obligations on industrialized countries to reduce emissions of greenhouse gases (mainly CO_2 gas), and, in November 2016, the Paris Accord, which aims to maintain a global temperature rise this century less than 2°C above pre-industrial levels, was ratified. However, realization of this goal is presently imperiled by the current and anticipated cost of CO_2 sequestration.

Seventy percent of the cost of capture of CO_2 involves separation from other gases. The conventional process for carbon dioxide capture is by reversible solvent absorption[50],[51], however, this process consumes high amounts of energy [50] and accordingly is costly and has high environmental impact. More efficient and environmentally friendly separation processes are urgently needed. The advantages of membrane-based gas separation include energy efficiency, processability, and low maintenance costs, making membranes attractive for carbon dioxide capture[51-53]. In particular, the development of a membrane separator for the selective and efficient removal of CO_2 in the presence of CO, H_2, H_2O, and H_2S (fuel gas) or N_2, O_2, H_2O, SO_2, NOx, and HCl (flue gas) would be of tremendous economic value[54].

Membrane Design - Two metrics define membrane performance, permeance; that is the flux of a specific gas through the membrane, typically reported in units of GPU($1 GPU=10^{-6}$ cm^3 (STP)/cm^2-s-cmHg) and selectivity; the membrane's ability to pass one gas species relative to another, typically reported as a dimensionless ratio of flux. An efficient membrane should have both high permeance and selectivity. Porous membranes usually exhibit a high CO_2 flux but, due to their pore size variability, they often exhibit poor selectivity that depends further on the composition of other gases in the CO_2 mixture. Dense membranes, typically polymers, often exhibit high selectivity, but the CO_2 flux is in general very low because of the low solubility and diffusivity of CO_2 within the nominally dense membrane material. In general, most existing[47, 52] membranes exhibit a sharp 'trade-off' between flux and selectivity and are so far impractical for CO_2 capture applications. Therefore, there remains an urgent unmet need to develop a new membrane technology with combined high CO_2 flux and high CO_2 selectivity.

Three factors govern flux and selectivity of any membrane: 1) how fast the species to be separated can enter into or exit from the membrane, 2) how selectively the species to be separated can enter into or exit from the membrane, and 3) how fast the species to be separated can be

transported through the thickness of the membrane. Not surprisingly biological systems have evolved to maximize the combination of these three factors: in biological systems, separation processes typically take place in a liquid medium through an ultra-thin layer aided by enzymes. Enzymes catalyze the selective and rapid dissolution and regeneration of the target species; short diffusion distances combined with the inherent three orders of magnitude higher diffusivity within liquid versus solid media maximize transport rates. For CO_2 in particular, the respiratory system of vertebrates is an excellent case in point. Red blood cells employ the enzyme, carbonic anhydrase, to rapidly and selectively dissolve CO_2 produced by tissue and regenerate CO_2 exhaled from the lung.

Carbonic anhydrases (**Figure 3.1.1**) represent a family of metalloenzymes that catalyze the rapid interconversion of CO_2 and water to carbonic acid H_2CO_3, which dissociates to bicarbonate (HCO_3^-) and protons:

$$CO_2 + H_2O \Leftrightarrow H_2CO_3 \Leftrightarrow HCO_3^- + H^+ \quad (1)$$
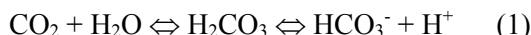
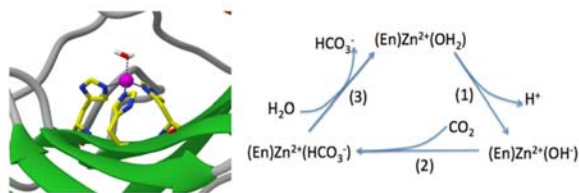via the cycle depicted in **Figure 3.1.1**, according to the prevailing species concentrations. This reaction serves to maintain the acid-base balance in blood and to actively control the concentration of CO_2 in the respiratory system of mammals. Carbonic anhydrases are necessarily one of the 'fastest' enzymes, where reported catalytic rates range from 10^4 to 10^6 reactions per second depending on the specific CA family, meaning that one molecule of CA can catalyze the hydration/dissolution of 10,000 to 1,000,000 molecules of CO_2 per second[55, 56].

The concept of employing CA for CO_2 separation in an 'immobilized liquid' membrane was first reported by Ward and Robb who impregnated a cellulose acetate film with a 2N potassium bicarbonate solution containing 2 g/L of carbonic anhydrase and observed a factor of 6 increase in CO_2 permeability over potassium bicarbonate alone[57]. Given the 0.007-cm effective thickness of their membrane, the actual CO_2 flux/per unit area (i.e. the CO_2 permeance) was not very

Figure 3.1.1. (Left): Active site of carbonic anhydrase determined by molecular simulations (*vide infra*). A zinc ion (Zn^{2+}, purple sphere) surrounded by three coordinating histidines and a water molecule comprises the active site. (Right): The overall catalytic cycle for CO_2 hydration to HCO_3^- with zinc as the metal in the enzyme "(En)" active site depicted. This reaction is driven by the concentration gradient: clockwise when the CO_2 concentration is greater than HCO_3^- and counterclockwise when more HCO_3^- is present. Deprotonation of the zinc-bound water in Step (1) is thought to be rate limiting.

impressive: only 30 GPU (gas permeance = gas permeability / membrane thickness). However, the CO_2 permeability of the membrane (214×10^{-9}) was exceptional: about 2 orders of magnitude higher than solid polymer membranes (typically $2\text{-}3 \times 10^{-9}$)[53, 57]. Based on a similar concept, Carbozyme Inc developed a 'contained liquid membrane' (CLM) by encapsulating an aqueous CA solution layer within a "microporous polypropylene hollow fiber membrane mat"[56, 58], where the minimum membrane thickness was established by the fiber diameter (~100 µm). 5 times higher CO_2 permeability was observed in Carbozyme's CLM compared to Ward and Robb's membrane, presumably due to the reduced effective membrane thickness,

However, the CO_2 flux (reported to be $1\text{~}5 \times 10^{-8}$ mol/m^2·ol/m[11], corresponding to a permeance of 30~150 GPU) still fell far short of that needed for practical CO_2 sequestration (e.g. a CO_2 capture cost < \$20-40/ton as required by US Department of Energy, which translates to a CO_2/N_2 selectivity > 30-50 and CO_2 permeance > 300-3000 GPU)[59, 60]. Inherent

problems/limitations of carbonic anhydrase catalyzed 'immobilized' or 'contained' liquid membranes developed to date are thickness (of the order $10 - 100$ μm,), which establishes the diffusion length and limits/governs the flux, and the CA concentration, which governs the CO_2 dissolution and regeneration rates but is limited in current membranes by the enzyme solubility (typically < 1mM).

Here, in order to overcome the limitations of current CO_2 membranes and for the first time exceed the DOE requirements for CO_2 sequestration, we have developed an ultra-thin, CA-catalyzed, nano-stabilized liquid membrane for CO_2 separation (see **Figure 3.1.2**). It comprises oriented close-packed arrays of 8-nm diameter hydrophilic cylindrical nanopores, whose effective thickness (i.e. the hydrophilic pore length) is defined by oxygen plasma treatment to be ~18-nm. Through capillary condensation the pores are filled with carbonic anhydrase enzymes stabilized within water channels by nano-confinement. Due to the exceptional thinness of the membrane and the high effective concentration of CA within the close-packed arrangement of nanopores, we demonstrate unprecedented values of combined CO_2 flux (up to 2600GPU) and CO_2/N_2 selectivity (> 500).
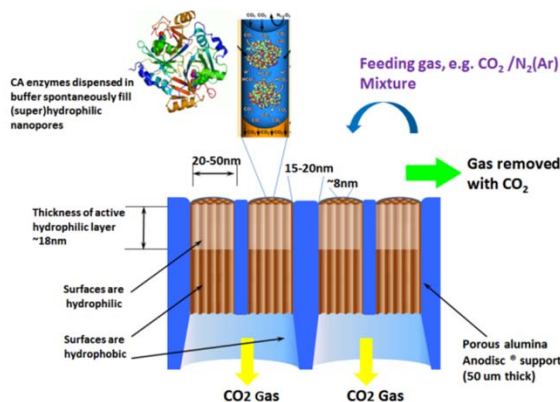
Figure 3.1.2. Design of ultra-thin, biomimetic liquid membrane for CO_2 separation – CA enzymes are stabilized within ~8 x18-nm cylindrical hydrophilic liquid-filled pores and catalyze rapid, selective CO_2 dissolution and regeneration. The high effective CA concentration and membrane thinness result in combined high CO_2 flux and selectivity.

Results

Fabrication of ultra-thin hydrophilic nanoporous membrane

The membrane was fabricated on a commercial, asymmetric Anodisc^TM porous alumina support purchased from Whatman International Ltd. The support is 60μm thick and is composed of oriented asymmetric vertical channels that are perpendicular to the disc surface. The channel diameters taper from 200-nm in diameter on the bottom surface to 20-40-nm in diameter on the top surface (see **Figure 3.1.3**). To create an architecture that both stabilizes water and can accommodate CA enzymes (*vide infra*) the oriented Anodisc^TM pores were sub-divided into smaller, 8-nm diameter pores via deposition of P123 block copolymer templated mesoporous silica using 'Evaporation-Induced Self-Assembly" (EISA, see Materials and Methods and [61, 62]). In this process the Anodisc^TM pore channels are filled to a depth of about 1μm with a cylindrical hexagonal P123/silica mesophase (space group p6mm), which when confined to a cylindrical channel orients parallel to the channel axis. Calcination at 400°C is used to remove the P123 template resulting in oriented 8-nm diameter nanopores (see **Figure 3.1.3 b-d**) whose pore surfaces are terminated with
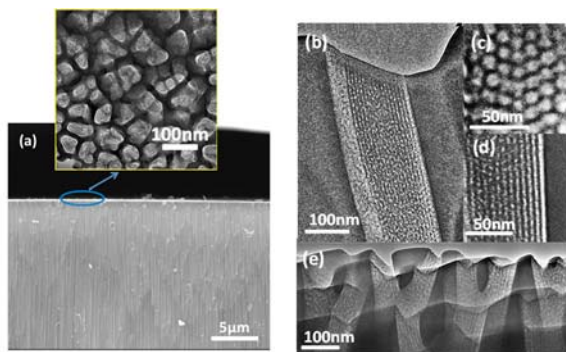
Figure 3.1.3. Micro- and nanostructure of the hierarchical, asymmetric membrane. (a) Cross-sectional SEM image of Anodisc[TM] support showing oriented ~50-nm pore channels near the top surface; Inset: Plan-view TEM image of FIBed Anodisc[TM] surface showing complete filling of all Anodisc[TM] pores channels with ordered arrays of silica nanopores. (b-d) Cross-sectional TEM images of Anodisc[TM] surface showing oriented arrays of 8-nm diameter cylindrical pores. (e) lower magnification cross-sectional view of silica nanopore array.

hydrophilic surface silanol groups ($\equiv$Si-OH). Hydrophilic 8-nm diameter nanopores are large enough to accommodate CA (~5.5-nm in diameter) within a confined water layer and small enough to spontaneously fill with water above ~80%RH (*vide infra*). However, the thickness of the resulting nano-stabilized water membrane would be ~1-μm far exceeding that of natural membranes. To reduce the effective thickness of the nano-stabilized water membrane, we conducted two steps of surface modification (see **Figure 3.1.4**). First, using an atomic layer deposition apparatus, we treated the membrane with ozone to maximize the surface silanol coverage and then conducted 5 cycles of alternating hexamethyldisilizane (HMDS) + trimethylchlorosilane (TMCS)/H_2O vapor exposures to quantitatively replace hydrophilic surface silanol groups with hydrophobic tri-methylsilyl groups ($Si(CH_3)_3$) (see **Figure 3.1.4**). Second, we exposed the membrane to a remote oxygen plasma for 5 seconds to re-convert hydrophobic trimethylsilyl groups to hydrophilic silanol groups at the immediate membrane surface. The mechanism of this plasma-nanopore-modification has been described by us previously[62, 63]: Briefly, reactive radicals generated in a low-pressure oxygen plasma are mainly charged ions that cannot penetrate deeply into the nanoporous support, because the plasma Debye length (~20-cm under our conditions) is much larger than the pore size (~8-nm). To confirm the hydrophilicity of the plasma-modified nanoporous membrane surface and the hydrophobicity of the HMDS-modified surface, the water contact angle was measured with a Biolin Scientific Theta Optical Tensiometer. **Figure 3.1.4c** shows the hydrophilic surface to have a contact angle of nearly 0° (note since the water droplet for the measurement is about 0.05ml, not all water can be adsorbed by the nanopores, and some excessive free water remains on the surface) consistent with a superhydrophilic surface stemming from the hydrophilic surface chemistry and nanoscale roughness[64]. In comparison the water contact angle of the HMDS modified surface was ~150° consistent with a superhydrophobic surface stemming from the hydrophobic surface chemistry plus nanoscale roughness[65].

To estimate the depth of the hydrophilic plasma-modified surface layer, we compared TiO_2 atomic layer deposition (ALD) on the original hydrophilic mesoporous silica membrane with TiO_2 ALD on the HMDS plus oxygen plasma-modified membrane, using conventional $TiCl_4$ and H_2O vapor as the TiO_2 ALD precursors. It is well established that TiO_2 ALD requires a hydrophilic (normally hydroxylated) surface to initiate deposition, therefore the formation of TiO_2 can be used as a 'marker' of the hydrophilic surface chemistry. **Figure 3.1.4b** shows EDS-based Ti elemental mapping of cross-sectional samples, where the brightness corresponds to the Ti concentration. The top panel is a cross-section of the original mesoporous silica membrane, where we observe Ti deposition throughout the ~250-nm thick section (membrane top surface is on left) as expected from the hydroxylated surface chemistry. The bottom panel shows that Ti ALD on the HMDS + plasma-modified membrane is confined to an approximately 18-nm thick region on the immediate surface – this depth establishes the effective thickness of the confined water membrane to be only 18-nm *vide infra*.
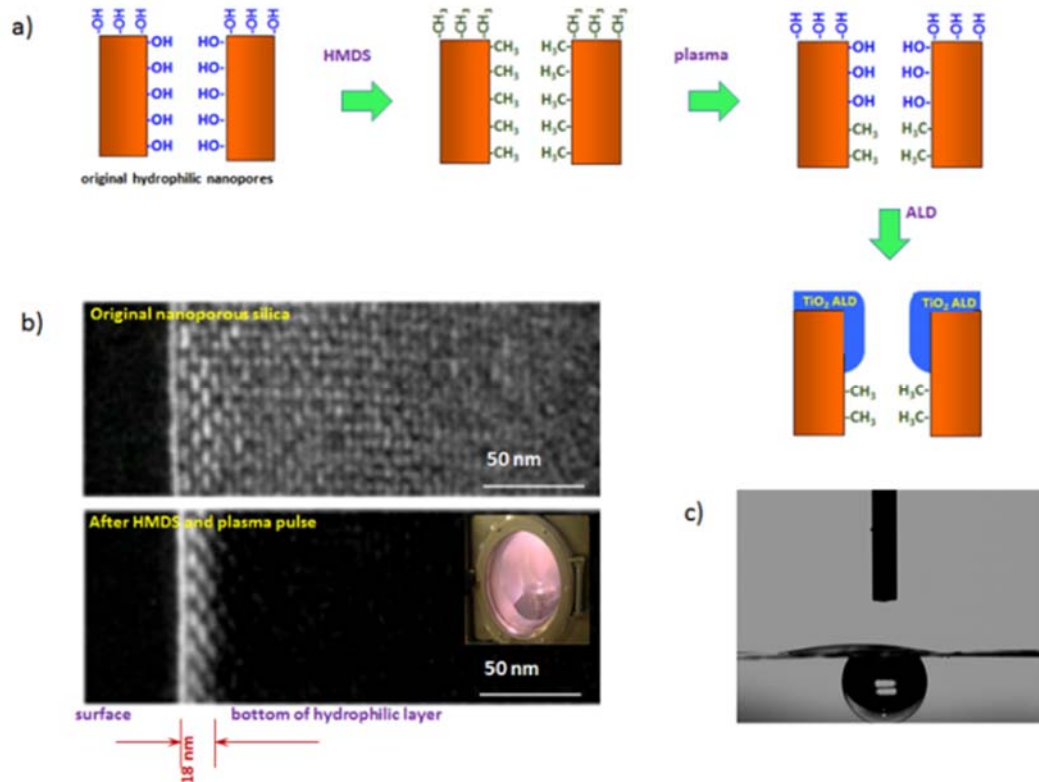
Figure 3.1.4 Schematic showing the stepwise modification process used to create an ultrathin hydrophilic nanoporous surface. a) the original silanol terminated mesoporous silica membrane is reacted with alternating cycles of HMDS+TMCS and water vapor using ALD to replace Si-OH with Si-Si(CH$_3$)$_3$ groups. A remote short pulse of oxygen plasma is used to re-convert surface Si-Si(CH$_3$)$_3$ groups back to Si-OH groups at the immediate membrane surface, which enables localized TiO$_2$ deposition using alternating TiCl$_4$/H$_2$O exposures. b) Cross-sectional TEM image of Ti-mapping where titania ALD is used as a High Z electron imaging agent to identify/map hydrophilic regions of the membrane that support titania ALD. (Top image): Titania modification occurs throughout the original hydrophilic silanol terminated nanoporous membrane, but, after HMDS plus plasma treatment, the hydrophilic region is shown to be confined to the top 18-nm thickness of the membrane (bottom); c) Photograph of water droplets dispensed on the anodic alumina membrane prepared with a thin hydrophilic mesoporous silica film surface via plasma treatment (top surface) compared to the hydrophobic trimethylsily terminated anodic alumina film surface (bottom surface) demonstrating contrasting superhydrophilic and superhydrophobic surface properties.

Formation of sub-20nm thick enzymatic membrane reactor.

Having successfully fabricated an ultra-thin hydrophilic nanoporous layer on the hydrophobic support, we next introduced CA enzymes into the hydrophilic nanopores by simple immersion of the sample in an aqueous enzyme solution with a CA concentration of 0.05 mM. After moderate bath sonication for 10 minutes, the sample was withdrawn from the solution and allowed to 'dry' in a horizontal configuration. During this evaporation process, the CA enzyme solution is concentrated and stabilized within the hydrophilic nanopores via capillary forces to form an ultrathin water membrane containing CA enzymes. Since the superhydrophobic pores repel water, the thickness of the CA containing water membrane is defined by the thickness of the hydrophilic nanoporous layer, which was determined to be about 18 nm (**Figure 3.1.4**).

Direct observation of the formation and thickness of the water membrane is challenging. However, by measurement of the mass of water adsorbed within a defined area of the hydrophilic nanoporous membrane, we can calculate the effective water membrane thickness according to its geometry. To perform this experiment, we used a quartz crystal microbalance (QCM) to measure the mass of water adsorbed within the nanoporous membrane deposited onto the active area of the QCM and processed identically to the membrane deposited on the AO support, i.e. by HMDS/TMCS ALD followed by plasma processing. To confirm the structural similarity of the films deposited on the QCM and AO support surfaces, we performed grazing incidence small angle scattering (GISAXS). **Fig. 3.1.5a-b** compares the respective GISAX data where we observe nearly identical patterns confirming the structural similarity of the samples. Next we placed coated QCM devices into an environmental chamber and performed water adsorption isotherms. **Figure 3.1.5d** compares the H_2O adsorption isotherms of nanoporous silica films processed before and after plasma processing, where 0% RH corresponds to samples purged using pure dry N_2 for more than 1 hr. For the original HMDS hydrophobic nanoporous silica membrane (referred to as 'before plasma irradiation' in **Figure 3.1.5d**), the mass of the sample shows a small increase with increasing RH, probably due to water vapor adsorption by randomly scattered hydrophilic micropores that are inaccessible to HMDS/TMCS molecules during ALD. For the hydrophilic membrane prepared by HMDS/TMCS ALD followed by plasma irradiation (referred to as 'after plasma irradiation' in **Figure 3.1.5d**), the mass of water adsorbed increases abruptly at about 80% RH consistent with spontaneous water absorption by capillary condensation and the formation of the nanostabilized water membrane (*vide infra*). The 4.82 µg mass increment at RH=80% corresponds to a volume of 4.82×10^{-6} cm^3 of water. Assuming a 50 % volumetric porosity of the membrane (as is typical for P123 templated mesoporous silica) and using the geometric surface area of 4.91 cm^2 for the 25mm diameter QCM sensor, we calculate the corresponding water layer thickness to be 19.6nm. Further considering the fact that some water can still be adsorbed within the hydrophobic regions due to isolated hydrophilic microporosity, the actual thickness of the water membrane is estimated to be slightly under 20nm, which is in good agreement with the 18nm thickness observed according to the TiO_2-ALD experiments (**Figure 3.1.4**).
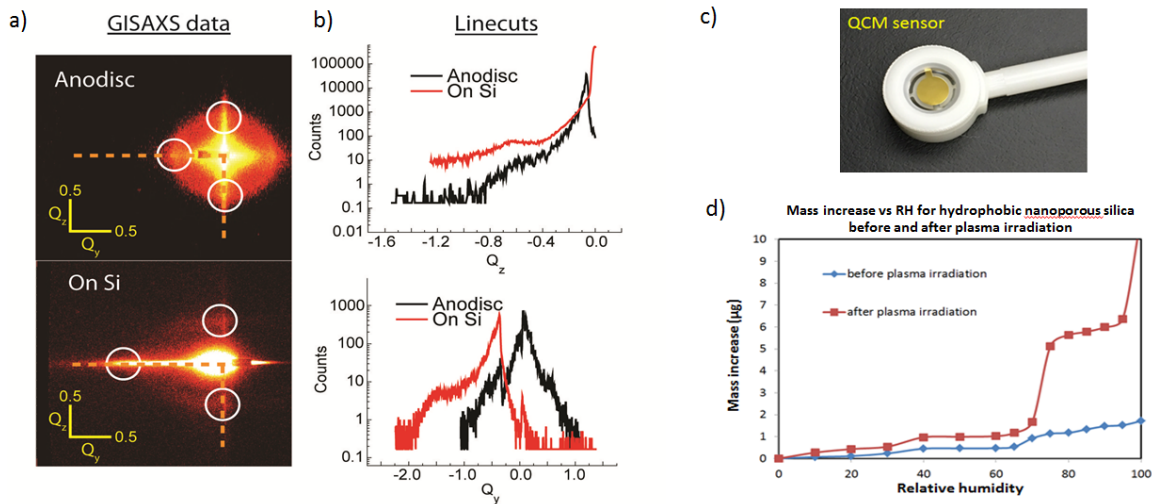
Figure 3.1.5 a) GISAX data showing the nanoporous silica within AO channels and the nanoporous silica on Si surface have the same porous structure; b) Linecut of GISAXS showing the similarity of two samples; c) Picture of 25mm diameter QCM sensor coated with nanoporous silica; d) QCM measurement results on mass increase of a completely hydrophobic nanoporous silica sample (blue plot) and the same hydrophobic nanoporous silica sample but plasma-treated with the ultra-thin hydrophilic layer (red plot) due to capillary condensation of water vapor at various humidity values. The amount of condensed water vapor indicates the volume thereby the thickness of the ultra-thin hydrophilic layer.

To prove the formation and the "air-tightness" of the membrane, the permeance of N_2 (maintained at 95% RH humidity) through the membrane (prepared as described above) was measured using a bubble flow rate meter for a 1 atm pressure difference. The permeance of N_2 through the membrane was almost undetectable, whereas, in contrast, the N_2 permeance through the completely hydrophobic sample (i.e. prepared without plasma irradiation and thereby having no stabilized water layer) was measured to be 340 sccm/cm^2-atm. This indicates that the ultra-thin CA containing water membrane is continuous and essentially defect-free. One conceivable concern might be how to ensure that the water membrane is stable and will not 'dry out' in real world applications. As previously discussed, this concern will be alleviated by maintaining the membrane at a sufficient relative humidity where, due to capillary condensation, the uniformly sized hydrophilic nanopores remain water-filled. According to the Kelvin equation, capillary condensation for a hydrophilic pore occurs at a relative humidity RH defined by: $ln(RH)=-(2\gamma V_m/rRT)$, where γ and V_m are the surface tension and the molar volume of water, r is the pore radius, T is the temperature in Kelvin, and R=8.32 J mol^{-1} K^{-1}. For the 8-nm diameter pores of our membrane, the Kelvin equation predicts condensation to occur at a RH equal to or exceeding 80% which is consistent with the water adsorption 'step' observed in **Figure 3.1.5d**. A typical flue gas comprises 6.2wt% H_2O if it is from a coal-fired plant, and 14.6wt% H_2O if from a gas-fired plant. Both are much higher than the saturated water vapor concentration at 40°C (~50g H_2O/kg air or 0.5wt% H_2O). Therefore, the humidity requirement to maintain membrane stability can be easily satisfied if the membrane is used to capture CO_2 from power plant flue gas.

Another potential concern is that of the water membrane strength, e.g. will the water membrane be ruptured when applying pressurized gas for separation? Again, the consistent nano-sized dimensions of the hydrophilic pores assure mechanical stability: the capillary force of water embedded within a small pore can be calculated according to P = $2\gamma cos\theta/r$, and for water confined within 8nm diameter hydrophilic pores where the contact angle θ = 0, the capillary force is about 35 atm. Therefore at regular operations, where the gas pressure is typically less than several atmospheres, the capillary force is large enough to stabilize the membrane and prevent its displacement into the hydrophobic portion of the membrane nanopores.

Enzymatic, nano-stabilized water membrane performance

So far, we have demonstrated an 'air-tight', ultra-thin, stable, enzyme-containing water membrane formed on an AO support. CO_2 permeance of the enzymatic water membrane thus fabricated was measured at various temperatures and pH values (**Figure 3.1.6a-b**). The permeance was found to be not only dependent on the pH and temperature, but also to be strongly dependent upon the type and the source of the CA enzyme. We then determined and compared our best-observed CO_2/N_2 separation efficiency and CO_2 flux performance with other as-reported CO_2 membranes, and the corresponding data are plotted in **Figure 3.1.6f**.

Figure 3.1.6a compares the CO_2 permeances at different temperatures for two types of carbonic anhydrase enzymes: CA derived from mammalian bovine erythrocytes and the CA from *Desulfovibrio vulgaris* – an extremophile bacteria that evolved to survive under conditions of 5°C and pH 10. For the Bovine CA enzyme, the permeance, resulting from CA mediated CO_2 dissolution (Eq. 1) followed by diffusion across the 18-nm thick water membrane and ex-solution (reverse of Eq. 1) at the hydrophobic interface is temperature dependent and, as expected, is maximized at mammalian body temperature, 30-40 °C. For membranes containing the *Desulfovibrio vulgaris* CA enzyme, the CO_2 permeance is practically temperature independent exceeding that of the bovine CA membrane at low and high temperatures but found to be less than that of bovine CA at 30-40 °C. Our observed temperature dependent CA activity is in good agreement with that reported by Hooks and Rehm et al.[66]. **Figure 3.1.6b** plots CO_2 permeance as a

function of pH for bovine CA membranes and *Desulfovibrio vulgaris* CA membranes. Similar to the temperature dependence, the bovine CA membranes performed best at neutral pH, whereas the *Desulfovibrio vulgaris* CA membranes had a very moderate pH dependence over the pH range 2-10 and exhibited higher CO_2 permeance at both lower and higher pH.
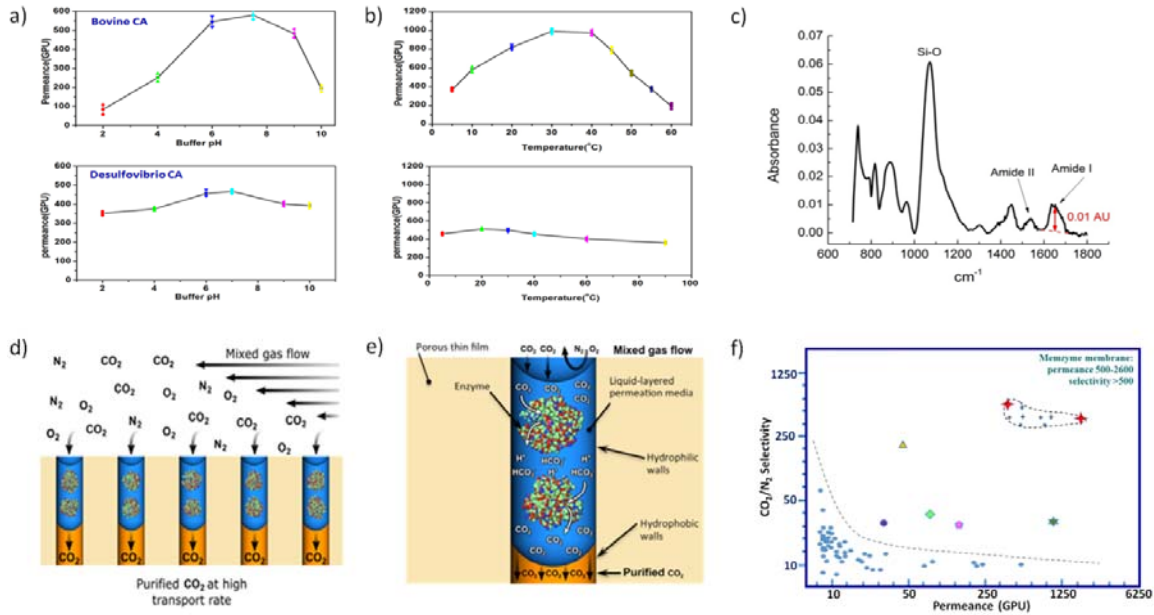
Figure 3.1.6 a) Comparison of the CO_2 permeance vs temperature for the enzymatic water membranes prepared using Bovine or *Desulfovibrio vulgaris* CA enzymes, where the stabilized water layer is composed of water and enzyme; b) Comparison of the CO_2 permeance vs pH for the enzymatic water membranes prepared using Bovine or *Desulfovibrio vulgaris* CA enzymes, where the stabilized water layer is composed of buffered electrolytes; c) FTIR spectrum of the enzyme-embedded hydrophilic nanoporous silica layer, indicating an effective areal density of 8.0×10^{11} CA/cm^2 that is consistent with the loading of 2-enzymes per nanopore; d) schematic of the model structure for selective CO_2 transport; e) Zoom-in schematic of the model structure for selective CO_2 transport; f) CO_2/N_2 selectivity vs CO_2 permeance of the enzymatic water membrane compared with other membranes. The red stars indicate membranes showing the highest measured selectivity or flux and the bounded area represents the range of selectivity and permeance obtained for all membranes (with representative data shown). The red stars are performance for our ultra-thin enzymatic water membrane; the orange triangle is the performance for the Carbozyme CA membrane[19]; the blue dots, the purple circle, the green prism, the pink pentagon, and the blue star are CO_2 membrane performance data from references 8, and 20 – ref 24 respectively.

Figure 3.1.6f compares the CO_2 separation and permeance performance of our ultra-thin enzymatic water membrane with that of other classes of CO_2 membranes. Most types of membranes do not have sufficient permeance to satisfy practical CO_2 separation requirements. In addition, there is always a sharp compromise between permeance and selectivity. In contrast, our ultra-thin enzymatic water membrane exhibits an unprecedented combination of high CO_2 permeance (up to 2600 GPU) and high CO_2/N_2 selectivity (>500). To explain the enhanced performance of our CA catalytic membrane we must reconsider the factors govern flux and selectivity of any membrane: 1) how fast the species to be separated can enter into or exit from the membrane, 2) how selectively the species to be separated can enter into or exit from the membrane, and 3) how fast the species to be separated can be transported through the thickness of the membrane. In our case CA enzymes catalyze the selective and rapid dissolution and regeneration of the target species; short diffusion distances combined with the inherent three orders of magnitude higher diffusivity within liquid versus polymers commonly used for CO_2 membranes[52, 56] maximize transport rates. Water

membranes containing CA have been reported previously for CO_2 separation by Ward and Robb et al in the 1960's[56] and more recently by Carbozyme Inc.[67]. However, the inherent mechanical weakness of the water layer in their membrane configurations limited their membrane thicknesses, to be only as thin as 10-100 microns, a hundred times thicker than most polymer membranes, therefore negating the potential advantage of the water membrane compared to a polymer membrane. Here through nanoconfinement we have created a mechanically stable water membrane only ~18-nm thick. Furthermore, compared to the Ward and Robb and Carbozyme membranes another advantage of our membrane is the high enzyme concentration achieved by confinement within the close packed array of hydrophilic nanopores (see **Figure 3.1.3**). CA enzyme solubility in water membranes is in general lower than 0.2 mM. For example, Carbozyme was able to use a CA concentration of 0.16 mM (5 g/l) and Ward and Robb et al were able to use a CA concentration of 0.06 mM (2 g/l). In contrast, the high density of hydrophilic nanopores (4.0 x10^{11} nanopores per cm^2) in our membrane, if filled with CA, would allow attainment of a significantly higher local CA concentration. To prove this point we performed FTIR spectroscopy of the CA filled membrane prepared on an IR transparent silicon substrate in the same manner as for the QCM measurements (**Figure 3.1.6c**). Based on the molar extinction coefficient of the Amide I absorption band at 1640 cm^{-1} attributed uniquely to the CA enzyme, we calculated a molar concentration of CA that corresponded to a loading of on average of 2 CA enzymes per nanopore yielding an effective CA concentration within the membrane of 3.7 mM (100 mg/mL), or, an effective areal density of 8.0 x10^{11} CA/cm^2. This CA concentration is 10x greater than achievable in solution (~ 10 mg/mL) and correspondingly accelerates the rates of selective CO_2 dissolution and release from the membrane.

Knowing the CA areal density and the membrane thickness we can attempt to calculate the CO_2 permeance. As mentioned above, the CO_2 permeance of the enzymatic water membrane is determined by the relative rates of: 1) CO_2 entering the membrane on the feed side; 2) HCO_3^- species transport through the thickness of the membrane; and 3) CO_2 release from the 'downstream' side, where the slowest 'rate limiting' process governs the overall CO_2 permeance. Based on the reversible Eq.1, CA catalyzes the dissolution of CO_2 on the feed side to form bicarbonate that dissociates to carbonic acid that diffuses through the water layer and is enzymatically converted back to CO_2 on the downstream side, meaning Steps 1 and 3 depend upon the enzymatic activity of CA, while Step 2 depends on the diffusion coefficient of carbonic acid or other carbonate species in water. For Step 2, we know the CO_2 permeability in pure water is 210×10^{-9} $cm^3(STP)\cdot cm$ /sec$\cdot cm^2\cdot cmHg$[12]; therefore, the permeance for a 20nm thick water layer should be $210\times10^{-9}cm^3(STP)cm$ /sec$\cdot cm^2\cdot cmHg$ divided by the thickness of 20nm, which is 0.1 cm^3/s-cm^2-cmHg, or 10^5 GPU, much larger than the permeance we observed (**Figure 3.1.6a**). This indicates that the CA catalyzed Steps 1 or 3 are rate limiting. As discussed previously, we determined the areal CA enzyme density on our membrane to be 8×10^{11} molecules/cm^2. Taking the published activity of 10^6 reactions/sec for Bovine enzyme[57], the calculated CO_2 permeance will be 8×10^{17} molecules/sec$\cdot cm^2$, or, a volumetric flux of 0.03 cm^3/sec$\cdot cm^2$. At the 36cmHg driving pressure (see Methods), this corresponds to a CO_2 permeance of 833 GPU, which is in reasonable agreement with the measured data (ranging from 500-2600 GPU, **Figure 3.1.6a**).

Molecular dynamics simulations of nanoconfined CA enzymes

We reasoned that the variability in the measured permeance and the discrepancy between the calculated 'theoretical' value and the highest measured CO_2 permeance could be a consequence of nanoconfinement effects on the CA structure and activity. To test this idea, we performed molecular dynamics simulations of the CA enzyme in conditions that resemble the silica membrane to characterize atomic level details of the system. As shown in **Figure 3.1.7**, we simulated 1 or more CA enzymes in a rectangular silica nanopore (inner dimensions of 8 x 8 x 10 nm) that is filled with water at pH 7 (average silanol density of 5.9 SiOH/nm^2 with 16.5% ionization, see Methods). The simulations revealed that, initially placed in the center of the nanopore, the CA enzymes rapidly
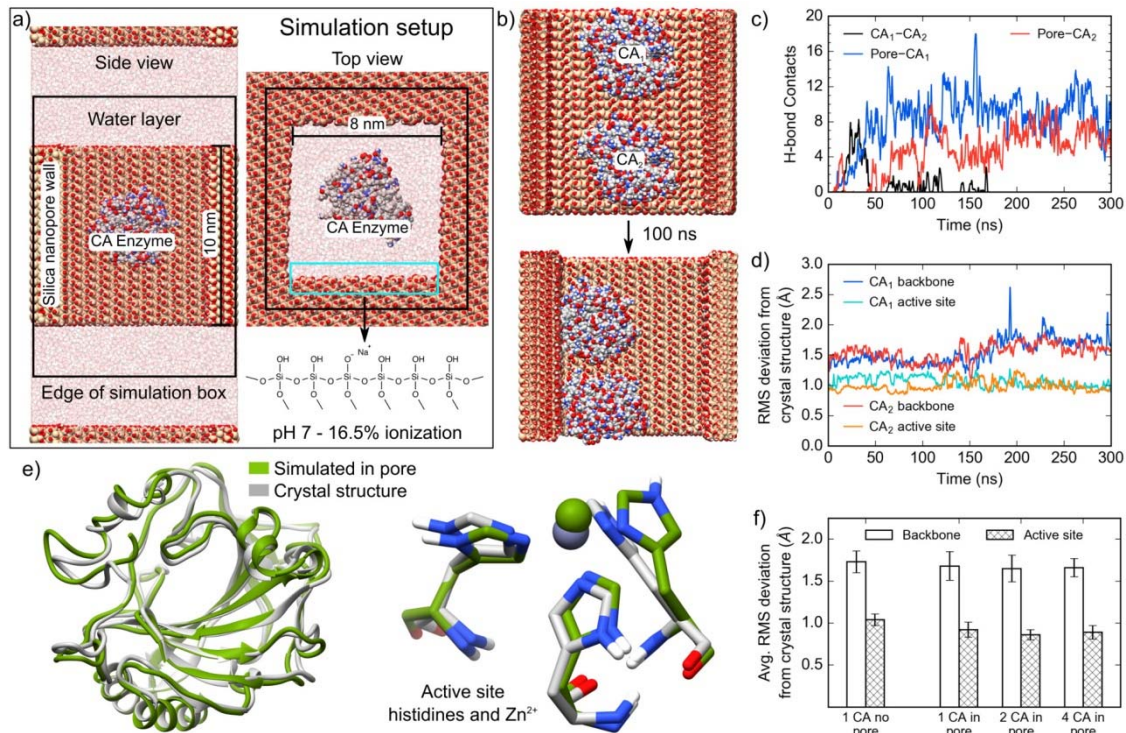
Figure 3.1.7. a) Setup for the molecular dynamics simulations of CA enzymes in a silica nanopore; b) CA enzymes rapidly (< 100 ns) adsorb to the surface of the silica nanopore and remain in contact with the pore walls for the duration of the simulation, as shown by H-bond contacts between the pore and CA in (c); d) root-mean-squared deviation (RMSD) data of the protein backbone and active site atoms shows that the structure of the CA enzymes adsorbed to the pore remains stable during the course of the simulation and close to the crystal structure; e) ribbon representation (left) and close-up of the active site of the CA enzyme show close similarity between the average structure simulated in the nanopore and crystal structure; f) average RMSD data (over the last 50 ns of 300 ns simulations) for 1, 2, and 4 CA enzymes per pore (to simulate varying crowded conditions) shows that structure of the enzyme is highly robust and resembles the CA structure free in solution.

(< 100 ns) 'find' the walls of the pore (**Figure 3.1.7b**) and form hydrogen bonds that are sustained throughout the simulation (**Figure 3.1.7c**). Adsorption to the walls of the nanopore is expected due to the large number of polar and charged (positive and negative) residues on the surface of CA, and is consistent with previous studies showing binding of polypeptides to different silica surfaces[68, 69]. However, adsorbed CA enzymes retain some mobility and are able move along the silica surface. Different portions of the enzyme contact the pore walls at different times with the active site remaining accessible to the solution and permitting substrate and product molecules to readily diffuse in and out. The structure of the CA enzyme in the nanopore is highly robust, as shown by the root-mean-squared deviation (RMSD) of the backbone and active site atoms compared to the CA crystal structure (**Figure 3.1.7d and e**), and does not appear to be negatively affected by adsorption to the nanopore. Furthermore, the CA RMSD data for simulations in the nanopore closely resemble the values obtained for the free enzyme in solution (**Figure 3.1.7f**), even for the case of crowded confinement (2-4 CA enzymes in the nanopore with an effective concentration greater than 150 mg/mL within individual nanopores). These results suggest that enzymatic activity of CA in the silica nanopores will be largely unaffected by adsorption and/or crowding.

Discussion and summary

Separation processes in natural biological systems typically take place in a watery environment, oftentimes aided by enzyme catalysis, and the thickness of biological membranes is

normally on the nanometer scale. To implement the same strategies for CO_2 capture, we have fabricated an ultra-thin, enzymatic, nano-stabilized water membrane. By using Nature's design principles of "ultra-thin", "watery" and "enzymatic" we achieved a combination CO_2 flux and CO_2/N_2 selectivity greatly exceeding that of conventional membranes. The membrane is mechanically and environmentally stable due to the capillary force of water condensation within uniform hydrophilic 8-nm nanopores. Using a regular array of close packed hydrophilic nanopores whose depth is only 18-nm to confine and contain CA enzymes, we achieved an effective CA concentration 10x greater than possible in water. Our simulations show that favorable interactions between CA and the silica nanopores result in adsorption of the enzymes to the pore walls and allows very high local protein concentrations (2 or more CA per pore, equivalent to >150 mg/mL) compared to the bulk aqueous solution (~ 10 mg/mL). This computational result is in good agreement with measurements based on amide signals in the FTIR spectrum that indicate ~2 carbonic enzymes occupy each pore. Locally high protein concentration and molecular crowding in the nanopores will likely increase the enzyme's specific activity, as observed for other confined enzymes[70, 71], and enhance the effective binding affinity (decreased Michaelis constant) due to excluded volume effects[72, 73][30,31]. Our catalytic water membrane exceeds for the first time the U.S. Department of Energy standards for CO_2 sequestration technologies and should be stable for CO_2 sequestration from flue gas. By simple replacement of CA enzymes with alternate enzymes we propose that our ultra-thin, enzymatic, nano-stabilized water membrane concept could be readily adapted to other separation processes.

Methods

Fabrication of ultra-thin enzymatic water membrane.

The membrane was fabricated on a commercial, asymmetric Anodisc[TM] porous alumina support purchased from Whatman International Ltd. The support is 60μm thick and is composed of oriented asymmetric vertical channels that are perpendicular to the disc surface. The channel diameters taper from 200-nm in diameter on the bottom surface to 50-nm in diameter on the top surface (see **Figure 3.1.3**). The support was treated with UV/ozone to fully hydroxylate the alumina surface and insure wetting and covalent bonding with 'sol-gel derived' silica (*vide infra*). In order to fabricate oriented 8-nm diameter cylindrical pores within the channels of the Anodisc[TM], we prepared a Pluronic P123 block copolymer containing silica sol following the procedure of [61, 62]. The sol was applied to the support by spin-coating at 3000RPM where capillary action followed by evaporation-induced self-assembly (EISA) resulted in the formation of a hexagonal silica/P123 mesophase oriented within the Anodisc[TM] pore channel[61, 62]. After two successive spin-coating depositions, the samples were aged at 50 °C for 12 hours. To remove the P123 pore template, the samples were calcined at 400l><full-title>Small</full-title></periodical><pages>982-989</pages><volume>4</volume><number>7</number><dates><year>2008sub-micron pores of the Anodics[TM] as shown in **Figure 3.1.3**.

To enable the formation of an ultra-thin stabilized water membrane, we first exposed the Anodisc[TM] to ozone irradiation to maximize the coverage of hydroxyl groups on all the nanopore surfaces. This was followed by five cycles of alternating HMDS+TMCS/H_2O vapor exposure at 180 °C in an Angstrom-dep[TM] atomic layer deposition (ALD) system to convert the hydrophilic surface hydroxyl groups to hydrophobic trimethylsilyl groups. Following that, the hydrophobic porous support was placed into the plasma chamber of an Angstrom-dep[TM] *III* plasma-ALD system, and the top surface was irradiated by an oxygen plasma for 5 seconds, converting only am 18-nm deep thickness of the hydrophobic nanopores to hydrophilic hydroxyl terminated silica nanopores. To load CA enzymes into the nanopore channels, the membrane was 'floated' hydrophilic face down on a 0.05 mM CA solution and bath sonicated gently for 10 minutes. Then the samples were

removed from the solution, inverted, and maintained in a horizontal configuration on a clean surface until all excess water on the membrane evaporated.

Structural and Physical Characterization

FIB and SEM were carried out on a FEI Q3D dual beam FIB/SEM system, with 30kV/3nA initial voltage/current followed by 8kV/25pA final polishing voltage/current for ion beam mode, and 5kV/24pA for SEM mode. TEM images were acquired using a JEOL2010F HRTEM, and Ti-mapping was acquired using the same TEM with a Gatan EELS system.

GISAXS was performed using a Bruker Nanostar on samples prepared on Anodisc™ substrates fabricated as indicated above or on Si substrates prepared as described for FTIR analysis (*vide infra*).

QCM was performed using a QCM200-5MHz quartz crystal microbalance manufactured by Stanford Research Systems. An air-tight environmental chamber was used during the measurement for controlled humidity.

FTIR was performed using a Thermo Scientific Nicolet 6700 FTIR spectrometer. A P123-templated silica film was deposited onto intrinsic, IR transparent single crystal Si substrates (400 µM thick, double polished) by spin-coating; this film was then processed in an identical manner as the Anodisc™ supported P123 templated film described above and loaded with CA.

CO_2 separation performance measurement

CO_2 permeance and CO_2/N_2 or CO_2/H_2 selectivity measurements were performed using a home-made test cell designed to accommodate a 25mm diameter sample and to be immerged into a water bath for needed temperature control. The feed gas was first introduced through a water bubbler heated at 90 °C to achieve a saturated humidity. In the permeance vs temperature and pH measurements (**Figure 3.4.6a-b**), the feed gas was compressed pure CO_2 with a relative pressure of 7.0 psi (or 36cmHg). On the collection side, a bubble flow rate meter was used to measure the flow rate, and the CO_2 pressure was maintained at ambient atmospheric pressure. For the permeance measurements for comparisons with other CO_2 membranes (**Figure 3.4.6f**), the feed gas composition was 20vol% CO_2 in N_2 maintained at ambient pressure in order to simulate the major composition of flue gas from a coal-fired plant. On the collection side, a $Ca(OH)_2$ solution was used to collect CO_2 and maintain a constant driving pressure for CO_2 separation. The amount of permeated CO_2 could also be determined by $Ca(OH)_2$ weight increase.

Molecular dynamics simulations were performed with the GROMACS software package[71]. The CHARMM36 force field[74, 75] was used to model the bovine carbonic anhydrase (CA) enzyme (Protein Data Bank accession number 1V9E[76]) under different conditions relevant to CO_2 separation, including interaction with silica nanopores. The silica nanopore atoms were modeled with the CHARMM36-compatible INTERFACE force field[77, 78]. Protonation states of amino acids of the CA enzyme were selected according to the results of PROPKA analysis at pH 7[79].

A rectangular silica nanopore was built based on the structure of the alpha-cristobalite unit cell. The pore's outer dimensions are 11 x 12 x 10 nm and its internal dimensions are 8 x 8 x 10 nm. The average surface silanol density of the pore is 5.9 SiOH/nm2, which provides a reasonable model of the amorphous silica surface used in the experimental membranes[80, 810]. A percentage (16.5 %) of the surface silanols were ionized to match the pH 7 conditions. Sodium (Na+) ions were added to counter the negative charge of the ionized silanol groups. No additional salt molecules, either Na+ or Cl-, were added to the simulation except to produce an overall neutral charge simulation system. A vertical water-filled space exists between periodic images of the simulation cell of height 6 nm, giving the CA enzyme the ability to exit the nanopore. Three CA-

nanopore systems were simulated with 1, 2, and 4 enzymes within the pore to observe possible crowding effects. A free CA enzyme in solution was also simulated for reference.

All systems were simulated at room temperature (298 K) for 300 ns using a Nose-Hoover thermostat. The simulation volume for pore systems was adjusted during the early stages of the simulation to obtain an average pressure of 1 atm, and subsequently simulated at constant volume. The free CA enzyme was simulated at constant 1 atm pressure using a Parrinello-Rahman barostat.

3.2 Establishing fundamental structure / catalytic function relationships for 2D metal chalcogenide materials

Overview - Establishing processing–structure–property relationships for monolayer materials is crucial for a range of applications spanning optics, catalysis, electronics and energy. Presently, for molybdenum disulfide, a promising catalyst for artificial photosynthesis, considerable debate surrounds the structure/property relationships of its various allotropes. Here we unambiguously solve the structure of molybdenum disulfide monolayers using high-resolution transmission electron microscopy supported by density functional theory and show lithium intercalation to direct a preferential transformation of the basal plane from 2H (trigonal prismatic) to 1Tt (clustered Mo). These changes alter the energetics of molybdenum disulfide interactions with hydrogen ((G_H), and, with respect to catalysis, the 1T transformation renders the normally inert basal plane amenable towards hydrogen adsorption and hydrogen evolution. Indeed, we show basal plane activation of 1Tr molybdenum disulfide and a lowering of ΔG_H from +1.6 eV for 2H to +0.18 eV for 1Tro comparable to 2H molybdenum disulfide edges on Au(111), one of the most active hydrogen evolution catalysts known.

Improving the capacity and efficiency of the Hydrogen Evolution Reaction (HER) is an enduring challenge of green energy production and artificial photosynthesis[82, 83]. Still, while HER in organisms evolved with time and increasing complexity, artificial HER aims to replicate the same with minimalism and simplicity. A cornerstone of the challenge is to mimic the function of natural hydrogenase enzymes, which catalyse HER in living systems. Indeed, it can be seen that without a catalyst like hydrogenase, HER does not proceed with the speed required for practical applications[84, 85]. However, hydrogenases can be difficult to extract and purify, and can denature under non-natural operations[86], consequently, inorganic alternatives are used for most applications. The most common example of this is platinum (Pt), which has served as the benchmark catalyst for HER due to its high catalytic efficiency[87-89]. Nevertheless, because of the scarcity and cost of Pt, a more abundant alternative is needed for cost-effective implementation.

For this, MoS_2, an earth abundant lamellar solid, has shown prominent HER catalysis nearing the efficiency of platinum[90, 91]. However, experiments using MoS_2 grown on Au(111) indicated that this material is only catalytic on its edge sites[90]. Theoretical studies corroborated these results with the Gibbs free energy of hydrogen adsorption (ΔG_H), a measure of HER efficiency, to be feasible for catalysis only at MoS_2 edges[92, 93]; the basal plane of MoS_2 does not appear to participate in catalysis, meaning the bulk of material is catalytically inert. Consequently, the maximization of MoS_2 edges and mimicry of the edge structure has become a significant topic[94-97].

Interestingly, recent studies have begun to show enhancement of MoS_2 catalytic efficiency following lithium intercalation and exfoliation. The Tafel-slope of these sheets, a benchmark of electrochemical efficiency against applied overpotential, is nearly twice that of natural MoS_2 after lithium treatment[98-100]. As the lithium-exfoliation reactions increase the availability of basal plane surfaces but not edges, the catalytic improvements are postulated to be basal plane related. Nonetheless, because the basal plane structures of lithium-exfoliated monolayers, and indeed, many

two-dimensional sheets, are difficult to characterize[101-103], the post lithiation and exfoliation structure of MoS_2 remains nebulous and historically controversial, rendering the origin of this catalytic enhancement correlatively vague. To briefly recount a history of the structural understanding of MoS_2 exfoliated with the assistance of lithium, it can be seen that a structural change in Li-intercalated MoS_2 has been reported as far back as 1973[104], nevertheless, interpretations of the final structure vary significantly in the literature. For example, in 1973, Somoano et al.[104], observed extensive layer displacements after intercalation, suggesting the resulting product is a mixture of disordered compounds. However, in 1983, Py et al.[105] reported the alkali metal exfoliated structure to be crystalline, with a first order phase transition from the natural trigonal prismatic (2H) to an octahedral (1T) phase. In 1989, a significant distortion to a $2a_o \times 2a_o$ lattice was reported by Chrissafis et al.[106] In 1991, an octahedral structure was observed by Jimenez et al. and Qin et al., but a small distortion was noted, making the final crystal a $2a_o \times a_o$ super lattice[107, 108]. Atomic force microscopy images obtained in 1993, by Schumacher et al., though, indicated no distortion or superlattice[109]. In 1998, Dungey et al. observed a $2a_o \times 2a_o$ lattice with trigonal Mo clustering[110], but in 1999, a $2a_o \times a_o$ superlattice was seen by Heising et al., with severe distortion and formation of infinite Mo-zig-zag chains[111]. A chain-of-diamonds motif was suggested by Petkov et al. in 2002 ([112]), but most recently, in 2013, Maitra et al. reported a distortion-free octahedral phase[113]. Chhowalla and coworkers observed similar variations, from a perfect octahedral phase with natural 2H MoS_2 domains[114], distorted phases[100], coexistence of various phases[115], and also, a perfect octahedral phase[116]. Surprisingly, we note that the changed structures are almost always referred to as 1T, regardless of polymorphic structural differences. It is therefore not surprising to see recent catalytic improvement being attributed to varied structures, including octahedral[98, 99, 113], and distorted Mo phases[117, 118]. Part of the confusion is likely a simple consequence of incomplete transformation resulting in identification of partially transformed and transitional states due to variations between batches, however, there may be underlying issues of stability as well, making the resultant structure, and indeed, structural based predictions of its catalytic effectiveness difficult to handle[119].

To address these long-standing issues and shed light on the catalytic origin of the transformed crystals, here we take a combined experimental/theoretical approach using controlled processing conditions to achieve stable phases and density functional theory calculations to investigate the stability of these polymorphs. With the solution processing advantages of these materials[120-122], we report the catalytic efficiency of HER in homogenous reactions, with experimental H_2 yield of these phases, and corroborate them with calculated ΔG_H. The analysis was then extended from MoS_2 to WS_2 to show similarly distorted crystal phases and basal plane catalytic activation.

Results

Exfoliation and phase transformation of MoS_2

A typical lithium-exfoliation reaction consisted of immersing MoS_2 powder in n-butyl lithium (1 M) for 72 h at room temperature[112, 114, 123]. The intercalated compound was then transferred to water and sonicated to yield exfoliated monolayers. After purification using centrifugation and dialysis, concentrations and purity of each batch were measured using Flame Atomic Absorption Spectrophotometry. Samples were then visualized using abberation-corrected scanning transmission electron microscopy.

As seen in **Figure 3.2.1**, a typical sheet exfoliated using this method indeed yields a mixed phase. First, a trigonal prismatic (2H) phase that corresponds with an untransformed basal plane can be seen with symmetrical Mo–Mo spacing of 2.98±0.05 Å. Second, an octahedral phase with displaced sulfur atoms and symmetrical Mo

arrangements (2.95±0.06 Å) is seen, albeit in small quantities. Last, large swatches of a visually distinct, tertiary phase is also present, with Mo atoms asymmetrically clustered to form one-dimensional lines of alternating light-and dark stripes. In this phase, Mo–Mo distances of 3.55±0.16 Å and 2.92±0.16 Å were measured. On the basis of the above, we thus conclude that within one individual sheet, a microcosm of various phases are present,
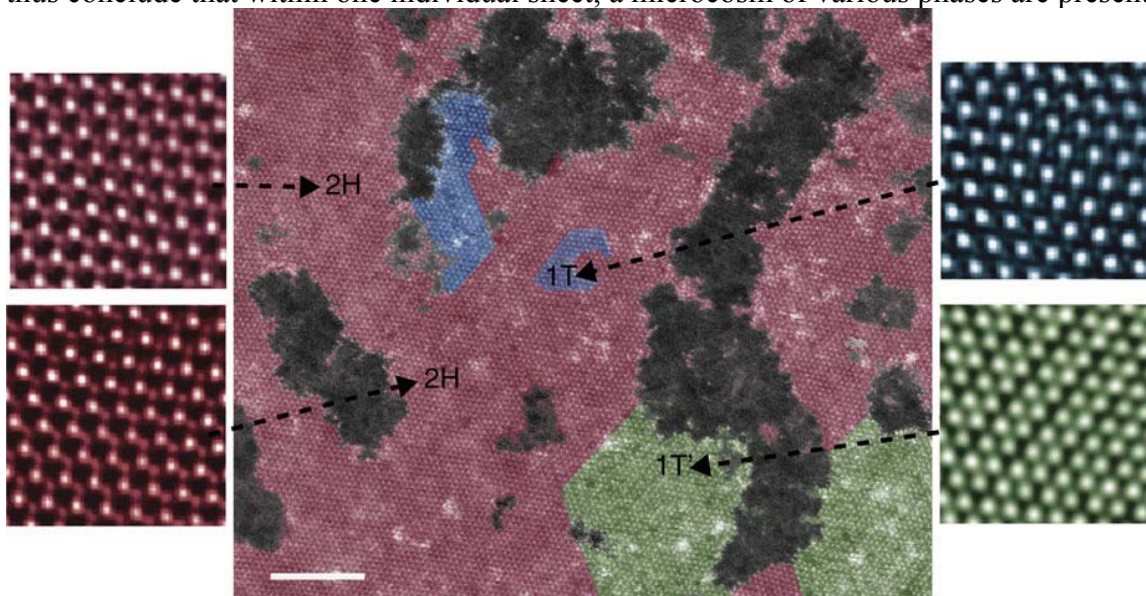
Figure 3.2.1 Polymorphism and incomplete transformations. Polymorphisms within the basal plane exhibit coexistence of three different phases, 2H (trigonal prismatic, false coloured as red), 1T (octahedral, false coloured as blue) and 1T′ (clustered Mo, false coloured as green). Scale bar, 5 nm.

with each representing differing interpretations in previous work. Nevertheless, as the stability of each phase should be an intrinsic consequence of the energetics of distinct atomic arrangements, we sought to understand the relative stabilities of each phase. Because it was previously reported that materials revert back to the natural 2H phase[123], we reasoned that the 2H is the overall energetic minimum, with the other polymorphs occupying differing metastable points in relation to the 2H.

To better define this, we employed Density Functional Theory (DFT) to independently predict the structures of possible polymorphs (data not shown). As can be seen in **Table 1**, a total of four polymorphs were predicted based on structural optimization of unit cells. The first two, consisting of 1×1 unit cells, were the 2H trigonal prismatic phase and the 1T octahedral phase. In addition, a distorted phase with zig-zag chains consisting of a 2×1 supercell and a phase with Mo–Mo atoms clustered into trimerized pockets in a 2×2 supercell were predicted. We dub the two later phases, 1T′ and 1T″, respectively.

Next, the stabilities of each DFT polymorph were calculated. It can be seen that the symmetrical 1T representation has the least stable ground-state (+0.82 eV versus 2H). Indeed, in a 2×2 or 4×4 supercell, we find the 1T phase eventually relaxes into 1T″, which is second in stability, at +0.63 eV, conforming with the dynamical phonon instability

Table 1 | Structural polymorphs of MoS₂ and summary of parameters as predicted by Density Functional Theory.

2H	1T	1T′	1T″

Phase	Relative stability (eV f.u.$^{-1}$)	a (Å)	b (Å)	α (°)	Mo-Mo (Å)	E_g (eV)
2H	0	3.18	3.18	120	3.18	1.7
1T	0.82	3.17	3.17	120	3.17	Metallic
1T′	0.55	6.55	3.18	119	2.77, 3.18	0.01 (PBE) 0.26 (HSE06)
1T″	0.63	6.44		119.5	2.77, 3.26	0.1 (PBE) 0.01 (HSE06)

(Top) Mo atoms are represented as teal spheres, S atoms as gold spheres. (Bottom) From left to right, relative stability in eV, lattice parameters a, b and α, Mo-Mo distance, and band gap E_g (eV) based on Perdew–Burke–Ernzerhof (PBE) and Heyd-Scuseria-Ernzerhof (HSE) exchange-correlation functionals.
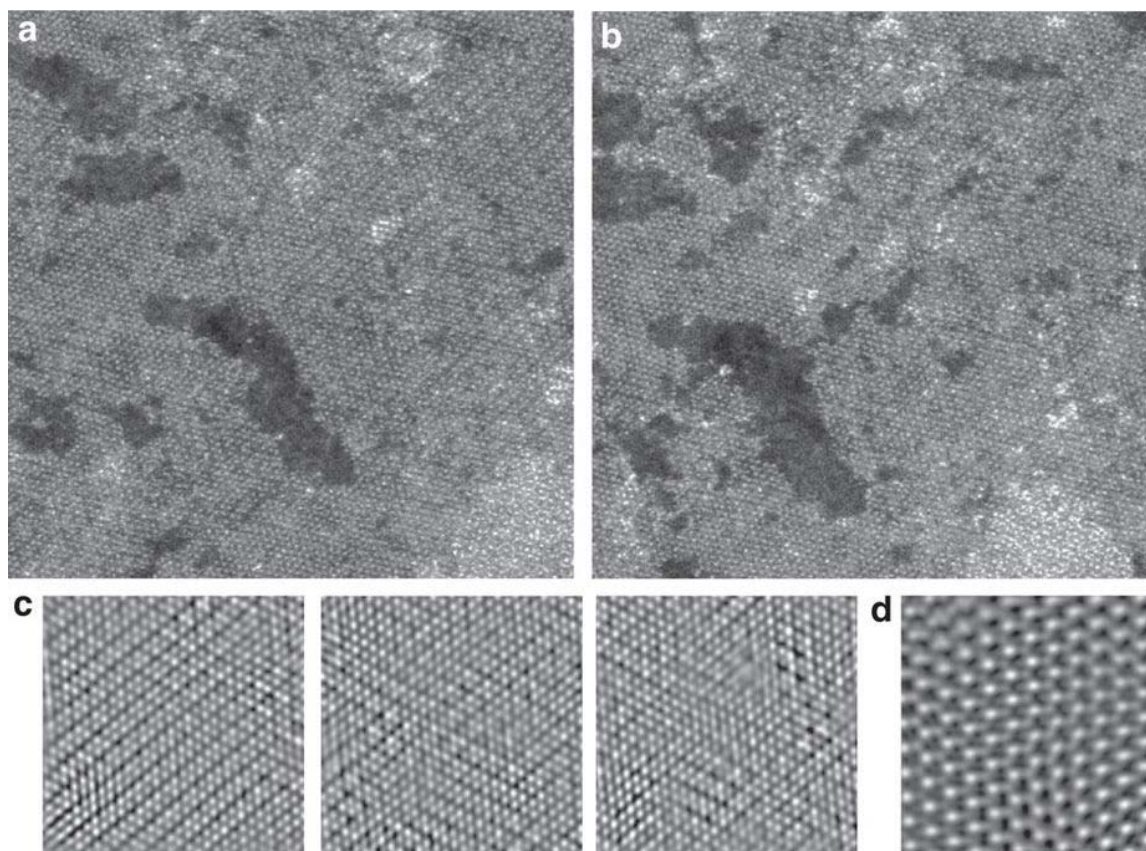
Figure 3.2.2 Basal plane transformations. (a) MoS₂ basal plane showing preferential transformation to 1T′ with increased lithiation, in accordance with the calculated relative stability of the metastable phases. **(b)** On electron beam illumination, the basal plane exhibits a restoration to a symmetrical Mo arrangement indicative of 2H reversion. **(c)** Sequential frames taken 60 s apart, showing phase evolution under the electron beam. Electron dose rate was 2,800 e Å^{-2} s^{-1}, with each frame requiring 40 s to capture. **(d)** An electron dosed region with sulfur atoms resolved, demonstrating 1T′ to 2H phase reversion after illumination.

previously predicted in the 1T phase[119]. Nevertheless, the 1T′ phase was significantly more stable than 1T and 1T″ (+0.55 eV versus 2H), with a barrier against 2H reversion of 0.73 eV f.u.$^{-1}$ (formula unit, data not shown). By the DFT calculations, the transformed

portions within a sample, if allowed to reach metaequilibria, should therefore preferentially form 1T′ instead of the other polymorphs.

To investigate these results experimentally, we prepared samples to induce equilibria by extending the lithium intercalation period. As seen in Figure **3.2.2**, a preferential transformation to 1T′ is possible on the entirety of the basal plane. This therefore suggests that the various polymorphs observed previously are likely consequences of incomplete reactions, such as partial intercalation, with parts of the basal plane yet to undergo sufficient conversion to the 1T′. Indeed, we have observed that when intercalation times are extended from 72 to 240 h, a complete transformation to the 1T′ can be achieved (data not shown).

Given the DFT prediction of 1T′ as a metastable phase, we examined the ability to covert 1T′ back to 2H under electron beam-illumination. As shown in **Figure 3.2.2c**, sequential frames taken at 60 s intervals (acquired at 40 s/frame at an electron dose rate of 2,800 electron $\text{Å}^{-2}\,\text{s}^{-1}$) show gradual relaxation of Mo atoms from 1T′ lines to symmetrical 2H spacing. A detailed investigation of the structures again showed the 1T′ phase with Mo spacings of 3.55 Å and 2.92 Å, and the relaxed structure displayed trigonal prismatically coordinated sulfur atoms with Mo–Mo spacing of 2.95 Å, in agreement with the 2H structure (**Figure 3.2.2d**). These results corroborate the 1T′ as the energetically preferred metastable phase that will relax back to 2H when energetic input, for example, heat, exceeds that of the metastable barrier energy. It further suggests that the partial or incomplete phase transformations observed previously may be due to energetic conditions reverting the material to 2H during the characterization process. These observations support previous electrical characterizations of the material[114, 123] with 1T′ having greatly reduced resistivity compared to 2H (calculated bandgap of 0.01 and 1.7 eV, respectively, shown in **Table 3.2.1**).

To corroborate the above, High-angle annular Dark-field (HAADF) images were simulated using coordinates from DFT. As seen in **Figure 3.2.3**, good agreement was seen between experiment and simulations. We note in samples that are predominantly 1T′ (**Figure 3.2.2a**), lines modulated in two-dimensions can be seen at intersections of 1T′. This may be interpreted as the 1T″, however, its occurrence is very localized and defective (<5%), and consequently, not of practical significance.

Dye-sensitized HER

Following these structural insights, HER catalysis of these MoS_2 polymorphs was examined. For this, we measured H_2 formation using MoS_2 in a homogenous photocatalysis reaction. In a typical reaction, a solution of MoS_2 was sensitized with Eosin Y (EY), and Triethanolamine (TEOA) was added as a sacrificial electron donor[43,44]. The reaction mixture was then purged of atmospheric gasses, and irradiated with a xenon lamp tuned to 1 sun. The flow entering and exiting the reaction flask was then monitored on a gas chromatograph to quantify H_2 formation inside the flask.

The reaction proceeded via photoexcitation of EY and subsequent intersystem crossing to yield a triplet excited state (EY^{3*}). Acceptance of an electron via reductive quenching from the sacrificial electron donation (TEOA) then yields a radical EY^{-}[113, 124-127]. The highly reductive EY^{-} can then reduce a proton to form H_0, return the electron to an oxidized TEOA, or transfer the
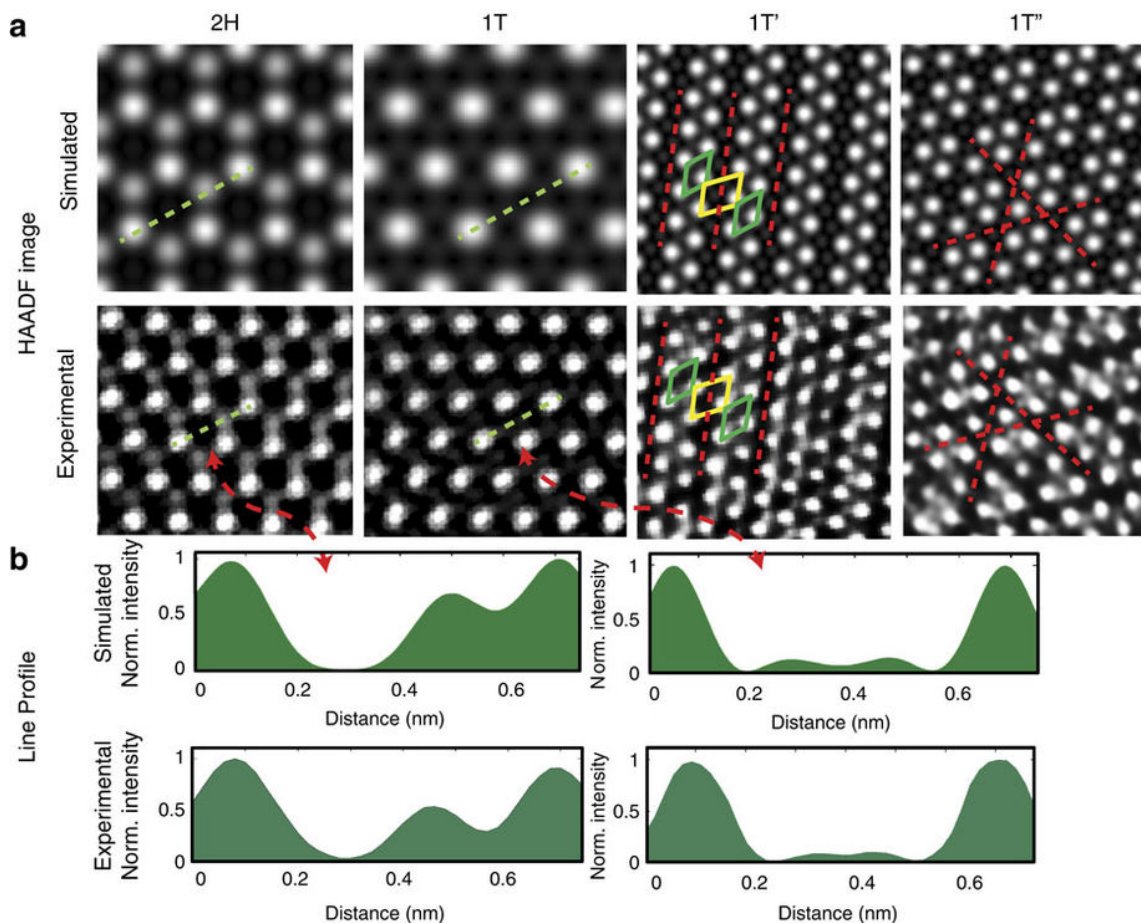

Figure 3.2.3 Different possible phases for MoS$_2$ (a) Simulated and experimental images of different possible phases for MoS$_2$. FFT mask filters have been employed for clarity. **(b)** line scan comparisons between 2H and 1T using the simulated and experimental images, showing modulation of sulfur contrast.

electron to another catalyst such as the MoS_2. As seen in **Figure 3.2.4a**, in the absence of MoS_2, direct reduction of protons by radicalized EY occurs by collisional reductive quenching with TEOA (data not shown), and generates a peak H_2 flux of 150 nmol min^{-1}. Over the course of 100 min, a yield of 7.5 µmols was observed, giving a typical activity of 4.5 µmol h^{-1} (**Figure 3.2.4b**). Sequential addition of 1T′ (for example, 'fully transformed MoS_2') gradually raised the peak flux, until saturation was reached with 40 p.p.m. of MoS_2, yielding a peak flux of 620 nmol min^{-1}. With the latter reaction, 40 p.p.m. of MoS_2 raised overall yield to 30 µmol in the first 100 min, giving a typical activity of 18 µmol h^{-1}, which is four times higher than the autocatalytic EY dye under the same conditions[124]. In both cases, addition of small amounts of HCl regenerates a stopped reaction, suggesting reaction termination is due to proton depletion (data not shown).

Given the boosted HER performance, it reasons that in the presence of fully transformed MoS_2 a preferential charge transfer occurred between the radical EY^{-} and the MoS_2. Indeed, with the reductive potential of EY at −0.8 V versus normal hydrogen electrode (NHE), and MoS_2's conduction band situated at 0.2 V versus NHE, such a transfer is feasible[128, 129]. To support this, the charge transfer was examined using fluorescence quenching correlations between EY and the Li-exfoliated MoS_2 (**Figure 3.2.4c**). It can be seen that the fluorescence quenching interactions

between EY and MoS$_2$ are predictive of the eventual H$_2$ yield, with both curves rising to saturation in the presence of 40 p.p.m. of MoS$_2$. The fluorescence quenching following a saturation reaction fitting, vis-à-vis a continual diminishing of fluorescence with increasing quencher concentration (for example, collisional quenching) indicates the formation of a ground-state complex between EY and lithium-exfoliated MoS$_2$, facilitating effectual charge transfer. To further elucidate these interactions, we monitored the excited state interactions via fluorescence decay. As seen in **Figure 3.2.4d**, the fluorescence lifetime of a singlet excited EY, in the absence of secondary interactions, is ~1 ns. However, interactions with reductive quenchers, such as TEOA, via collisional quenching results in fluorescence lifetime shortening that fits a two exponential decay (**Figure 4.2.4e**)[130]. Interactions between EY and MoS$_2$ did not follow this behavior. Instead, the lifetime of EY was maintained at ~ 1 ns (**Figure 3.2.4f**), while the fluorescence intensity was attenuated by 75% at saturation. This indicates adsorption of EY onto MoS$_2$ to form a non-fluorescent ground-state complex that facilitates charge transfer within the complex with an excited state lifetime following the behavior of the 25% minority free dyes[130].
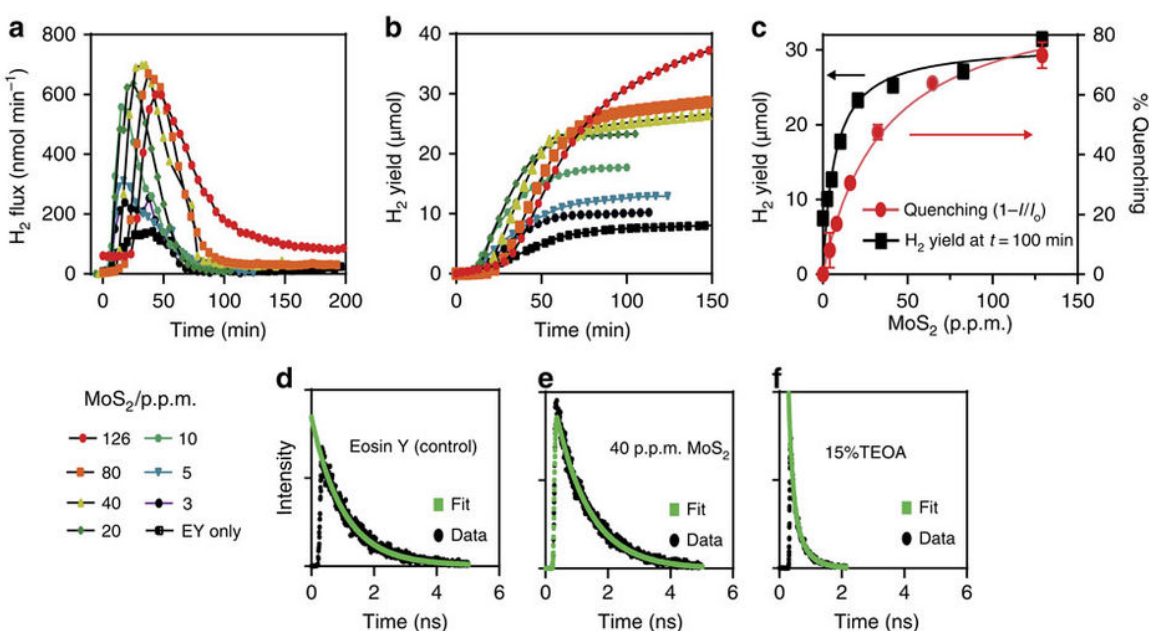
Figure 3.2.4 Hydrogen evolution. With dye sensitization (eosin Y, EY), MoS2 can be used to conduct homogenous hydrogen evolution reactions in solution. **(a)** Real time H2 flux at incremental MoS2 concentrations. Diminished reactions are indicative of proton exhaustion, and can be restarted with acid addition. **(b)** Corresponding cumulative H2 yield (For a and b note key bottom left). **(c)** Incremental concentration of MoS2 and correlative overlay of cumulative H2 yield (black) with fluorescence quenching of dye (red) in solution. **(d)** fluorescence decay of eosin Y, **(e)** reaction saturated with eosin Y and MoS2 showing similar decay, indicative of static-quenching and ground-state complex, and **(f)** collisional quenching between TEOA and eosin Y resulting in second order decay and attenuated lifetime. Error bars denote s.d.

As the above were performed with the fully transformed 1T′, effect of partial 1T′ transformation was then investigated. Here, two additional MoS$_2$ batches with diminishing 1T′ transformation were used in identical reactions. As shown in **Figure 3.2.5a**, the MoS$_2$ batches with diminished 1T′ transformation yielded significantly less H$_2$. Indeed, it can be seen that H$_2$ yield scaled proportionately with 1T′ signatures, which dominates the basal plane of the exfoliated sheets (data not shown). Given that 1T′ has shown empirical evidence of improved electrical conductivity, it is therefore possible that the improved catalysis seen with the 'fully transformed MoS$_2$' is a consequence of better electron conduction from the EY$^-$ charge transfer site to the catalytic sites of

MoS$_2$. However, it is also possible that the 1T′ transformation fundamentally alters the catalytic mechanism of the MoS$_2$ sheets, possibly giving additional active sites for catalysis.

To investigate these hypotheses, we calculated, via DFT, the free energy of hydrogen adsorption (ΔG_H), for the basal plane of each polymorph. From previous reports, it is known that $|\Delta G_H| \approx 0$ describes an optimal adsorption condition for catalysis[91]. Significant deviation in the exothermic direction ($\Delta G_H < 0$) can indicate irreversible adsorption, consequently, an efficient catalyst such as the 2H MoS$_2$ edge site, tends towards being slightly endothermic ($\Delta G_H > 0$). From our calculations, ΔG_H for the 2H basal plane is $> +1.6$ eV regardless of the H coverage and the absorption site. As a result, the adsorption of H on the 2H basal plane is strongly unfavorable. This is consistent with the 2H surface being catalytically inert[90]. However, when the basal plane is converted to 1T′, the hydrogen binding energy becomes negative (adsorption occurs). As seen in **Figure 3.2.5b**, the free energy of adsorption here for 1T′ MoS$_2$ is reasonably close to the optimum value of $\gtrsim 0$ eV [93], emerging at $\Delta G_H = 0.13$ eV at 1/16 coverage and growing to 0.25 eV as H coverage increased to 1/2. This indicates that the 1T′ transformed surface is amenable for catalysis, and indeed, the HER improvements with 1T′ fraction is due to catalytic activation of the MoS$_2$ basal plane. Most interestingly, we also observe adsorption of hydrogen to stabilize the 1T′. Indeed, **Figure 3.2.5c** shows that when H coverage exceeds 0.4, 1T′ becomes more stable than 2H. As significant benchmark work with 2H MoS$_2$ was performed with Au (111) supports[90], we compare 1T′ with 2H Mo-edge sites, when supported on gold. It can be seen here that $|\Delta G_H|$ on the 1T′ basal plane is comparable to the 2H Mo-edge supported on Au (111) and graphene at 0.25 coverage and slightly outperforms Mo-edges on Au (111) at 0.5 coverage (**Figure 3.2.5d, e**)[131]. Above all, the shear increase in surface area availability after exfoliation to monolayers (100–1,000-fold greater than bulk solids)[132] renders the basal plane improvements even more significant.

As WS$_2$ can undergo analogous phase transformations, its catalytic efficiency was similarly analyzed. We have also determined (data not shown), the H$_2$ flux with WS$_2$ was a third lower than MoS$_2$. For peak H$_2$ flux, WS$_2$'s 400 nmol min^{-1} showed approximately threefold improvement over controls, but weaker than the 750 nmol min^{-1} observed for MoS$_2$. Similarly, H$_2$ yield with WS$_2$ was 18 μmol at $t = 100$ min, which is 33% lower than MoS$_2$. As fluorescence lifetime measurements revealed an analogous molecular charge transfer pathway, the reduced HER efficiency was thus indicative of WS$_2$ being a less efficient catalyst. From **Figure 3.2.5**, it can be seen that the ΔG_H of 1T′ transformed WS$_2$ was 0.15 to 0.2 eV higher than MoS$_2$. Nevertheless, this value represents a 10-fold reduction over ΔG_H of 2H WS$_2$, indicating catalytic activation of the basal plane comparable to MoS$_2$.

Discussion

We investigated the structure of MoS$_2$ exfoliated with lithiation intercalation and directly correlated the varying physical structures to the catalytic origin for HER. Particularly, we demonstrated via abberation-corrected scanning transmission electron microscopy that modulated lithiation can lead to complete 1T′ transformation in the basal plane, and corroborated the experimental findings with DFT calculated phase stabilities. It was shown that the Mo atoms of MoS$_2$ became asymmetrically spaced with increased lithiation, thus forming the 1T′ phase. In DFT, the 1T′ was shown to be energetically favorable compared to other possible polymorphs. Nevertheless, external perturbations within the environment, including electron imaging parameters, can induce a reversion to 2H.
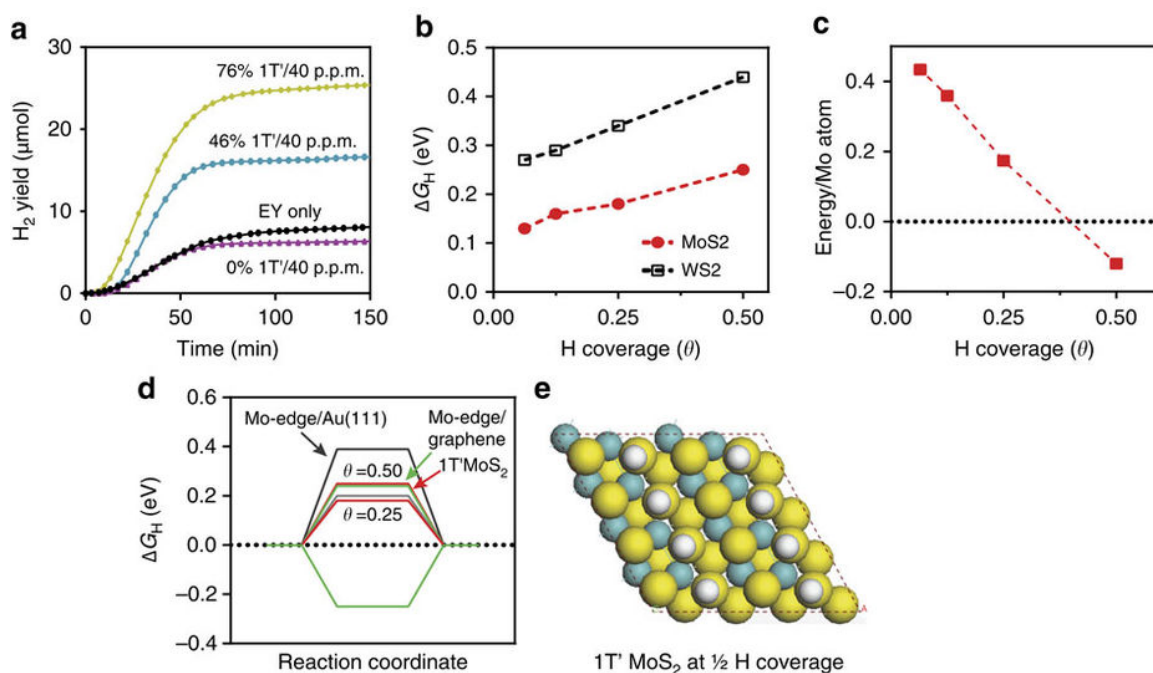
Figure 3.2.5 Energetics of Hydrogen Evolution. (**a**) Cumulative H_2 yield with MoS_2 undergoing differing degrees of 1T′ transformation. (**b**) DFT calculated Gibbs free energy of hydrogen adsorption (ΔG_H) as a function of H coverage. (**c**) DFT calculated stability of the MoS_2 structures per Mo atoms as a function of H coverage. As the H coverage exceeds 0.4, the stability of the 1T′ phase (red dashes) surpasses that of the 2H (black dots). (**d**) Free-energy diagram of hydrogen evolution reaction at 1/2 and 1/4 H coverage, with 1T′ MoS_2 basal plane, 2H MoS_2 edge on graphene and 2H MoS_2 on Au(111) as reference. (**e**) Structural representation of 1T′ at 1/2 H coverage.

With regard to catalysis, we have shown that the 1T′ transformation rendered the normally inert basal plane amenable towards hydrogen adsorption and H_2 evolution. Indeed, ΔG_H on the basal plane of 1T′ MoS_2 showed catalytic activation and was lowered from +1.6 eV in the 2H to +0.18 eV. Moreover, when H coverage became >0.4, DFT showed 1T′ phase stability surpasses that of 2H. To put this in perspective, the ΔG_H of 0.18 eV is comparable to 2H MoS_2 edges on Au(111), one of the most active HER catalysts yet characterized. This makes the 1T′ MoS_2 a state-of-the-art catalyst. In addition, as exfoliation to monolayers increases the surface area by as much as 1,000-fold[77, 133], the basal plane activation provides non-trivial increases in catalytic efficiency compared with the edge only catalysis of the 2H [90, 96]. We demonstrate this by H_2 evolution studies in basic solution (pH 11), via self-assembled photocatalytic charge transfer complexes for HER. Here it can be seen that MoS_2 catalysts can boost H_2 yield of the HER catalytic dye, EY, by fourfold. Moreover, MoS_2 itself does not fatigue over the course of the reaction. A clearer understanding of these materials, and the underlying relationship between structure, properties and performance, provides a pathway towards quantitative engineering of MX_2 to enable the emerging 'green energy' economy.

Methods

Lithium intercalation and exfoliation

For MoS_2, lithium intercalation was accomplished by immersing 1 g of MoS_2 powder in 10 ml of 1 M *n*-butyl lithium. The mixture was stirred vigorously in an inert atmosphere glovebox for 3 to 10 days. After, the compound was washed over three layers of Whatman filter paper (#51, ashless) with 200 ml of hexane and then collected in a bottle. Three hundred millilitres of H_2O was then added, and the mixture was sonicated for 3 m to extricate the intercalated MoS_2 powder from

the filter paper. The filter paper was then removed from the bottle, and the solution was sonicated for an additional 1.5 h. Unexfoliated portions were removed with centrifugation at 100 g for 3 min. The supernatant was then collected, and purified by centrifugation and washing with H_2O (3 × 10,000 g for 1.5 h, followed by resuspension in water after each centrifugation cycle). The solution was then transferred in to a dialysis bag (Fisher Scientific, MW 5,000), and dialysed against running water for 3 days. The solution was then again centrifuged at 500 g for 15 m to remove aggregates, and the resultant samples were used as is. For WS_2, Li intercalation was performed at 100 °C in a Parr bomb. Exfoliation and purification of WS_2 was the same as MoS_2. Atomic force microscopy images of exfoliates sheets are shown in (data not shown).

STEM microscopy and analysis

A FEI Titan G2 80–200 S/TEM with a Cs probe corrector operated at 200 kV was used in this study. High-angle annular dark-field (HAADF) S/TEM images were acquired with an electron probe size of 0.8 Å, convergence angle of 18.1 mrad, and current of ∼100 pA with an annular detector with a collection range of 60–160 mrad. The high resolution HAADF images were typically taken at 1,800 k magnification, yielding a pixel size of about 0.23 Å or a frame size of 48 × 48 nm for 2,048 × 2,048 pixels per frame. Such conditions gave rise to an equivalent electron dose rate of ∼2,800 electrons $Å^{-2} s^{-1}$. Acquisition of the HAADF image (frame of 2,048 × 2,048 pixels) took ∼40 s at a dwell time of ∼10 µs/pixel. In sub-figures of **Figures 3.2.1, 3.2.2** and **3.2.3**, the filtered images were obtained by Fast Fourier transformation (FFT) of the HAADF images into reciprocal space, forming FFT patterns. Reciprocal spots from the patterns (typically [88, 90, 134] type reflections) were selected, masked with a 60 pixels filter, and then transformed into real space with inverse FFT. Gatan Digital Micrograph was used for the image processing.

Computational details

All density functional calculations were carried out using the Vienna *ab initio* simulation package[135] with plane wave basis set and projector augmented-wave pseudopotentials[136]. All energies were calculated with Perdew–Burke–Ernzerhof exchange-correlation potentials[134]. For selected structures, we applied the hybrid HSE06 functional[137] to calculate the electronic band gap. The MoX_2 (X=Mo,W) monolayers were modeled using surface supercells separated in the periodic direction by a 20 Å-thick vacuum slab. We applied a plane wave energy cutoff of 600 eV and Γ-centered 24 × 24 × 1, 12 × 24 × 1, 12 × 12 × 1, and 6 × 6 × 1 k-points grids for Brillouin zone sampling of the 1 × 1 unit cell (2H and 1T), and the 2 × 1 (1T′), 2 × 2 (1T′′), and 4 × 4 (H/XS₂) supercells, respectively. The criteria of convergence for energy and force were set as 10^{-4} eV and $3 × 10^{-3}$ eV/Å. The hydrogen adsorption energies were calculated using the 4 × 4 surface supercell containing 16 Mo atoms and 32 S atoms. A dipole correction was applied to cancel the electrostatic interaction between the periodic slabs. The DFT binding energies were calculated as $\Delta E_H = \frac{1}{n}\left(E(\text{surf}+n\text{H}) - E(\text{surf}) - \frac{n}{2}E(\text{H}_2)\right)$, where E(surf+nH), E(surf), and E(H₂) are the total energies for the MoS_2 surface with n hydrogen atoms adsorbed, the clean MoS_2 surface, and the molecular hydrogen in the gas phase, respectively. The most stable H binding site in the basal plane of MoS_2 is on the top of the S atoms. We define H coverage as the ratio of the number of H and Mo atoms in the basal plane. For 1T′ MoS_2, we obtained binding energies of −0.16 eV, −0.13 eV, and −0.11 eV, and −0.035 eV at the 1/16H, 1/8H, 1/4H, and 1/2H coverage. For the 4 × 4 supercell, this corresponds to n=1, 2, 4, and 8, respectively. The adsorption free energy was calculated by adding a thermal correction to the binding energy $\Delta G_H = \Delta E_H + \Delta E_{ZPE} - T\Delta S_H$, where ΔE_{ZPE} and $T\Delta S_H$ are, respectively, the differences in the zero point energy and entropy contribution between the H adsorbed state and H₂ in the gas phase. We took $\Delta S_H = -\frac{1}{2} S(\text{H}_2)$, where ½ S(H₂) is the entropy of ½ H₂ in the gas phase at standard conditions (T=298.15 K, Pressure=1 atm). We used the assumption that the vibrational entropy in the adsorbed state is small[138]. For H/1T′ MoS_2, E_{ZPE}=0.228 eV (vibrational frequencies 2,530.1 cm^{-1}, 637.6 cm^{-1}, 519.8 cm^{-1}) and E_{ZPE}=0.271 eV

for H_2. With these values, the Gibbs free energy was calculated as $\Delta G_H = \Delta E_H + 0.29$ eV. Additional details are available in Supplementary Methods (data not shown).

Photocatalysis

Stock mixtures of 30% v/v TEOA and 10 mg ml^{-1} Eosin Y were freshly prepared for each reaction. MoS_2 (and WS_2) were prepared at twice the desired final concentration (for example, 80 p.p.m.). To prepare the reaction mixture, 35 ml of the 30% v/v TEOA was mixed with 35 ml of the MoS_2 or WS_2, reaching the final concentration of 15% v/v TEOA and the predetermined MoS_2/WS_2 concentration (for example, 40 p.p.m.). The mixture was then transferred to a 250 ml two-neck flask, to which 1 ml of the 10 mg ml^{-1} Eosin Y was added. The flask was then covered in aluminum foil, stirred and purged with continuous Ar flow (20 c.c.m.) for 20 min. After Ar purge, the aluminum foil covering was removed, and the mixture was illuminated at 1 sun. With the Ar flow kept at 20 c.c.m., gas samples were continuously monitored at 90 s intervals using an Inficon 3,000 micro GC gas analyzer until reaction termination.

Potential impact: As stressed in the Basic Energy Sciences Advisory Committee (BESAC) Report "New Science for a Secure and Sustainable Energy Future" (December 2008), solving our Nation's energy challenges will entail more than incremental changes in present materials-related technologies; new, advanced routes to nanostructured materials with transformational properties, such as our combination of evaporation-induced self-assembly and ALD deposition, will be required. Importantly, our approach to the synthesis of nanostructured catalysts and separation membranes will be both an ideal model platform for the fundamental understanding of nanoscale structure-property relationships and a scalable strategy for the large scale processing of advanced energy-related materials.

4.0 Publications, patents and awards that acknowledge DOE-BES support (2003-2017):

4.1 Refereed Journal Articles, Published 2003 to 2017:

1. Wang, H., Zhu, W., Ping, Y., Wang, C., Gao, N., Yin, X.; Gu, C., Ding, D., Brinker, C. J., & Li, G. (2017). Controlled Fabrication of Functional Capsules Based on the Synergistic Interaction between Polyphenols and MOFs under Weak Basic Condition. *Acs Applied Materials & Interfaces*, **9**(16), 14258.
2. Zheng, X., Shen, G., Wang, C., Li, Y., Dunphy, D., Hasan, T., & Brinker, C. J.; Su, B.-L. (2017). Bio-inspired Murray materials for mass transfer and activity. *Nature Communications* **8**.
3. Dunphy, D. R., Sheth, P. H., Garcia, F. L., & Brinker, C. J. (2015). Enlarged Pore Size in Mesoporous Silica Films Templated by Pluronic F127: Use of Poloxamer Mixtures and Increased Template/SiO2 Ratios in Materials Synthesized by Evaporation-Induced Self-Assembly. *Chemistry of Materials*, **27** (1), 75.
4. Chou, S. S., Huang, Y.-K., Kim, J., Kaehr, B., Foley, B. M., Lu, P., Dykstra, C., Hopkins, P. E., Brinker, C. J., Huang, J, & Dravis, V. P. (2015). Controlling the Metal to Semiconductor Transition of MoS2 and WS2 in Solution. *Journal of the American Chemical Society*, **137** (5), 1742.
5. Chou, S. S., Sai, N., Lu, P., Coker, E. N., Liu, S., Artyushkova, K., Luk, T. S., Kaehr, B., & Brinker, C. J. (2015). Understanding catalysis in a multiphasic two-dimensional transition metal dichalcogenide. *Nature Communications*, **6**.

6. Zhu, J., Quan, Z., Lin, Y.-S., Jiang, Y.-B., Wang, Z., Zhang, J., Jin, C., Zhao, Y., Liu, Z., Brinker, C. J., & Xu, H. (2014). Porous Ice Phases with VI and Distorted VII Structures Constrained in Nanoporous Silica. *Nano Letters*, **14** (11), 6554.

7. Fu, Y., Li, B., Jiang, Y.-B., Dunphy, D. R., Tsai, A., Tam, S.-Y., Fan, H., Zhang, H., Rogers, D., Rempe, S., Atanassov, P., Cecchi, J. L., & Brinker. C. J. (2014). Atomic Layer Deposition of L-Alanine Polypeptide. *Journal of the American Chemical Society*, **136** (45), 15821.

8. Zhou, D., Ji, Z., Jiang, X., Dunphy, D. R., Brinker, C. J., & Keller, A. (2013). Influence of Material Properties on TiO2 Nanoparticle Agglomeration. *PLoS ONE* **8** (11), e81239.

9. Xiong, S., Dunphy, D. R., Wilkinson, D. C., Jiang, Z., Strzalka, J., Wang, J., Su, Y., de Pablo, J. J., & Brinker, C. J. (2013). Revealing the Interfacial Self-Assembly Pathway of Large-Scale, Highly-Ordered, Nanoparticle/Polymer Monolayer Arrays at an Air/Water Interface. *Nano Letters*, **13** (3), 1041.

10. Kendall, E. L., Ngassam, V. N., Gilmore, S. F., Brinker, C. J., & Parikh, A. N. (2013). Lithographically Defined Macroscale Modulation of Lateral Fluidity and Phase Separation Realized via Patterned Nanoporous Silica-Supported Phospholipid Bilayers. *Journal of the American Chemical Society*, **135** (42), 15718.

11. Chou, S. S., Kaehr, B., Kim, J., Foley, B. M., De, M., Hopkins, P. E., Huang, J., Brinker, C. J., & Dravid, V. P. (2013). Chemically Exfoliated MoS2 as Near-Infrared Photothermal Agents. *Angewandte Chemie-International Edition*, **52** (15), 4160.

12. Brinker, C. J. & Clem, P. G. (2013). Quartz on Silicon. *Science* **340**, 818-819.

13. Zarzar, L. D., Swartzentruber, B. S., Harper, J. C., Dunphy, D. R., Brinker, C. J., Aizenberg, J. & Kaehr, B. (2012). Multiphoton Lithography of Nanocrystalline Platinum and Palladium for Site-Specific Catalysis in 3D Microenvironments. *Journal of the American Chemical Society* **134**, 4007-4010.

14. Jiang, X., Bao, L., Cheng, Y.-S., Dunphy, D. R., Li, X. & Brinker, C. J. (2012). Aerosol-assisted synthesis of monodisperse single-crystalline [small alpha]-cristobalite nanospheres. *Chemical Communications* **48**, 1293-1295.

15. Zarzar, L. D., Kim, P., Kolle, M., Brinker, C. J., Aizenberg, J. & Kaehr, B. (2011). Direct writing and actuation of three-dimensionally patterned hydrogel pads on micropillar supports. *Angew Chem Int Ed Engl* **50**, 9356-60.

16. Xiong, S., Molecke, R., Bosch, M., Schunk, P. R. & Brinker, C. J. (2011). Transformation of a Close-Packed Au Nanoparticle/Polymer Monolayer into a Large Area Array of Oriented Au Nanowires via E-beam Promoted Uniaxial Deformation and Room Temperature Sintering. *Journal of the American Chemical Society* **133**, 11410-11413.

17. Luk, T. S., Xiong, S., Chow, W. W., Miao, X., Subramania, G., Resnick, P. J., Fischer, A. J. & Brinker, C. J. (2011). Anomolous Enhanced Emission from PbS Quantum Dots on a Photonic-Crystal Microcavity. *J. Opt. Soc. Am. B* **28**, 1365-1373.

18. Khripin, C. Y., Pristinski, D., Dunphy, D. R., Brinker, C. J. & Kaehr, B. J. (2011). Protein-Directed Assembly of Arbitrary Three-Dimensional Nanoporous Silica Architectures. *ACS Nano* **5**, 1401-1409.

19. Jiang, X., Liu, N., Assink, R. A., Jiang, Y. & Brinker, C. J. (2011). Photoresponsive release from azobenzene-modified single cubic crystal NaCl/silica particles. *J. Nanomaterials* **2011**, 1-6.

20. Jiang, X., Jiang, Y.-B. & Brinker, C. J. (2011). Hydrothermal synthesis of monodisperse single-crystalline alpha-quartz nanospheres. *Chemical Communications* **47**, 7524-7526.

21. Hopkins, P. E., Kaehr, B., Phinney, L. M., Koehler, T. P., Grillet, A. M., Dunphy, D., Garcia, F. & Brinker, C. J. (2011). Measuring the Thermal Conductivity of Porous, Transparent SiO2 Films With Time Domain Thermoreflectance. *Journal of Heat Transfer-Transactions of the Asme* **133**, 061601.

22. Dunphy, D. R., Garcia, F. L., Kaehr, B., Khripin, C. Y., Collord, A. D., Baca, H. K., Tate, M. P., Hillhouse, H. W., Strzalka, J. W., Jiang, Z., Wang, J. & Brinker, C. J. (2011).

Tricontinuous Cubic Nanostructure and Pore Size Patterning in Mesostructured Silica Films Templated with Glycerol Monooleate. *Chemistry of Materials* **23**, 2107-2112.

23. Dunphy, D. R., Garcia, F. L., Jiang, Z., Strzalka, J., Wang, J. & Brinker, C. J. (2011). X-Ray characterization of self-assembled long-chain phosphatidylcholine/bile salt/silica mesostructured films with nanoscale homogeneity. *Chemical Communications* **47**, 1806-1808.

24. Xiong, S. S., Miao, X. Y., Spencer, J., Khripin, C., Luk, T. S. & Brinker, C. J. (2010). Integration of a Close-Packed Quantum Dot Monolayer with a Photonic-Crystal Cavity Via Interfacial Self-Assembly and Transfer. *Small* **6**, 2126-2129.

25. Moghaddam, S., Pengwang, E., Jiang, Y. B., Garcia, A. R., Burnett, D. J., Brinker, C. J., Masel, R. I. & Shannon, M. A. (2010). An inorganic-organic proton exchange membrane for fuel cells with a controlled nanoscale pore structure. *Nature Nanotechnology* **5**, 230-236.

26. Khripin, C. Y., Brinker, C. J. & Kaehr, B. (2010). Mechanically tunable multiphoton fabricated protein hydrogels investigated using atomic force microscopy. *Soft Matter* **6**, 2842-2848.

27. Kendall, E. L., Mills, E., Liu, J. W., Jiang, X. M., Brinker, C. J. & Parikh, A. N. (2010). Salt-induced lipid transfer between colloidal supported lipid bilayers. *Soft Matter* **6**, 2628-2632.

28. Kaehr, B. & Brinker, C. J. (2010). Using bacterial cell growth to template catalytic asymmetry. *Chemical Communications* **46**, 5268-5270.

29. Jiang, X. M., Ward, T. L., Cheng, Y. S., Liu, J. W. & Brinker, C. J. (2010). Aerosol fabrication of hollow mesoporous silica nanoparticles and encapsulation of L-methionine as a candidate drug cargo. *Chemical Communications* **46**, 3019-3021.

30. Jiang, X. M. & Brinker, C. J. (2010). Rigid templating of high surface-area, mesoporous, nanocrystalline rutile using a polyether block amide copolymer template. *Chemical Communications* **46**, 6123-6125.

31. Jiang, X., Ward, T. L., van Swol, F. & Brinker, C. J. (2010). Numerical Simulation of Ethanol-Water-NaCl Droplet Evaporation. *Industrial & Engineering Chemistry Research* **49**, 5631-5643.

32. Chen, Z., Jiang, Y. B., Dunphy, D. R., Adams, D. P., Hodges, C., Liu, N. G., Zhang, N., Xomeritakis, G., Jin, X. Z., Aluru, N. R., Gaik, S. J., Hillhouse, H. W. & Brinker, C. J. (2010). DNA translocation through an array of kinked nanopores. *Nature Materials* **9**, 667-675.

33. Zhang, L. N., Singh, S., Tian, C. S., Shen, Y. R., Wu, Y., Shannon, M. A. & Brinker, C. J. (2009). Nanoporous silica-water interfaces studied by sum-frequency vibrational spectroscopy. *Journal of Chemical Physics* **130**.

34. Xomeritakis, G., Tsai, C. Y., Jiang, Y. B. & Brinker, C. J. (2009). Tubular ceramic-supported sol-gel silica-based membranes for flue gas carbon dioxide capture and sequestration. *Journal of Membrane Science* **341**, 30-36.

35. Subramania, G., Lee, Y. J., Fischer, A. J., Luk, T. S., Brinker, C. J. & Dunphy, D. (2009). Emission modification of CdSe quantum dots by titanium dioxide visible logpile photonic crystal. *Applied Physics Letters* **95**.

36. Homer, C. J., Jiang, X. M., Ward, T. L., Brinker, C. J. & Reid, J. P. (2009). Measurements and simulations of the near-surface composition of evaporating ethanol-water droplets. *Physical Chemistry Chemical Physics* **11**, 7780-7791.

37. Dunphy, D. R., Alam, T. M., Tate, M. P., Hillhouse, H. W., Smarsly, B., Collord, A. D., Carnes, E., Baca, H. K., Kohn, R., Sprung, M., Wang, J. & Brinker, C. J. (2009). Characterization of Lipid-Templated Silica and Hybrid Thin Film Mesophases by Grazing Incidence Small-Angle X-ray Scattering. *Langmuir* **25**, 9500-9509.

38. Pang, J. B., Xiong, S. S., Jaeckel, F., Sun, Z. C., Dunphy, D. & Brinker, C. J. (2008). Free-standing, patternable nanoparticle/polymer monolayer arrays formed by evaporation induced self-assembly at a fluid interface. *Journal of the American Chemical Society* **130**, 3284-+.

39. Pang, J. B., Stuecker, J. N., Jiang, Y. B., Bhakta, A. J., Branson, E. D., Li, P., Cesarano, J., Sutton, D., Calvert, P. & Brinker, C. J. (2008). Directed aerosol writing of ordered silica nanostructures on arbitrary surfaces with self-assembling inks. *Small* **4**, 982-989.

40. Dunphy, D., Fan, H. Y., Li, X. F., Wang, J. & Brinker, C. J. (2008). Dynamic investigation of gold nanocrystal assembly using in situ grazing-incidence small-angle X-ray scattering. *Langmuir* **24**, 10575-10578.

41. Dovgolevsky, E., Kirmayer, S., Lakin, E., Yang, Y., Brinker, C. J. & Frey, G. L. (2008). Self-assembled conjugated polymer-surfactant-silica mesostructures and their integration into light-emitting diodes. *Journal of Materials Chemistry* **18**, 423-436.

42. Cygan, R. T., Brinker, C. J., Nyman, M. D., Leung, K. & Rempe, S. B. (2008). A molecular basis for advanced materials in water treatment. *Mrs Bulletin* **33**, 42-47.

43. Yang, T. H., Yee, C. K., Amweg, M. L., Singh, S., Kendall, E. L., Dattelbaum, A. M., Shreve, A. P., Brinker, C. J. & Parikh, A. N. (2007). Optical detection of ion-channel-induced proton transport in supported phospholipid bilayers. *Nano Letters* **7**, 2446-2451.

44. Jiang, Y.-B., Xomeritakis, G., Chen, Z., Dunphy, D., Kissel, D. J., Cecchi, J. L. & Brinker, C. J. (2007). Sub-10 nm Thick Microporous Membranes Made by Plasma-Defined Atomic Layer Deposition of a Bridged Silsesquioxane Precursor. *Journal of the American Chemical Society* **129**, 15446-15447.

45. Fan, H. Y., Hartshorn, C., Buchheit, T., Tallant, D., Assink, R., Simpson, R., Kisse, D. J., Lacks, D. J., Torquato, S. & Brinker, C. J. (2007). Modulus-density scaling behaviour and framework architecture of nanoporous self-assembled silicas. *Nature Materials* **6**, 418-423.

46. De, G., Kohn, R., Xomeritakis, G. & Brinker, C. J. (2007). Nanocrystalline mesoporous palladium activated tin oxide thin films as room-temperature hydrogen gas sensors. *Chemical Communications*, 1840-1842.

47. Wright, A., Gabaldon, J., Burckel, D. B., Jiang, Y. B., Tian, Z. R., Liu, J., Brinker, C. J. & Fan, H. Y. (2006). Hierarchically organized nanoparticle mesostructure arrays formed through hydrothermal self-assembly. *Chemistry of Materials* **18**, 3034-3038.

48. Truesdell, R., Mammoli, A., Vorobieff, P., van Swol, F. & Brinker, C. J. (2006). Drag reduction on a patterned superhydrophobic surface. *Physical Review Letters* **97**.

49. Singh, S., Houston, J., van Swol, F. & Brinker, C. J. (2006). Superhydrophobicity - Drying transition of confined water. *Nature* **442**, 526-526.

50. Rodriguez, A. T., Chen, M., Chen, Z., Brinker, C. J. & Fan, H. Y. (2006). Nanoporous carbon nanotubes synthesized through confined hydrogen-bonding self-assembly. *Journal of the American Chemical Society* **128**, 9276-9277.

51. Pang, J. B., Yang, L., Loy, D. A., Peng, H. S., Ashbaugh, H. S., Mague, J., Brinker, C. J. & Lu, Y. F. (2006). Mesoscopically ordered organosilica and carbon-silica hybrids with uniform morphology by surfactant-assisted self-assembly of organo bis-silanetriols. *Chemical Communications*, 1545-1547.

52. Jiang, Y. B., Liu, N. G., Gerung, H., Cecchi, J. L. & Brinker, C. J. (2006). Nanometer-thick conformal pore sealing of self-assembled mesoporous silica by plasma-assisted atomic layer deposition. *Journal of the American Chemical Society* **128**, 11018-11019.

53. Gerung, H., Zhao, Y., Wang, L., Jain, R. K., Boyle, T. J., Brinker, C. J. & Han, S. M. (2006). Two-photon absorption of matrix-free Ge nanocrystals. *Applied Physics Letters* **89**.

54. Gerung, H., Boyle, T. J., Tribby, L. J., Bunge, S. D., Brinker, C. J. & Han, S. M. (2006). Solution synthesis of germanium nanowires using a Ge2+ alkoxide precursor. *Journal of the American Chemical Society* **128**, 5244-5250.

55. Fan, H. Y., Wright, A., Gabaldon, J., Rodriguez, A., Jiang, Y. & Brinker, C. J. (2006). Three-dimensionally ordered gold nanocrystal/silica superlattice thin films synthesized via sol-gel self-assembly. *Advanced Functional Materials* **16**, 891-895.

56. Fan, H. Y., Gabaldon, J., Brinker, C. J. & Jiang, Y. B. (2006). Ordered nanocrystal/silica particles self-assembled from nanocrystal micelles and silicate. *Chemical Communications*, 2323-2325.

57. Brinker, C. J. & Dunphy, D. R. (2006). Morphological control of surfactant-templated metal oxide films. *Current Opinion in Colloid & Interface Science* **11**, 126-132.

58. Yang, K., Fan, H. Y., Malloy, K. J., Brinker, C. J. & Sigmon, T. W. (2005). Optical and electrical properties of self-assembled, ordered gold nanocrystal/silica thin films prepared by sol-gel processing. *Thin Solid Films* **491**, 38-42.

59. Xomeritakis, G., Tsai, C. Y. & Brinker, C. J. (2005). Microporous sol-gel derived aminosilicate membrane for enhanced carbon dioxide separation. *Separation and Purification Technology* **42**, 249-257.

60. Torquato, S., Donev, A., Evans, A. G. & Brinker, C. J. (2005). Manufacturable extremal low-dielectric, high-stiffness porous materials. *Journal of Applied Physics* **97**.

61. Smarsly, B., Gibaud, A., Ruland, W., Sturmayr, D. & Brinker, C. J. (2005). Quantitative SAXS analysis of oriented 2D hexagonal cylindrical silica mesostructures in thin films obtained from nonionic surfactants. *Langmuir* **21**, 3858-3866.

62. Peng, H. S., Tang, J., Pang, J. B., Chen, D. Y., Yang, L., Ashbaugh, H. S., Brinker, C. J., Yang, Z. Z. & Lu, Y. F. (2005). Polydiacetylene/silica nanocomposites with tunable mesostructure and thermochromatism from diacetylenic assembling molecules. *Journal of the American Chemical Society* **127**, 12782-12783.

63. Nyman, M., Ingersoll, D., Singh, S., Bonhomme, F., Alam, T. M., Brinker, C. J. & Rodriguez, M. A. (2005). Comparative study of inorganic cluster-surfactant arrays. *Chemistry of Materials* **17**, 2885-2895.

64. Gogte, S., Vorobieff, P., Truesdell, R., Mammoli, A., van Swol, F., Shah, P. & Brinker, C. J. (2005). Effective slip on textured superhydrophobic surfaces. *Physics of Fluids* **17**.

65. Gerung, H., Bunge, S. D., Boyle, T. J., Brinker, C. J. & Han, S. M. (2005). Anhydrous solution synthesis of germanium nanocrystals from the germanium(II) precursor Ge[N(SiMe3)(2)](2). *Chemical Communications*, 1914-1916.

66. Gerung, H., Brinker, C. J., Brueck, S. R. J. & Han, S. M. (2005). In situ real-time monitoring of profile evolution during plasma etching of mesoporous low-dielectric-constant SiO2. *Journal of Vacuum Science & Technology A* **23**, 347-354.

67. Fan, H. Y., Leve, E. W., Scullin, C., Gabaldon, J., Tallant, D., Bunge, S., Boyle, T., Wilson, M. C. & Brinker, C. J. (2005). Surfactant-assisted synthesis of water-soluble and biocompatible semiconductor quantum dot micelles. *Nano Letters* **5**, 645-648.

68. Fan, H. Y., Leve, E., Gabaldon, J., Wright, A., Haddad, R. E. & Brinker, C. J. (2005). Ordered two- and three-dimensional arrays self-assembled from water-soluble nanocrystal-micelles. *Advanced Materials* **17**, 2587-+.

69. Fan, H. Y., Chen, Z., Brinker, C. J., Clawson, J. & Alam, T. (2005). Synthesis of organo-silane functionalized nanocrystal micelles and their self-assembly. *Journal of the American Chemical Society* **127**, 13746-13747.

70. Doshi, D. A., Shah, P. B., Singh, S., Branson, E. D., Malanoski, A. P., Watkins, E. B., Majewski, J., van Swol, F. & Brinker, C. J. (2005). Investigating the interface of superhydrophobic surfaces in contact with water. *Langmuir* **21**, 7805-7811.

71. Xu, Z. P., Braterman, P. S., Yu, K., Xu, H. F., Wang, Y. F. & Brinker, C. J. (2004). Unusual hydrocarbon chain packing mode and modification of crystallite growth habit in the self-assembled nanocomposites zinc-aluminum-hydroxide oleate and elaidate (cis- and trans-[Zn2Al(OH)(6)(CH3(CH2)(7)CH=CH(CH2)(7)COO-)] and magnesium analogues. *Chemistry of Materials* **16**, 2750-2756.

72. Song, Y. J., Yang, Y., Medforth, C. J., Pereira, E., Singh, A. K., Xu, H. F., Jiang, Y. B., Brinker, C. J., van Swol, F. & Shelnutt, J. A. (2004). Controlled synthesis of 2-D and 3-D dendritic platinum nanostructures. *Journal of the American Chemical Society* **126**, 635-645.

73. Liu, N. G., Dunphy, D. R., Atanassov, P., Bunge, S. D., Chen, Z., Lopez, G. P., Boyle, T. J. & Brinker, C. J. (2004). Photoregulation of mass transport through a photoresponsive azobenzene-modified nanoporous membrane. *Nano Letters* **4**, 551-554.

74. Fan, H. Y., Yang, K., Boye, D. M., Sigmon, T., Malloy, K. J., Xu, H. F., Lopez, G. P. & Brinker, C. J. (2004). Self-assembly of ordered, robust, three-dimensional gold nanocrystal/silica arrays. *Science* **304**, 567-571.

75. Yu, K., Smarsly, B. & Brinker, C. J. (2003). Self-assembly and characterization of mesostructured silica films with a 3D arrangement of isolated spherical mesopores. *Advanced Functional Materials* **13**, 47-52.

76. Yang, Y., Lu, Y. F., Lu, M. C., Huang, J. M., Haddad, R., Xomeritakis, G., Liu, N. G., Malanoski, A. P., Sturmayr, D., Fan, H. Y., Sasaki, D. Y., Assink, R. A., Shelnutt, J. A., van Swol, F., Lopez, G. P., Burns, A. R. & Brinker, C. J. (2003). Functional nanocomposites prepared by self-assembly and polymerization of diacetylene surfactants and silicic acid. *Journal of the American Chemical Society* **125**, 1269-1277.

77. Xomeritakis, G., Naik, S., Braunbarth, C. M., Cornelius, C. J., Pardey, R. & Brinker, C. J. (2003). Organic-templated silica membranes - I. Gas and vapor transport properties. *Journal of Membrane Science* **215**, 225-233.

78. Xomeritakis, G., Braunbarth, C. M., Smarsly, B., Liu, N., Kohn, R., Klipowicz, Z. & Brinker, C. J. (2003). Aerosol-assisted deposition of surfactant-templated mesoporous silica membranes on porous ceramic supports. *Microporous and Mesoporous Materials* **66**, 91-101.

79. Wu, X., Yu, K., Brinker, C. J. & Ripmeester, J. (2003). Mesostructured MTES-derived silica thin film with spherical voids investigated by TEM: 2. Dislocations and strain relaxation. *Langmuir* **19**, 7289-7294.

80. Wang, D. H., Zhou, W. L., McCaughy, B. F., Hampsey, J. E., Ji, X. L., Jiang, Y. B., Xu, H. F., Tang, J. K., Schmehl, R. H., O'Connor, C., Brinker, C. J. & Lu, Y. F. (2003). Electrodeposition of metallic nanowire thin films using mesoporous silica templates. *Advanced Materials* **15**, 130-+.

81. Smarsly, B., Xomeritakis, G., Yu, K., Liu, N. G., Fan, H. Y., Assink, R. A., Drewien, C. A., Ruland, W. & Brinker, C. J. (2003). Microstructural characterization of polystyrene-block-poly(ethylene oxide)-templated silica films with cubic-ordered spherical mesopores. *Langmuir* **19**, 7295-7301.

82. McCaughey, B., Costello, C., Wang, D. H., Hampsey, J. E., Yang, Z. Z., Li, C. J., Brinker, C. J. & Lu, Y. F. (2003). Self-assembly of mesostructured conjugated poly(2,5-thienylene ethynylene)/silica nanocomposites. *Advanced Materials* **15**, 1266-+.

83. Lu, Y. F., McCaughey, B. F., Wang, D. H., Hampsey, J. E., Doke, N., Yang, Z. Z. & Brinker, C. J. (2003). Aerosol-assisted formation of mesostructured thin films. *Advanced Materials* **15**, 1733-+.

84. Liu, N. G., Chen, Z., Dunphy, D. R., Jiang, Y. B., Assink, R. A. & Brinker, C. J. (2003). Photoresponsive nanocomposite formed by self-assembly of an azobenzene-modified silane. *Angewandte Chemie-International Edition* **42**, 1731-1734.

85. Liu, N. G., Assink, R. A., Smarsly, B. & Brinker, C. J. (2003). Synthesis and characterization of highly ordered functional mesoporous silica thin films with positively chargeable -NH2 groups. *Chemical Communications*, 1146-1147.

86. Liu, N. G., Assink, R. A. & Brinker, C. J. (2003). Synthesis and characterization of highly ordered mesoporous thin films with -COOH terminated pore surfaces. *Chemical Communications*, 370-371.

87. Gibaud, A., Grosso, D., Smarsly, B., Baptiste, A., Bardeau, J. F., Babonneau, F., Doshi, D. A., Chen, Z., Brinker, C. J. & Sanchez, C. (2003). Evaporation-controlled self-assembly of silica surfactant mesophases. *Journal of Physical Chemistry B* **107**, 6114-6118.

88. Gibaud, A., Baptiste, A., Doshi, D. A., Brinker, C. J., Yang, L. & Ocko, B. (2003). Wall thickness and core radius determination in surfactant templated silica thin films using GISAXS and X-ray reflectivity. *Europhysics Letters* **63**, 833-839.
89. Garnweitner, G., Smarsly, B., Assink, R., Ruland, W., Bond, E. & Brinker, C. J. (2003). Self-assembly of an environmentally responsive polymer/silica nanocomposite. *Journal of the American Chemical Society* **125**, 5626-5627.
90. Dunphy, D. R., Singer, S., Cook, A. W., Smarsly, B., Doshi, D. A. & Brinker, C. J. (2003). Aqueous stability of mesoporous silica films doped or grafted with aluminum oxide. *Langmuir* **19**, 10403-10408.
91. Doshi, D. A., Gibaud, A., Liu, N. G., Sturmayr, D., Malanoski, A. P., Dunphy, D. R., Chen, H. J., Narayanan, S., MacPhee, A., Wang, J., Reed, S. T., Hurd, A. J., van Swol, F. & Brinker, C. J. (2003). In-situ X-ray scattering study of continuous silica-surfactant self-assembly during steady-state dip coating. *Journal of Physical Chemistry B* **107**, 7683-7688.
92. Doshi, D. A., Gibaud, A., Goletto, V., Lu, M. C., Gerung, H., Ocko, B., Han, S. M. & Brinker, C. J. (2003). Peering into the self-assembly of surfactant templated thin-film silica mesophases. *Journal of the American Chemical Society* **125**, 11646-11655.

4.2 Proceedings (2003 to 2017):

1. <u>Self-assembled, ordered gold nanocrystal/silica thin films for prism-based surface plasmon resonance sensors</u>. Yang, Kai; O'Brien, Michael J.; Malloy, Kevin J.; Sigmon, Thomas W.; Fan, Hongyou; Lopez, Gabriel P.; Brinker, C. Jeffrey; Sheik-Bahae, Mansoor. Quantum Electronics and Laser Science Conference (QELS); 2005; v.2, p.1082-1084. Conference: 2005 Quantum Electronics and Laser Science Conference (QELS); May 22-27 2005; Baltimore, MD
2. <u>Surfactant-assisted synthesis of water-soluble and biocompatible semiconductor quantum dot-micelles</u>. Fan, Hongyou; Leve, Erik W.; Scullin, Chessa; Tallant, David; Wilson, Michael C.; <u>Brinker, C. Jeffrey</u>. Progress in Biomedical Optics and Imaging-Proceedings of SPIE; 2005; v.5705, p.92-100. Conference: Nanobiophotonics and Biomedical Applications II; Jan 24-27 2005; San Jose, CA
3. <u>Electrical and optical properties of self-assembled, ordered gold nanocrystal/silica thin films prepared by sol-gel processing.</u> Yang, K; Fan, H; O'Brien, MJ; La Fontaine, S.; Lopez, GP; Malloy, KJ; Brinker, CJ; Sigmon, TW. Proceedings of the Materials Research Society. Micro- and Nanosystems–Materials and Devices 872, 103-108 (2005).
4. <u>Self-assembly and integration of ordered, robust three-dimensional gold nanocrystal/metal oxide superlattices</u>. Fan, H; Yang, K; Gabaldon, JP; Boye, DM; Sigmon, TW; Malloy, KJ; Brinker, CJ; Proceedings of NSTI Nanotech 2005, p. 765-768
5. <u>The Study of interaction of superhydrophobic (SH) materials with fluids using TSM sensors.</u> Kwoun, SJ; Cairncross, R; Lec, RM; Shah, P.; Brinker, C.J. Proceedings of the 2005 IEEE. International, Frequency Control Symposium and Exposition, August 29-31, 2005; p. 78-83

4.3 Books Edited (2003 to 2017):

1. <u>Annual Review of Nano Research</u> – Volume 3
   Cao, Guozhong and Brinker, C. Jeffrey, editors
   World Scientific Publishing Co. Ltd., Singapore/London, 2010

2. <u>Annual Review of Nano Research</u> – Volume 2
   Cao, Guozhong and Brinker, C. Jeffrey, editors
   World Scientific Publishing Co. Ltd., Singapore/London, 2008

3. <u>Annual Review of Nano Research</u> – Volume 1
   Cao, Guozhong and Brinker, C. Jeffrey, editors
   World Scientific Publishing Co. Ltd., Singapore/London, 2006

4. <u>Self-Assembled Nanostructured Materials</u>
   Lu, Yunfeng; Brinker, C. Jeffrey; Antonietti, Markus; and Chunli B., editors
   MRS Symposia Proceedings, Volume 775
   Materials Research Society, Pittsburgh, PA, 2003.

4.4 Book Chapters (2003 to 2017):

1. Diallo, M. & Brinker, C. J. (September 2010). Nanotechnology for Sustainability: Environment, Water, Food, Minerals, and Climate. In *Nanotechnology Research Directions for Societal Needs in 2020, Retrospective and Outlook (NSF WTEC Panel Report)* (Roco, M. C., Mirkin, C. A. & Hersam, M. C., eds.). Springer, Berlin and Boston.

2. Brinker, C. J. & Ginger, D. (September 2010). Nanotechnology for Sustainability: Energy Conversion, Storage, and Conversion. In *Nanotechnology Research Directions for Societal Needs in 2020, Retrospective and Outlook (NSF WTEC Panel Report)* (Roco, M. C., Mirkin, C. A. & Hersam, M. C., eds.). Springer, Berlin and Boston.

3. Dunphy, Darren R., Smarsly, Bernd, and Brinker, C. Jeffrey. (June 2010) Control of Morphology in Mesoporous and Mesostructured Hybrid Materials. In *The Supramolecular Chemistry of Organic-Inorganic Hybrid Materials. (* Rurack, Knut, ed.) John Wiley & Sons, Inc., Hoboken, NJ.

4. Liu, Nanguo and Brinker, C. Jeffrey. (April 2009) Photoresponsive Nanocomposite Materials Including Axobenzene-Containing Polysilsesquixane Films and Photoswitched Nanovalves. In *Smart Light-Responsive Materials: Azobenzene Containing Polymers and Liquid Crystals* (Zhao, Yue and Ikeda,Tomiki, eds.) John Wiley & Sons, Inc., Hoboken, NJ.

5. Fan, Hongyou and Brinker, C. Jeffrey. (May 2004) Evaporation-Induced Self-Assembly to functional Nanostructures. In *Mesoporous Crystals and Related Nano-Structured Materials.* (Terasaki, Osuma, ed.) Studies in Surface Science and Catalysis, (Book Series, Vol 148) Elsevier.

4.5 Patents Issued and Applications Filed (2003 to 2017):

4.5.1 Patents issued / allowed

1. Method for Atomic Layer Deposition, U.S. Patent No. 9,605,344, issued 03/28/2017.
2. Biomimetic Membranes and Method of Making Biomimetic Membranes, U.S. Patent No. 9,486,742, issued 11/08/2016.
3. Enzymatically Active High-Flux Selectively Gas-Permable Membranes, U.S. Patent No. 9,242,210, issued 1/26/2016.
4. Aerosol Fabrication Methods for Monodisperse Nanoparticles, U.S. Patent No. 8,864,045, issued 10/21/2014.
5. Freezing Assisted Fabrication of Nano and Micro Hollow Cubic Metal Oxides, U.S. Patent No. 8,501,057, issued 08/06/2013.

6. Methods for Preparing High Crystallinity and Surface Area Porous Metal Oxides, U.S. Patent No. 8,318,127, issued 11/27/2012.
7. Aerosol Method for Nano Silver-Silica Composite Anti-Microbial Agent, U.S. Patent No. 8,246,933, issued 08/21/2012.
8. Ultra-Thin Microporous/Hybrid Materials, U.S. Patent No. 8,187,678, issued 5/29/2012.
9. Method of Making Dense, Conformal, Ultra-Thin Cap Layers of Nanoporous Low-k ILD by Plasma-Assisted Atomic Layer Deposition, U.S. Patent No. 7,947,579, issued 5/24/2011.
10. Method for Making Surfactant-Templated Thin Films, U.S. Patent No. Patent No. RE 41,612E, reissued 08/31/2010.
11. Prototyping of Patterned Functional Nanostructures, U.S. Patent No. 6,913,832, issued 07/05/2005.
12. Inorganic Dual-Layer Microporous Supported Membranes, U.S. Patent No. 6,536,604, issued 03/25/2003.

4.5.2 Patent applications filed

1. Generation of Mesoporous Materials Using Multiphase Surfactant Systems; PCT Appl. PCT/US16/22056, filed 03/11/2016.
2. Enzymatically Active High-Flux Selectively Gas-Permeable Membranes; Divisional Appl. 14/942,707, filed 11/16/2015.
3. Innovative Nanopore Sequencing Technology Including a Self-Assembled Porous Membrane; Utility Appl. 14/555,453, filed 11/26/2014.
4. Ultra-thin microporous/hybrid membranes made by successive surface activation and reaction. UNM PS-0828; Provisional application 60/988,180, filed 11/15/2007.
5. Method of Making Dense, Conformal, Ultra-Thin Cap Layers of Nanoporous Low-k ILD by Plasma-Assisted Atomic Layer Deposition, UNM-745, provisional application filed 02/13/2006.

4.6 Awards and Honors (2003-2017):

4.6.1 PI Awards, C. Jeffrey Brinker (National Academy of Engineering, 2002)

2003 Materials Research Society MRS Medal
2005 University of New Mexico Research Excellence Award
2006 Directeur de Recherche Universite Pierre et Marie Curie, Paris VI
2006 Rutgers University Distinguished Alumnus Award
2007 R&D 100 Award: Self-Assembling Process for Fabricating Tailored Thin Films
2008 R&D 100 Award: Patterned Superhydrophobic Surfaces
2008 Edward R. Orton Jr. Memorial Award, American Ceramic Society and ASM
2009 IBM Distinguished Lecturer in Materials Science and Engineering
2009 Named Fellow of the Materials Research Society
2010 Robert B. Sosman Award, American Ceramics Society
2011 R&D 100 Award: Biomimetic Water Purification Membranes
2012 Médaille du Collège de France, Paris
2012 Federal Laboratory Consortium, Notable Technology Development Award – Biomimetic Membranes
2013 Federal Laboratory Consortium, Outstanding Regional Partnership – UNM
Health Sciences Center/Sandia National Laboratories Partnership

2014 Federal Laboratory Consortium, Notable Technology Development Award, Nano-Stabilized Enzymatic Membrane for CO2 Capture

2014 Elected to Board of Directors, Materials Research Society (3 year term)

2015 University of New Mexico STC, Innovation Fellow Award

2015 Gold Award in Green Technology: R&D 100 Green Technology Special Recognition Award for CO2 Memzyme

2015 R&D 100 Award, CO2 Memzyme is an ultra-thin membrane that is the first cost-effective technology for carbon dioxide separation and capture to meet and exceed DOE targets for helping to reduce the threat of climate change.

2015 UNM Presidential Medal of Distinction - Recipients are recognized for thoughts and actions advancing the highest ideals of New Mexico citizens.

2016 - Elected to the National Academy of Inventors - Election to NAI Fellow status is a high professional distinction accorded to academic inventors who have demonstrated a highly prolific spirit of innovation in creating or facilitating outstanding inventions that have made a tangible impact on quality of life, economic development, and welfare of society.

2017 – Lifetime Achievement Award in Sol-Gel Science – International Sol Gel Society

4.6.2 *Major National and International Graduate Student Awards and Fellowships**:*

1. Lauren Zarzar, Harvard University, Akzo-Nobel Student Award, American Chemical Society, Denver, CO, August 28 – September 2, 2011   (for work performed at Sandia National Labs/University of New Mexico during summer 2010-2011; published in *Angewandte Chemie*; mentored by Bryan Kaehr, C. Jeffrey Brinker)

2. Mekensey Buley (PhD student) Graduate Research Fellowship (Nanoparticle Human Interactions), Sandia National Laboratories/University of New Mexico Excellence in Engineering Research Program, 2011-2012.

3. Annikka Jensen (PhD student), Integrated Graduate Education and Research Traineeship (IGERT) Fellowship in Integrating Nanotechnology with Cell Biology and Neuroscience, 2010-2012.

4. Carlee Ashley (PhD May 2010), Harry S. Truman Postdoctoral Fellowship, Sandia National Laboratories, 2010-2013

5. Carlee Ashley (PhD May 2010), Outstanding Graduate student 2010, Chemical and Nuclear Engineering department, the University of New Mexico.

6. Carlee Ashley (PhD May 2010), Michael Gallegos Prize for Entrepreneurship, $25,000, University of New Mexico Technology Business Plan Competition, April 2010

7. Carlee Ashley (PhD May 2010), Materials Research Society Graduate Student Silver award, December 2009

8. Carlee Ashley (PhD May 2010), Materials Research Society Fall Meeting, Top Poster Award, 2008, *Targeted in-vitro Drug Delivery.*

9. Carlee Ashley, Darren Dunphy, Eric Carnes, C. Jeffrey Brinker, Materials Research Society Fall Meeting, Top Poster Award Finalist, 2008, *Self-assembly of Well-Ordered, Close-Packed 2D Arrays of Recombinant Virus-Like Particles that Nucleate the Growth of Inorganic Nanomaterials.*

10. Jennifer Pelowitz (PhD student), Integrated Graduate Education and Research Traineeship (IGERT) Fellowship in Integrating Nanotechnology with Cell Biology and Neuroscience, 2009-2011.

11. Patrick Johnson (PhD student), Integrated Graduate Education and Research Traineeship (IGERT) Fellowship in Integrating Nanotechnology with Cell Biology and Neuroscience, 2008-2011

12. Adam Wise (PhD student) Integrated Graduate Education and Research Traineeship (IGERT) Fellowship in Nanoscience and Microsystems, National Science Foundation, 2007-2010

13. Eric Carnes (PhD July 2008), Carlee Ashley (PhD May 2010), NSF Ethics Fellows, the University of New Mexico, National Science Foundation Pilot Program between School of Engineering and Department of Philosophy graduate students to develop and team-teach *Engineering Ethics*, 2007-2008.

14. Carlee Ashley (PhD 2010), NSF Interdisiplinary Graduate Research Trainee (IGERT) Fellowship, 2007-2009

15. Eric Carnes (PhD 2008), NSF Interdisiplinary Graduate Research Trainee (IGERT) Fellowship, 2006-2008

16. Shisheng Xiong (PhD 2010), Y. Gao, J. Pang, J. Grey, C.Jeffrey Brinker, Materials Research Society Fall Meeting, Top Poster Award Finalist, 2008, *Functional Monolayer Nanoparticle/polymer Composites Formed by EISA at a Fluid Interface*.

17. Carlee Ashley, First Prize, Graduate student Oral Competition, *GISAXS Characterization of 2D Bacteriophage Arrays Deposited via Convective Assembly,* NM Chapter of the American Vacuum Society, May 22, 2007, Albuquerque, NM (paid trip to AVS International Symposium, Seattle, WA, October 2007).

18. Carlee Ashley, Eric Carnes, Helen Baca, Jeff Brinker. First Prize, Graduate student poster competition *Cell-Directed Assembly of 3-D Bio-Nano Interfaces*. Industrial Advisory Board Meeting of the UNM/RUTGERS/PENN STATE Ceramic and Composite Materials Center (CCMC), March 13, 2007, Albuquerque, NM

19. Yunfeng Lu (PhD 1998), Presidential Early Career Award for Scientists and Engineers (PECASE), 2005-2010.

20. Yunfeng Lu (PhD 1998), American Chemical Society Unilever (Young Investigator) Award in Colloid and Surface Chemistry, 2005

21. Helen K. Baca (PhD 2005), Materials Research Society Student Gold Award, 2005

22. Helen Baca (PhD candidate), National Science and Defense Graduate Fellowship, 2003

4.6.3 Undergraduate Student Awards

1. Katie Epler, Top Junior Chemical Engineering student, University of New Mexico, May 2012

2. Katie Epler, Albuquerque Chapter Scholarship by the New Mexico Engineering Foundation, New Mexico Society of Professional Engineers, 2001 - present

3. American Vacuum Society, May 24, 2011, Albuquerque, NM, First prize, poster competition, D. Padilla, KE Epler, RE Castillo, G. Phillips, D. Wilkinson, C. Burgard, B. Wilkinson, N. Johannes, EC Carnes, CJ Brinker and CE Ashley, Development of Porous Nanoparticle-Supported Lipid Bilayers (Protocells) for Targeted-Gene Delivery

4. R. E. Castillo, K.E. Epler, D. Wilkinson, N. Johannes, A. Jensen, C.E. Ashley, E.C. Carnes, and C.J. Brinker, A new approach to cancer therapeutics using nanoparticle-based targeted drug delivery. (First place undergrad poster competition) The 22nd Annual Rio Grande Symposium on Advanced Materials, October 11, 2010, Albuquerque, NM. First place undergrad poster award

5. Alison Stace-Naughton, Dartmouth visiting undergrad (summer 2008, winter 2009; co-author JACS 2009 paper), Goldwater Fellowship, 2009-2011

6. DeAnna Lopez, First prize, Spectral Image category, Confocal microscope image "Cells Take the Lead", Microscopy Facility Image Competition, Cancer Center Fluorescence Microscopy Facility, University of New Mexico, February 2008, Albuquerque, NM. Published in Life in Print, Science News Online, Jan 26, 2008, vol. 173, no. 4, p. 56.

7. <u>Cynthia Douthit</u>, Second Prize, Undergraduate student poster competition, Examining Integration Techniques using Living Yeast Cells into Self-Assembled Nanostructures, AIChE 2008 Annual Meeting, November 16-21, 2008, Philadelphia, PA.
8. <u>Cynthia M. Douthit</u>, First Prize, Undergraduate student poster competition *Integrating Living Yeast Cells into Patterned Self-Assembled Nanostructures,* Rio Grande Symposium on Advanced Materials -- RGSAM, October 9, 2007, Albuquerque, NM
9. <u>Andrew Collord</u>, Third Prize, Undergraduate student poster competition, *Structure and Aqueous Stability of Surfactant-Templated Porous Films Synthesized using a Hybrid Inorganic/Organic Sol-Gel Precursor,* Rio Grande Symposium on Advanced Materials -- RGSAM, October 9, 2007, Albuquerque, NM
10. <u>DeAnna Lopez</u>, First Prize, Undergraduate Student Poster Competition, *Cell-to-cell communication among nano-confined cells in self-assembled matrices.* Sandia National Laboratories' Student Symposium, Albuquerque, NM , Aug 2, 2007
11. <u>Patrick Johnson</u>, First Prize, Undergraduate Student Poster Competition, *Gecko-Inspired Superadhesives,* Sandia National Laboratories' Student Symposium, Albuquerque, NM , Aug 2, 2007.
12. <u>DeAnna Lopez</u>, First Prize, Undergraduate Student Poster Competition, *Integration of Living Cells within Self-Assembled Nanostructures,* NM Chapter of the American Vacuum Society, May 22, 2007, Albuquerque, NM

5.0 References

1. Bonnemann, H. and R.M. Richards, *Nanoscopic metal particles - Synthetic methods and potential applications.* European Journal Of Inorganic Chemistry, 2001(10): p. 2455-2480.
2. Hashmi, A.S.K. and G.J. Hutchings, *Gold catalysis.* Angewandte Chemie-International Edition, 2006. **45**(47): p. 7896-7936.
3. Wegener, S.L., T.J. Marks, and P.C. Stair, *Design Strategies for the Molecular Level Synthesis of Supported Catalysts.* Accounts of Chemical Research, 2012. **45**(2): p. 206-214.
4. Rostovshchikova, T.N., et al., *New size effects in the catalysis by interacting copper nanoparticles.* Applied Catalysis A: General, 2005. **296**: p. 70-79.
5. Benson, E.E., et al., *Electrocatalytic and homogeneous approaches to conversion of CO2 to liquid fuels.* Chem. Soc. Rev., 2009. **38**: p. 89-99.
6. Fan, H.Y., et al., *Self-assembly of ordered, robust, three-dimensional gold nanocrystal/silica arrays.* Science, 2004. **304**(5670): p. 567-571.
7. Pang, J., et al., *Free-standing, patternable nanoparticle/polymer monolayer arrays formed by evaporation induced self-assembly at a fluid interface* J. amer. Chem. Soc., 2008. **130**: p. 3284-3285.
8. Dimitratos, N., J.A. Lopez-Sanchez, and G.J. Hutchings, *Slective liquid phase oxidation with supported metal nanoparticles.* Chemical Science, 2012. **3**(1): p. 20-44.
9. Hou, W., N.A. Dehm, and R.W.J. Scott, *Alcohol oxidations in aqueous solutions using Au, Pd, and bimetallic AuPd nanoparticle catalysts.* Journal of Catalysis, 2008. **253**(1): p. 22-27.
10. Villa, A., et al., *Au-Pd/AC as catalysts for alcohol oxidation: Effect of reaction parameters on catalytic activity and selectivity.* Applied Catalysis a-General, 2009. **364**(1-2): p. 221-228.

11. Vinod, C.P., K. Wilson, and A.F. Lee, *Recent advances in the heterogeneously catalysed aerobic selective oxidation of alcohols.* Journal of Chemical Technology and Biotechnology, 2011. **86**(2): p. 161-171.

12. Ma, Z. and S. Dai, *Design of novel structured gold nanocatalysts.* Acs Catalysis, 2011. **1**(7): p. 805-818.

13. Narayanan, S., J. Wang, and X.-M. Lin, *Dynamical self-assembly of nanocrystal supperlattices during colloidal droplet evaporation by in situ small angle x-ray scattering.* Phys. Rev. Lett., 2004. **93**(13).

14. Kalsin, A.M., et al., *Electrostatic assembly of binary nanoparticle crystals with a diamond-like lattice.* Science, 2006. **312**: p. 420-424.

15. Dunphy, D.R., et al., *Dynamic investigations of gold nanocrystal assembly using in situ grazing-incidnece small-angle x-ray scattering.* Langmuir, 2008. **24**(19): p. 10575-10578.

16. Shevchenko, E.V., et al., *Structural diversity in binary nanoparticle superlattices.* Nature, 2006. **439**: p. 55-59.

17. Smith, D.K., et al., *Self-assemlbed simple hexagonal AB binary nanocrystal superlattices: SEM, GISAXS, and defects.* J. amer. Chem. Soc., 2009. **131**: p. 3281-3290.

18. Sellinger, A., et al., *Continuous self-assembly of organic-inorganic nanocomposite coatings that mimic nacre.* Nature, 1998. **394**(6690): p. 256-260.

19. Jiang, Y.-B., et al., *Sub-10 nm Thick Microporous Membranes Made by Plasma-Defined Atomic Layer Deposition of a Bridged Silsesquioxane Precursor* **129**: p. 15446-15447

20. Garnweitner, G., et al., *Characterization of self-assembled lamellar thermoresponsive silica-hydrogel nanocomposite films.* Langmuir, 2004. **20**(22): p. 9811-9820.

21. Garnweitner, G., et al., *Self-assembly of an environmentally responsive polymer/silica nanocomposite.* Journal of the American Chemical Society, 2003. **125**(19): p. 5626-5627.

22. Liu, N.G., et al., *Photoresponsive nanocomposite formed by self-assembly of an azobenzene-modified silane.* Angewandte Chemie-International Edition, 2003. **42**(15): p. 1731-1734.

23. Liu, N.G., et al., *Photoregulation of mass transport through a photoresponsive azobenzene-modified nanoporous membrane.* Nano Letters, 2004. **4**(4): p. 551-554.

24. Liu, N.G., et al., *Self-directed assembly of photoactive hybrid silicates derived from an azobenzene-bridged silsesquioxane.* Journal of the American Chemical Society, 2002. **124**(49): p. 14540-14541.

25. Lu, Y.F., et al., *Self-assembly of mesoscopically ordered chromatic polydiacetylene/silica nanocomposites (vol 410, pg 913, 2001).* Nature, 2001. **411**(6837): p. 617-617.

26. Yang, Y., et al., *Functional nanocomposites prepared by self-assembly and polymerization of diacetylene surfactants and silicic acid.* Journal of the American Chemical Society, 2003. **125**(5): p. 1269-1277.

27. Fan, H.Y., et al., *Rapid prototyping of patterned functional nanostructures.* Nature, 2000. **405**(6782): p. 56-60.

28.   Doshi, D.A., *Optically defined multifunctional patterning of photosensitive thin-film silica mesophases (vol 290, pg 107, 2000).* Science, 2000. **290**(5499): p. 2075-2075.

29.   Lu, Y.F., et al., *Aerosol-assisted self-assembly of mesostructured spherical nanoparticles.* Nature, 1999. **398**(6724): p. 223-226.

30.   Lu, Y.F., et al., *Continuous formation of supported cubic and hexagonal mesoporous films by sol gel dip-coating.* Nature, 1997. **389**(6649): p. 364-368.

31.   Fan, H.Y., et al., *Self-assembled aerogel-like low dielectric constant films.* Journal of Non-Crystalline Solids, 2001. **285**(1-3): p. 79-83.

32.   Lu, Y.F., et al., *Chemical sensors based on hydrophobic porous sol-gel films and ATR-FTIR spectroscopy.* Sensors and Actuators B-Chemical, 1996. **36**(1-3): p. 517-521.

33.   Israelachvili, J.N., *Intermolecular and Surface Forces: With Application to Colloidal and Biological Systems.* 1992, London: Academic Press.

34.   Black, C.T., et al., *Spin-dependent tunneling in self-assembled cobalt-nanocrystal superlattices.* Science, 2000. **290**(5494): p. 1131-1134.

35.   Pileni, M.P., *Nanocrystal self-assemblies: Fabrication and collective properties.* Journal of Physical Chemistry B, 2001. **105**(17): p. 3358-3371.

36.   Mitchell, G.P., C.A. Mirkin, and R.L. Letsinger, *Programmed assembly of DNA functionalized quantum dots.* Journal of the American Chemical Society, 1999. **121**(35): p. 8122-8123.

37.   Xiong, S., et al., *Transformation of a Close-Packed Au Nanoparticle/Polymer Monolayer into a Large Area Array of Oriented Au Nanowires via E-beam Promoted Uniaxial Deformation and Room Temperature Sintering.* Journal of the American Chemical Society, 2011. **133**(30): p. 11410-11413.

38.   Xiong, S.S., et al., *Integration of a Close-Packed Quantum Dot Monolayer with a Photonic-Crystal Cavity Via Interfacial Self-Assembly and Transfer.* Small, 2010. **6**(19): p. 2126-2129.

39.   Shenhar, R., T.B. Norsten, and V.M. Rotello, *Polymer-mediated nanoparticle assembly: Structural control and applications.* Advanced Materials, 2005. **17**(6): p. 657-669.

40.   Ricco, A.J., G.C. Frye, and S.J. Martin, *Determination of BET surface areas of porous thin films using surface acoustic wave devices*
Langmuir, 1989. **5**: p. 273-276.

41.   Brinker, C.J., *Porous inorganic materials.* Current Opinion In Solid State & Materials Science, 1996. **1**(6): p. 798-805.

42.   Lu, Y.F., et al., *Microporous silica prepared by organic templating: Relationship between the molecular template and pore structure.* Chemistry Of Materials, 1999. **11**(5): p. 1223-1229.

43.   Chen, Z., et al., *DNA translocation through an array of kinked nanopores.* Nature Materials, 2010. **9**(8): p. 667-675.

44.   Moghaddam, S., et al., *An inorganic-organic proton exchange membrane for fuel cells with a controlled nanoscale pore structure.* Nature Nanotechnology, 2010. **5**(3): p. 230-236.

45.   Feng, H., et al., *Catalytic nanoliths.* Chemical Engineering Science, 2009. **64**(3): p. 560-567.

46.   Stair, P.C., et al., *Novel, uniform nanostructured catalytic membranes.* Topics in Catalysis, 2006. **39**(3-4): p. 181-186.

47.   Forster, P., et al., *Changes in Atmospheric Constituents and in Radiative Forcing Chapter 2.* 2007, United Kingdom: Cambridge University Press.

48.   Agency, I.E., *CO2 Emissions from Fuel Combustion Highlights (2015 Edition).* IEA Publications, 2015.

49.   Organization, W.M., *The State of Greenhouse Gases in the Atmosphere Based on Global Observations through 2013.* WMO Greenhouse Gas Bulletin, 2014. **10**.

50.   Aaron, D. and C. Tsouris, *Separation of CO2 from Flue Gas: A Review.* Separation Science and Technology, 2005. **40**(1-3): p. 321-348.

51.   Rao, A.B. and E.S. Rubin, *A Technical, Economic, and Environmental Assessment of Amine-Based CO2 Capture Technology for Power Plant Greenhouse Gas Control.* Environmental Science & Technology, 2002. **36**(20): p. 4467-4475.

52.   Khalilpour, R., et al., *Membrane-based carbon capture from flue gas: a review.* Journal of Cleaner Production, 2015. **103**: p. 286-300.

53.   Kentish, S.E., C.A. Scholes, and G.W. Stevens, *Carbon Dioxide Separation through Polymeric Membrane Systems for Flue Gas Applications.* Recent Patents on Chemical Engineering, 2008. **1**(1): p. 52-66.

54.   Chow, J.C., et al., *Separation and Capture of CO2 from Large Stationary Sources and Sequestration in Geological Formations.* Journal of the Air & Waste Management Association, 2003. **53**(10): p. 1172-1182.

55.   Yao, K., et al., *Biomimetic material—poly (N-vinylimidazole)–zinc complex for CO 2 separation.* Chemical Communications, 2012. **48**(12): p. 1766-1768.

56.   Bao, L. and M.C. Trachtenberg, *Facilitated transport of CO 2 across a liquid membrane: comparing enzyme, amine, and alkaline.* Journal of Membrane Science, 2006. **280**(1): p. 330-334.

57.   Ward, W.J. and W.L. Robb, *Carbon dioxide-oxygen separation: facilitated transport of carbon dioxide across a liquid film.* Science, 1967. **156**(3781): p. 1481-1484.

58.   Trachtenberg, M.C., et al., *Membrane-based, enzyme-facilitated, efficient carbon dioxide capture.* Energy Procedia, 2009. **1**(1): p. 353-360.

59.   Alivisatos, P. and M. Buchanan, *Basic Research Needs for Carbon Capture: Beyond 2020.* 2010: ; USDOE Office of Science (SC) (United States). Medium: ED; Size: 196 p.

60.   Toy, L., et al., *CO2 capture membrane process for power plant flue gas.* Research Triangle Park, NC: RTI International, 2012: p. 76.

61.   Brinker, C.J., et al., *Evaporation-induced self-assembly: nanostructures made easy.* Advanced materials, 1999. **11**(7): p. 579-585.

62.   Pang, J., et al., *Directed Aerosol Writing of Ordered Silica Nanostructures on Arbitrary Surfaces with Self-Assembling Inks.* Small, 2008. **4**(7): p. 982-989.

63.   Jiang, Y.-B., et al., *Sub-10 nm thick microporous membranes made by plasma-defined atomic layer deposition of a bridged silsesquioxane precursor.* Journal of the American Chemical Society, 2007. **129**(50): p. 15446-15447.

64. Wang, J., et al., *Superhydrophilic antireflective periodic mesoporous organosilica coating on flexible polyimide substrate with strong abrasion-resistance.* ACS applied materials & interfaces, 2017. **9**(6): p. 5468-5476.

65. Singh, S., et al., *Superhydrophobicity: drying transition of confined water.* Nature, 2006. **442**(7102): p. 526-526.

66. Hooks, D.O. and B.H. Rehm, *Surface display of highly-stable Desulfovibrio vulgaris carbonic anhydrase on polyester beads for CO2 capture.* Biotechnology letters, 2015. **37**(7): p. 1415-1420.

67. Trachtenberg, M.C. *Enzyme Facilitated Carbon Dioxide Capture.* in *Carbon Capture and Storage: Technology Innovation and Market Viability.* 2011. AGRION Business Network for Energy Cleantech, Sustainable Development.

68. Emami, F.S., et al., *Prediction of specific biomolecule adsorption on silica surfaces as a function of pH and particle size.* Chemistry of Materials, 2014. **26**(19): p. 5725-5734.

69. Patwardhan, S.V., et al., *Chemistry of aqueous silica nanoparticle surfaces and the mechanism of selective peptide adsorption.* Journal of the American Chemical Society, 2012. **134**(14): p. 6244-6256.

70. Lei, C., et al., *Entrapping enzyme in a functionalized nanoporous support.* Journal of the American Chemical Society, 2002. **124**(38): p. 11242-11243.

71. Pronk, S., et al., *GROMACS 4.5: a high-throughput and highly parallel open source molecular simulation toolkit.* Bioinformatics, 2013: p. btt055.

72. Echeverria, C. and R. Kapral, *Enzyme kinetics and transport in a system crowded by mobile macromolecules.* Physical Chemistry Chemical Physics, 2015. **17**(43): p. 29243-29250.

73. Schmit, J.D., E. Kamber, and J. Kondev, *Lattice model of diffusion-limited bimolecular chemical reactions in confined environments.* Physical review letters, 2009. **102**(21): p. 218302.

74. Best, R.B., et al., *Optimization of the additive CHARMM all-atom protein force field targeting improved sampling of the backbone ϕ, ψ and side-chain χ1 and χ2 dihedral angles.* Journal of chemical theory and computation, 2012. **8**(9): p. 3257-3273.

75. MacKerell Jr, A.D., et al., *All-atom empirical potential for molecular modeling and dynamics studies of proteins.* The journal of physical chemistry B, 1998. **102**(18): p. 3586-3616.

76. Saito, R., et al., *Structure of bovine carbonic anhydrase II at 1.95 Å resolution.* Acta Crystallographica Section D: Biological Crystallography, 2004. **60**(4): p. 792-795.

77. Heinz, H., et al., *Thermodynamically consistent force fields for the assembly of inorganic, organic, and biological nanostructures: the INTERFACE force field.* Langmuir, 2013. **29**(6): p. 1754-1765.

78. Emami, F.S., et al., *Force field and a surface model database for silica to simulate interfacial properties in atomic resolution.* Chemistry of Materials, 2014. **26**(8): p. 2647-2658.

79. Søndergaard, C.R., et al., *Improved treatment of ligands and coupling effects in empirical calculation and rationalization of p K a values.* Journal of Chemical Theory and Computation, 2011. **7**(7): p. 2284-2295.

80.   Tsige, M., et al., *Interactions and structure of poly (dimethylsiloxane) at silicon dioxide surfaces: Electronic structure and molecular dynamics studies.* The Journal of chemical physics, 2003. **118**(11): p. 5132-5142.

81.   Lorenz, C.D., et al., *Simulation study of the silicon oxide and water interface.* Journal of Computational and Theoretical Nanoscience, 2010. **7**(12): p. 2586-2601.

82.   Bard, A.J. and M.A. Fox, *Artificial photosynthesis: solar splitting of water to hydrogen and oxygen.* Accounts of Chemical Research, 1995. **28**(3): p. 141-145.

83.   Lewis, N.S. and D.G. Nocera, *Powering the planet: Chemical challenges in solar energy utilization.* Proceedings of the National Academy of Sciences, 2006. **103**(43): p. 15729-15735.

84.   Turner, J.A., *Sustainable hydrogen production.* Science, 2004. **305**(5686): p. 972-974.

85.   Walter, M.G., et al., *Solar water splitting cells.* Chemical reviews, 2010. **110**(11): p. 6446-6473.

86.   Colbeau, A. and P.M. Vignais, *The membrane-bound hydrogenase of Rhodopseudomonas capsulata: Stability and catalytic properties.* Biochimica et Biophysica Acta (BBA)-Enzymology, 1981. **662**(2): p. 271-284.

87.   Conway, B. and B. Tilak, *Interfacial processes involving electrocatalytic evolution and oxidation of H 2, and the role of chemisorbed H.* Electrochimica Acta, 2002. **47**(22): p. 3571-3594.

88.   Tafel, J., *Ueber strychnin. Justus Liebig's Annalen der Chemie.* Annalen der Chemie, 1898. **301**: p. 285-348.

89.   Tafel, J. and K. Naumann, *Die elektrolytische Reduction des Strychnis und Brucins.* European Journal of Inorganic Chemistry, 1901. **34**(3): p. 3291-3299.

90.   Jaramillo, T.F., et al., *Identification of active edge sites for electrochemical H2 evolution from MoS2 nanocatalysts.* science, 2007. **317**(5834): p. 100-102.

91.   Bonde, J., et al., *Hydrogen evolution on nano-particulate transition metal sulfides.* Faraday discussions, 2009. **140**: p. 219-231.

92.   Raybaud, P., et al., *Ab initio study of the H2–H2S/MoS2 gas–solid interface: The nature of the catalytically active sites.* Journal of Catalysis, 2000. **189**(1): p. 129-146.

93.   Hinnemann, B., et al., *Biomimetic hydrogen evolution: MoS2 nanoparticles as catalyst for hydrogen evolution.* Journal of the American Chemical Society, 2005. **127**(15): p. 5308-5309.

94.   Kong, D., et al., *Synthesis of MoS2 and MoSe2 films with vertically aligned layers.* Nano letters, 2013. **13**(3): p. 1341-1347.

95.   Karunadasa, H.I., et al., *A molecular MoS2 edge site mimic for catalytic hydrogen generation.* Science, 2012. **335**(6069): p. 698-702.

96.   Kibsgaard, J., et al., *Engineering the surface structure of MoS2 to preferentially expose active edge sites for electrocatalysis.* Nature materials, 2012. **11**(11): p. 963-969.

97.   Kibsgaard, J., T.F. Jaramillo, and F. Besenbacher, *Building an appropriate active-site motif into a hydrogen-evolution catalyst with thiomolybdate [Mo3S13] 2− clusters.* Nature chemistry, 2014. **6**(3): p. 248-253.

98.   Kim, J., et al., *Enhanced electrocatalytic properties of transition-metal dichalcogenides sheets by spontaneous gold nanoparticle decoration.* The journal of physical chemistry letters, 2013. **4**(8): p. 1227-1232.

99.   Lukowski, M.A., et al., *Enhanced hydrogen evolution catalysis from chemically exfoliated metallic MoS2 nanosheets.* Journal of the American Chemical Society, 2013. **135**(28): p. 10274-10277.

100.   Voiry, D., et al., *Conducting MoS2 nanosheets as catalysts for hydrogen evolution reaction.* Nano letters, 2013. **13**(12): p. 6222-6227.

101.   Azizi, A., et al., *Dislocation motion and grain boundary migration in two-dimensional tungsten disulphide.* Nature communications, 2014. **5**.

102.   Erickson, K., et al., *Determination of the local chemical structure of graphene oxide and reduced graphene oxide.* Advanced Materials, 2010. **22**(40): p. 4467-4472.

103.   Gómez-Navarro, C., et al., *Atomic structure of reduced graphene oxide.* Nano letters, 2010. **10**(4): p. 1144-1148.

104.   Somoano, R., V. Hadek, and A. Rembaum, *Alkali metal intercalates of molybdenum disulfide.* The Journal of Chemical Physics, 1973. **58**(2): p. 697-701.

105.   Py, M. and R. Haering, *Structural destabilization induced by lithium intercalation in MoS2 and related compounds.* Canadian Journal of Physics, 1983. **61**(1): p. 76-84.

106.   Chrissafis, K., et al., *Structural studies of MoS2 intercalated by lithium.* Materials Science and Engineering: B, 1989. **3**(1-2): p. 145-151.

107.   Sandoval, S.J., et al., *Raman study and lattice dynamics of single molecular layers of MoS 2.* Physical Review B, 1991. **44**(8): p. 3955.

108.   Qin, X., et al., *Real-space imaging of single-layer MoS 2 by scanning tunneling microscopy.* Physical Review B, 1991. **44**(7): p. 3490.

109.   Schumacher, A., et al., *Single-layer MoS2 on mica: studies by means of scanning force microscopy.* Surface science, 1993. **289**(1-2): p. L595-L598.

110.   Dungey, K.E., M.D. Curtis, and J.E. Penner-Hahn, *Structural characterization and thermal stability of MoS2 intercalation compounds.* Chemistry of Materials, 1998. **10**(8): p. 2152-2161.

111.   Heising, J. and M.G. Kanatzidis, *Structure of restacked MoS2 and WS2 elucidated by electron crystallography.* Journal of the American Chemical Society, 1999. **121**(4): p. 638-643.

112.   Petkov, V., et al., *Structure of nanocrystalline materials using atomic pair distribution function analysis: Study of LiMoS 2.* Physical Review B, 2002. **65**(9): p. 092105.

113.   Maitra, U., et al., *Highly Effective Visible-Light-Induced H2 Generation by Single-Layer 1T-MoS2 and a Nanocomposite of Few-Layer 2H-MoS2 with Heavily Nitrogenated Graphene.* Angewandte Chemie International Edition, 2013. **52**(49): p. 13057-13061.

114.   Eda, G., et al., *Photoluminescence from chemically exfoliated MoS2.* Nano letters, 2011. **11**(12): p. 5111-5116.

115.   Eda, G., et al., *Coherent atomic and electronic heterostructures of single-layer MoS2.* Acs Nano, 2012. **6**(8): p. 7311-7317.

116.   Kappera, R., et al., *Phase-engineered low-resistance contacts for ultrathin MoS2 transistors*. Nature materials, 2014. **13**(12): p. 1128-1134.

117.   Asadi, M., et al., *Robust carbon dioxide reduction on molybdenum disulphide edges*. Nature communications, 2014. **5**.

118.   Voiry, D., et al., *Enhanced catalytic activity in strained chemically exfoliated WS2 nanosheets for hydrogen evolution*. Nature materials, 2013. **12**(9): p. 850-855.

119.   Calandra, M., *Chemically exfoliated single-layer MoS 2: Stability, lattice dynamics, and catalytic adsorption from first principles*. Physical Review B, 2013. **88**(24): p. 245428.

120.   Tung, V.C., et al., *High-throughput solution processing of large-scale graphene*. Nature nanotechnology, 2009. **4**(1): p. 25-29.

121.   Tung, V.C., et al., *Low-temperature solution processing of graphene− carbon nanotube hybrid materials for high-performance transparent conductors*. Nano letters, 2009. **9**(5): p. 1949-1955.

122.   Tung, V.C., et al., *Towards solution processed all-carbon solar cells: a perspective*. Energy & Environmental Science, 2012. **5**(7): p. 7810-7818.

123.   Heising, J. and M.G. Kanatzidis, *Exfoliated and restacked MoS2 and WS2: Ionic or neutral species? Encapsulation and ordering of hard electropositive cations*. Journal of the American Chemical Society, 1999. **121**(50): p. 11720-11732.

124.   Du, P., et al., *Photocatalytic generation of hydrogen from water using a platinum (II) terpyridyl acetylide chromophore*. Journal of the American Chemical Society, 2006. **128**(24): p. 7726-7727.

125.   Min, S. and G. Lu, *Enhanced electron transfer from the excited eosin Y to mpg-C3N4 for highly efficient hydrogen evolution under 550 nm irradiation*. The Journal of Physical Chemistry C, 2012. **116**(37): p. 19644-19652.

126.   Min, S. and G. Lu, *Sites for high efficient photocatalytic hydrogen evolution on a limited-layered MoS2 cocatalyst confined on graphene sheets—the role of graphene*. The Journal of Physical Chemistry C, 2012. **116**(48): p. 25415-25424.

127.   Lazarides, T., et al., *Making hydrogen from water using a homogeneous system without noble metals*. Journal of the American Chemical Society, 2009. **131**(26): p. 9192-9194.

128.   Schneemeyer, L.F. and M.S. Wrighton, *Flat-band potential of n-type semiconducting molybdenum disulfide by cyclic voltammetry of two-electron reductants: interface energetics and the sustained photooxidation of chloride*. Journal of the American Chemical Society, 1979. **101**(22): p. 6496-6500.

129.   Min, S. and G. Lu, *Dye-sensitized reduced graphene oxide photocatalysts for highly efficient visible-light-driven water reduction*. The Journal of Physical Chemistry C, 2011. **115**(28): p. 13938-13945.

130.   Valeur, B. and M.N. Berberan-Santos, *Molecular fluorescence: principles and applications*. 2012: John Wiley & Sons.

131.   Tsai, C., F. Abild-Pedersen, and J.K. Nørskov, *Tuning the MoS2 edge-site activity for hydrogen evolution via support interactions*. Nano letters, 2014. **14**(3): p. 1381-1387.

132. Sanchez, V.C., et al., *Biological interactions of graphene-family nanomaterials: an interdisciplinary review.* Chemical research in toxicology, 2011. **25**(1): p. 15-34.

133. Chou, S.S., et al., *Chemically Exfoliated MoS2 as Near‐Infrared Photothermal Agents.* Angewandte Chemie, 2013. **125**(15): p. 4254-4258.

134. Perdew, J.P., K. Burke, and M. Ernzerhof, *Generalized gradient approximation made simple.* Physical review letters, 1996. **77**(18): p. 3865.

135. Kresse, G. and J. Furthmüller, *Efficient iterative schemes for ab initio total-energy calculations using a plane-wave basis set.* Physical review B, 1996. **54**(16): p. 11169.

136. Blöuml, P., *Projector augmented-wave method [J].* Phys Rev B, 1994. **50**(24): p. 17953-17979.

137. Heyd, J., G.E. Scuseria, and M. Ernzerhof, *Hybrid functionals based on a screened Coulomb potential.* The Journal of Chemical Physics, 2003. **118**(18): p. 8207-8215.

138. Nørskov, J.K., et al., *Trends in the exchange current for hydrogen evolution.* Journal of The Electrochemical Society, 2005. **152**(3): p. J23-J26.